

Theoretically Predicted Production Cross Section of Single Vector Boson



By

Junaid Tariq

SUBMITTED IN PARTIAL FULFILLMENT OF THE
REQUIREMENT FOR THE DEGREE OF
MASTER OF PHILOSOPHY
AT
DEPARTMENT OF PHYSICS
QUAID-I-AZAM UNIVERSITY, ISLAMABAD

Certificate

The undersigned hereby certify that they have read and recommend to the department of physics for acceptance of thesis entitled "**Theoretically predicted production cross section of Single Vector Boson**" by **Junaid Tariq** in partial fulfillment of the requirements for the degree of **Master of Philosophy**.

Supervisor:

Dr. Shamona Fawad Qazi
Associate Professor
Department of Physics
Quaid-i-Azam University
Islamabad.

Submitted Through:

Dr. Nawazish Ali Khan
Professor
Department of Physics
Quaid-i-Azam University
Islamabad.

Copyright Notice

Author: **Junaid Tariq**
Title: **"Theoretically Predicted Production Cross Section of Single
Vector Boson"**
Department: **Physics**
Degree: **M.Phil** Convocation: _____ year: _____

Permission is herewith granted to **Quaid-i-Azam University** to circulate and to have copied for non-commercial purposes, at its discretion, the above title upon the request of individuals or institutions.

Signature of Author

This thesis is dedicated to *my beloved son*

Acknowledgments

I cannot express enough thanks to Dr. Nawazish Ali Khan chairman department of physics, for giving me the opportunity to do research in National Center of Physics and providing invaluable guidance throughout this research.

I would like to express my sincere thanks to Dr. Shamona Fawad Qazi for her assistance through my whole duration of M.Phil. She helped me to put my ideas, well above the level of simplicity and into something concrete. I would like to acknowledge his assistance in reading and correcting this thesis.

I would like to express my special thanks of gratitude to Dr. Wajid Ali Khan who give me the golden opportunity to do this work and also for his patience, kindness and wisdom he has given to me during the whole work. Dr. Wajid Ali Khan is the person who open my mind for the experimental high energy physics. His kind suggestions and words guided me through my whole analysis.

Thanks to all the members in High Energy Physics group at the National Center for Physics (NCP), especially Dr. Usman Ashraf, Muhammad Gul for their positive criticism and continuous support and encouragement through the early stages of chaos and confusion. Thanks to Dr. Ashfaq Ahmad, Dr. Irfan Ashgar, Dr. Mohammad Ahmed, Sharjeel Kashif, Sheikh Mansoor who helped me in completing this work.

The greatest thanks goes to my beloved parents who encouraged me when ever I faced difficulties. Finally, I am grateful to my wife and son. They are always the source of my happiness and encourage me when I am depressed.

Junaid Tariq
November 2021.

Abstract

The cross sections of Z and W boson and their ratios are experimentally measured at the ATLAS and CMS detector at the Large Hadron Collider (LHC) in proton-proton collision at various center of mass energies. Theoretically predicted cross section of the W and Z boson production cross section in a proton-proton collision at $\sqrt{s} = 13\text{ TeV}$ and 14 TeV are presented in this thesis.

The vector boson production cross section measurement at hadron collision provides a deep understanding of quantum chromodynamics (QCD) and electroweak (EW) processes. The production of W and Z bosons are best examples of hard scattering processes at Large Hadron Collider. Theoretical predictions in perturbative chromodynamics are available at next-to-next-to-leading order (NNLO).

Theoretically predicted production cross section and cross section ratios of W and Z vector bosons are compared with the measured results at various center of mass energies. Kinematics of these vector bosons and corresponding leptons are also presented.

Contents

1	Introduction	1
1.1	The Standard Model of Particle Physics	1
1.1.1	The Fundamental Particles	1
1.1.1.1	Fermions	1
1.1.1.2	Bosons	2
1.1.1.3	Gluons	2
1.1.1.4	Electroweak Bosons	2
1.1.1.5	Higgs boson	2
1.2	Beyond Standard Model	3
1.2.1	Grand Unification	3
1.2.2	Supersymmetry (SUSY)	3
1.2.3	String Theory	4
1.3	Elementary Particles Dynamics	4
1.3.1	Quantum Electrodynamics	4
1.3.2	Quantum Chromodynamics	5
1.3.3	Weak Interaction	6
1.3.3.1	Decay of W and Z Boson:	7
1.4	Theoretical Overview of Particle Physics	7
1.4.1	Theory of Quantum Electrodynamics	7
1.4.1.1	Dynamics of Photon	8
1.4.1.2	Dynamics of Spin 1/2 Particles	10
1.4.1.3	Plane Wave Solution of Dirac Equation	10
1.4.1.4	Interacting Charged Fermions	11
1.4.2	Theory of Quantum Chromodynamics	12
1.4.2.1	Quark anti-quark Interaction	13
1.4.2.2	Quark Quark Interaction	14
1.4.2.3	Asymptotic Freedom	14
1.4.2.4	Running Coupling	15
1.4.3	Theory of Weak Interactions	15

CONTENTS

1.4.3.1	Charged Weak Interaction	16
1.4.3.2	Decay of Neutron	17
1.4.3.3	Neutral Weak Interaction	17
1.5	Gauge Symmetry	18
1.5.0.1	Higgs Mechanism and Higgs Boson	18
1.6	Hadron Collider Physics	20
2	The Large Hadron Collider	21
2.1	Detectors at Large Hadron Collider	21
2.1.0.1	A Toroidal LHC Apparatus (ATLAS)	22
2.1.0.2	Compact Muon Solenoid (CMS)	22
2.1.0.3	Large Hadron Collider beauty (LHCb)	23
2.1.0.4	A Large Ion Collider Experiment (ALICE)	23
2.1.0.5	Large Hadron Collider Forward (LHCf)	24
2.1.0.6	TOTEM	24
2.2	Parameters Of LHC	24
2.2.1	LHC Co-ordinate System	24
2.2.2	Pseudo rapidity	25
2.2.3	Luminosity	26
2.2.4	Pile-up (PU)	27
2.2.5	Beam Spot	27
2.3	CMS Detector	27
2.3.1	Structure of CMS	28
2.3.2	CMS Tracker	29
2.3.3	Electromagnetic Calorimeter (ECAL)	30
2.3.4	Hadron Calorimeter (HCAL)	30
2.3.5	Magnetic System of CMS	31
2.3.6	CMS Muon System	32
2.3.6.1	Drift Tube Chamber	32
2.3.6.2	Cathode Strip Chamber	32
2.3.6.3	Resistive Plate Chamber	33
2.3.7	CMS Trigger System	33
3	Theory of Single Vector Bosons	35
3.1	Significance of W and Z Boson Production Cross Section	35
3.2	Theory of Single Vector Boson Production	36
3.2.1	Cross Section Calculation	36
3.2.2	Parton Distribution Functions	37

CONTENTS

3.3	Measurement of Cross Section at The LHC	39
3.4	Event Selection for Vector Bosons	40
3.4.0.1	ATLAS	40
3.4.0.2	CMS	41
3.5	Inclusive Cross Section of W and Z Bosons	41
3.5.1	Differential Production Cross Section of W and Z Boson:	43
3.6	Measurement of p_T of Vector Bosons	45
3.7	Measured Cross Section of W and Z Bosons at Different C.O.M Energy	46
3.8	Uncertainties in the Predictions	51
3.8.1	Computation of Hessian PDF uncertainties	51
3.8.2	Computation of Monte Carlo PDF uncertainties	52
3.8.3	Theoretical Uncertainties	52
3.8.3.1	The value of α_s ant its uncertainty	52
3.8.3.2	Computation of PDF+ α_s uncertainties	54
3.8.3.3	NNPDF-Combined PDF and α_s uncertainties:	54
4	Results and Discussions	56
4.1	Work Summary	56
4.2	NNPDF3.1 Parton Distribution Function	56
4.2.1	NNPDF3.1 PDFs	57
4.3	Results	61
4.3.1	Measurements vs Predictions	61
4.3.1.1	8 TeV	61
4.3.1.2	13 TeV	61
4.3.1.3	14 TeV	62
4.4	Theoretical Predictions and Uncertainties in Cross Section of W and Z Bosons.	63
4.4.0.1	Variation In Cross Section With QCD Scale	70
4.5	Kinematics of W and Z Boson	75
4.5.1	Transverse Momentum and Pseudo Rapidity Distribution	75
4.6	Leptons p_T and η Distribution	78
4.6.1	Di-lepton Mass and Rapidity Distribution	80

List of Figures

1.1	Fermions and Bosons in the Standard Model, figure adopted from [1].	2
1.2	Known Elementary particles in Standard Model. Parameters are taken from [2].	3
1.3	Trend of QED running coupling constant with Q^2 (left), QCD running coupling constant with Q^2 (right), figure adopted from [10].	15
1.4	The change in the vale of α_s with the energy scale Q and the current world average value is illustrated, Figure taken from [11]	16
1.5	The potential V of a complex scalar field ϕ [13]	19
2.1	Schematic layout of the LHC experiment at CERN, figure taken from [16]	21
2.2	Inner view of ATLAS detector, figure taken from [20].	23
2.3	Schematic illustration of the CMS detector, figure taken from [21].	23
2.4	Inside view of the LHCb detector at LHC, figure taken from [14].	24
2.5	Sketch of the TOTEM and CMS experiments at the LHC figure taken from [4] .	24
2.6	ATLAS and CMS coordinate system, figure taken from [20]	25
2.7	Pseudo rapidity values in 1 st quadrant	25
2.8	\mathcal{L}_{int} delivered to CMS versus data taking period for pp collisions at different LHC energies. The distribution of $<\mu>$ versus luminosity recorded by CMS for the 2011 - 2012 and 2015 - 2018 data taking period figure adopted from [25].	27
2.9	Cut view of CMS detector, the distance of different components from center is illustrated in figure taken from [28]	29
2.10	Polar coordinates used by CMS. Figure taken from reference [29].	29
2.11	Schematic view of CMS detector. Figure taken from [30].	30
2.12	CMS ECAL layout, figure taken from [18].	31
2.13	Layout of CMS HCAL, figure taken from [18].	31
2.14	View of CMS superconducting solenoid. Figure adopted from [18].	32
2.15	CMS muon detector system. Figure adopted from [34].	33
2.16	CMS recorded luminosity at 13 TeV.	34
2.17	The L1 trigger system of CMS, figure taken from [18].	34
3.1	Correlation of LHC, Tevatron and SPS hadron Collider between the x values of the interaction of two partons [20]	36
3.2	Schematic of proton-proton collision at LHC.	37

LIST OF FIGURES

3.3	Parton Distribution Function evaluated at $Q^2 = m_Z^2$ top [20], MSTW 2008 NNLO PDFs at $Q^2 = 10\text{GeV}^2$ and $Q^2 = 10^4\text{GeV}^2$ bottom [47]	39
3.4	$Z \rightarrow \mu\mu$ in ATLAS detector (left) and $W \rightarrow e\nu$ in CMS detector (right) [20].	40
3.5	Transverse mass m_t distributions of $W \rightarrow e\nu$ and $W \rightarrow \mu\nu$ process (top) and dilepton mass m_{ll} distribution (bottom) [57]	42
3.6	Graphical sketch for the generalized partonic hard part of the Drell-Yan process [46]	42
3.7	Comparison of PDfs of \bar{u} and \bar{s} quark with LHC and without LHC data. [20]. Comparison plots can also be found in [59].	44
3.8	Z boson rapidity distribution (<i>left</i>) and W boson rapidity distribution (<i>right</i>) in 7 TeV pp collisions(<i>top</i>), for $Z \rightarrow l^+l^-$ the combined $d\sigma/d y_Z $ cross-section measurement compared to NNLO theoretical predictions (<i>bottom</i>) [20]	44
3.9	Hadronic recoil illustration in $W^\pm \rightarrow l^\pm\nu$ events (<i>top</i>). Differential cross sections (Normalized) for W boson as a function of $p_T(W)$ for electron. Ratios of theoretical predictions to the data (<i>bottom</i>) [35].	45
3.10	The predicted increase in cross section of vector bosons [60].	46
3.11	Ratio of Measured to predicted cross section(<i>top</i>), comparison of measured and predicted cross section ratio of W and Z boson (<i>bottom</i>). [57]	48
3.12	Measurements of vector boson cross section production multiplied with leptonic branching ratio (<i>top</i>). Measurements of W^+ and W^- production cross section times branching ratio (<i>middle</i>). Ratio of W^+ to Z and W^+ to W^- <i>bottom</i> . The yellow line showing the measured value with various experimental uncertainties at 7 TeV, 36 pb^{-1} [56]	49
3.13	The CMS measured total cross sections of W , W^+ , W^- and Z boson times branching fraction and theoretically predicted cross section. In each column upper value represent measured cross section with uncertainties and lower value represent theoretically predicted cross section, and their ratio also. [61]	50
3.14	Measured cross section (red line) and predicted cross section with different PDFs. The data points with error bars represent theoretically predicted value with various uncertainties [61]	50
3.15	Measured total cross section ratios of vector bosons and predicted cross section ratios of vector boson with different PDFs set [61].	51
3.16	The value of α_s used by different PDF groups	53
3.17	Summary of theoretical uncertainties in prediction of W and Z boson cross-sections at 7TeV [63]	53
3.18	W^\pm and Z^0 total cross sections, plotted as a function of $\alpha_S(M_Z^2)$, at NLO. [63] .	55
4.1	The NNPDF3.1-LO PDFs for the gluon (g), down (d), up(u), strange (s), charm (c) and bottom (b) quarks. (a), (b): for $Q^2 = 10\text{GeV}^2$, (c), (d): for $Q^2 = 100\text{GeV}^2$ and (e), (f): for $Q^2 = 1000\text{GeV}^2$	57
4.2	The NNPDF3.1-NLO PDFs as a function of x for the gluon (g), down (d), up(u), strange (s), charm (c) and bottom (b) quarks and also for the corresponding anti-quarks. (a), (b): for $Q^2 = 10\text{GeV}^2$, (c), (d): for $Q^2 = 100\text{GeV}^2$ and (e), (f): for $Q^2 = 1000\text{GeV}^2$, (g), (H): for anti-quarks at 10GeV^2 and 100GeV^2 respectively.	58

LIST OF FIGURES

4.3	The NNPDF3.1-NNLO PDFs as a function of x for the gluon (g), down (d), up(u), strange (s), charm (c) and bottom (b) quarks. (a), (b): for $Q^2 = 10\text{GeV}^2$, (c), (d): for $Q^2 = 100\text{GeV}^2$ and (e), (f): for $Q^2 = 1000\text{GeV}^2$, (g), (h): for 10000GeV^2 . The gluon PDFs are scaled down by a factor of 5 and 10.	59
4.4	The NNPDF3.1-NNLO PDFs as a function of x for the gluon (g), down (d), up(u), strange (s), charm (c) and bottom (b) anti-quarks. (a), (b): for $Q^2 = 10\text{GeV}^2$, (c), (d): for $Q^2 = 100\text{GeV}^2$ and (e), (f): for $Q^2 = 10000\text{GeV}^2$, (g), (h): PDF function of quarks as a function of q . The gluon PDFs are scaled down by a factor of 5.	60
4.5	Figure 4.5 shows measured cross section of (W^+, W^-, Z and W^\pm) with the variation of center of mass energy and at 14 TeV value of cross section is predicted at NNLO.	63
4.6	4.6a showing the predicted cross section of W boson at 13 TeV NNLO using various Parton Distribution Function. The measured values are taken from [57]	63
4.7	4.7a showing the predicted cross section of Z boson at 13 TeV NNLO using various Parton Distribution Function. The measured values are taken from [57]	64
4.8	4.8a showing the predicted cross section Ratio of W and Z boson at 13 TeV NNLO using various Parton Distribution Functions. The measured values are taken from [57]	64
4.9	4.9a showing the predicted cross section Ratio of W^+ and W^- boson at 13 TeV NNLO using various Parton Distribution Functions. The measured values are taken from [57]	65
4.10	4.10a and 4.10b are the NLO predictions of W and Z boson at 13TeV , 4.10c and 4.10d are for the W^+ and W^- bosons at 13 TeV	65
4.11	In Figure: 4.11a 4.11b are the NNLO predictions of W boson production cross section at 13 TeV and 14 TeV with 68% C.L. uncertainties. 4.11c 4.11d are the Z boson production cross section and 4.11e 4.11f are the predicted ratio of W and Z boson production cross section at 13TeV and 14TeV . The vertical error bars on prediction represent: inner (PDF), middle (α_s), outer (PDF+ α_s combined) error.	66
4.12	In Figure 4.12a 4.12b are the NNLO predictions of W^+ boson production cross section at 13 TeV and 14 TeV with 68% C.L. uncertainties. 4.12c 4.12d are the W^- boson production cross section and 4.12e 4.12f are the predicted ratio of W^+ and W^- boson production cross section at 13TeV and 14TeV . The vertical error bars on prediction represent: inner (PDF), middle (α_s), outer (PDF+ α_s combined) error.	67
4.13	In Figure, 4.13a 4.13b are the NNLO predictions of W boson production cross section at 13 TeV and 14 TeV with 90% C.L. uncertainties. 4.13c 4.13d are the Z boson production cross section and 4.13e 4.13f and 4.13g 4.13h showing the predicted cross section of W^+ and W^- boson at 13 TeV and 14TeV respectively. The vertical error bars on prediction represent: inner (PDF), middle (α_s), outer (PDF+ α_s combined) error.	68

LIST OF FIGURES

4.14 In Figure, 4.14a 4.14b are the NNLO predictions of W^+ boson production cross section at 13 TeV and 14 TeV with 90% C.L. uncertainties. 4.14c 4.14d are the Z boson production cross section and 4.14e 4.14f are the predicted ratio of W and Z boson production cross section at 13TeV and 14TeV . These uncertainties are measured with hessian error vector method in which vertical error bars represent inner (PDF), middle (α_s) and outer (PDF+ α_s combined) uncertainties.	69
4.15 The predicted increase in production cross section of W and Z vector boson with the choice of $\alpha_s(M_Z^2)$ at 13 TeV .	70
4.16 The predicted increase in production cross section of W^+, W^- vector boson with the choice of $\alpha_s(M_Z^2)$ at 13 TeV .	71
4.17 The predicted change in cross section of W and Z boson with the change in factorisation μ_R and re-normalisation μ_F . 4.17a 4.17b with 68% C.L. at 13 TeV	71
4.18 In figure 4.18a and 4.18b shows the predicted change in cross section of W^+ and W^- boson with the change in factorisation μ_R and re-normalisation μ_F scale and 4.18c and 4.18d are the cross section ratio of W to Z and W^+ to W^- boson. The vertical error bars on prediction represent: inner (PDF), middle (α_s), outer (PDF+ α_s combined) error.	72
4.19 The predicted change in cross section of W and Z boson with the change in factorisation μ_R and re-normalisation μ_F scale at 14 TeV . 4.19a 4.19c, with 68% C.L. and 4.19b 4.19d with 90% C.L.. The vertical error bars on prediction represent: inner (PDF), middle (α_s), outer (PDF+ α_s combined) error.	73
4.20 In figure 4.20a 4.20b showing the cross section of W^+ and W^- boson with different QCD scales at 68% C.L. uncertainties. 4.20c 4.20d represent the predicted change in cross section ratio of W and Z boson with QCD scales and 4.20e 4.20f for the W^+ and W^- boson similarly.	74
4.21 In figure 4.21a, 4.21c, 4.21e are the theoretically predicted transverse momentum distribution of W^+ , W^- and Z boson at 14 TeV with LO, NLO, and NNLO. 4.21b, 4.21d, 4.21f for the 13 TeV for NLO and NNLO.	75
4.22 In figure 4.22a, 4.22c, 4.22e are the generator level theoretically predicted pseudo rapidity distribution of W^+ , W^- and Z boson at 14 TeV with LO, NLO, and NNLO. 4.22b, 4.22d, 4.22f for the 13 TeV for NLO and NNLO.	76
4.23 In figure 4.23a, 4.23c, 4.23e are the generator level transverse momentum distribution of W^+ , W^- and Z boson at 14 TeV with different QCD scales. 4.23b, 4.23d, 4.23f are the pseudo rapidity distribution for NLO and NNLO.	77
4.24 In figure 4.24a, 4.24b are the generator level rapidity distribution of W^+ boson at 14 TeV and 13 TeV . 4.24c, 4.24d for the W^- boson and 4.24e 4.24f for Z boson rapidity distribution.	78
4.25 In figure 4.25a, 4.25c, 4.25e are the generator level transverse momentum distribution of electron at 14 TeV with LO, NLO, and NNLO. 4.25b, 4.25d, 4.25f for the 13 TeV for NLO and NNLO.	79
4.26 In figure 4.26a, 4.26c, 4.26e are the generator level pseudo rapidity distribution of electron at 14 TeV with LO, NLO, and NNLO. 4.26b, 4.26d, 4.26f for the 13 TeV for NLO and NNLO.	80

LIST OF FIGURES

- | | |
|---|----|
| 4.27 In figure 4.27a, 4.27b are the generator level rapidity distribution of electron for W^+ boson event at 14 TeV and 13 TeV , 4.27c, 4.27d for W^- and 4.27e, 4.27f for the Z boson event. | 81 |
| 4.28 In figure 4.28a, 4.28c, 4.28d are the generator level Di-lepton transverse momentum distribution at 14 TeV with different QCD scales. | 82 |

List of Tables

2.1	Parameters of LHC detectors	22
3.1	Kinematic cuts for CMS analysis [56] at 7 TeV for leptonic channel of Z and W boson respectively.	41
3.2	Kinematic cuts for ATLAS analysis [57] at 13 TeV for the leptonic channel of Z and W boson respectively.	41
3.3	Measured and NNLO predicted Ratios of W^+/W^- and W^\pm/Z . The measured values are at 7 TeV with an integrated luminosity of 36 pb^{-1} at CMS [56].	46
3.4	The measured total σ^{tot} cross section for leptonic channel of W^- , W^+ , W^\pm and Z -boson, and predicted total cross section. The measured values with certain uncertainties ($\pm stat. \pm syst. \pm lumi.$) are at 7 TeV with integrated luminosity 36 pb^{-1} at CMS and the predictions are at NNLO [56].	47
3.5	The measured total σ^{tot} cross sections with uncertainties ($\pm stat. \pm syst. \pm lumi.$) for lepton channels of W^- , W^+ , W^\pm and Z -boson, and predicted total cross section. The measured values are at 8 TeV with integrated luminosity 18.2 pb^{-1} at CMS and predictions are at NNLO [60].	47
3.6	Measured and predicted Ratios W^+/W^- and W^\pm/Z . The measured values are at 8 TeV with integrated luminosity 18.2 pb^{-1} at CMS and predictions are at NNLO [60].	47
3.7	The measured total σ^{tot} cross sections for the lepton channel of W^- , W^+ , W^\pm , and Z -boson, and predicted total cross section. The measured values are at 13 TeV with integrated luminosity 43 pb^{-1} at CMS [61].	47
3.8	Measured and predicted Ratios W^+/W^- and W^\pm/Z . The measured values are at 13 TeV with integrated luminosity 43 pb^{-1} [61].	48
4.1	The measured total σ^{tot} cross sections for leptonic decay channels (electron, muon) of W^- , W^+ , W^\pm and Z -bosons at CMS with 8 TeV , 18.2 pb^{-1} , and predicted total cross section at 8 TeV . The uncertainties in measurement due to statistical, systematic and luminosity error. The NNPDF3.1-NNLO PDF is used for the predictions.	61
4.2	Measured values with statistical and systematic errors and predicted Ratios W^+/W^- and W^\pm/Z at 8 TeV . For prediction NNPDF3.1-NNLO PDF is used.	61
4.3	The measured [57] [61] total σ^{tot} cross sections with statistical, systematic and luminosity error for the electron channel of W^- , W^+ , W^\pm and Z -boson, and predicted total cross section at 13 TeV . The NNPDF3.1-NNLO PDF is used for the predictions.	62

LIST OF TABLES

4.4	Measured ratio with statistical and systematic errors and predicted Ratios W^+/W^- and W^\pm/Z at 13 TeV. For prediction NNPDF3.1-NNLO PDF is used. The measured values are taken from reference [57]	62
4.5	Predicted total cross section of W^- , W^+ , W^\pm and Z boson at 14 TeV. The NNPDF3.1-NNLO PDF is used for the predictions.	62
4.6	Predicted Ratios W^+/W^- and W^\pm/Z at 14TeV. For prediction NNPDF3.1-NNLO PDF is used.	62

CHAPTER 1

Introduction

1.1 The Standard Model of Particle Physics

Particle physics deals with the fundamental matter particles and the interactions between them. It also explains their properties such as mass, spin and charge.

1.1.1 The Fundamental Particles

In particle physics an elementary particle or fundamental particle is the one that has no internal structure or is not made of other particles. The current fundamental particles are called fermions which are called matter particles and other type are called anti-matter particles and bosons, which are the force carrying particles and allow interactions between matter particles.

1.1.1.1 Fermions

In Standard Model (SM) there are two types of fermions, the quarks and the leptons. The fermions obey the Pauli Exclusion Principle which states that two fermions can not have same state at the same time i.e. two fermions can not have same quantum numbers. All fermions have half integral spin. In SM there are twelve fermions which are divided into six generations, each one has two particles. Fermions are divided into two groups, leptons and quarks. The leptons have elementary charge of -1 . Leptons have three flavors of charged particle, electron e , muon μ and tau τ , each lepton has corresponding neutral particle called neutrino. Electron is the only lepton which is stable in the universe from these six leptons. All the other leptons are massive and not stable hence decay into other stable particles.

Quarks have three generations and each one has two types. These six quarks are up (u), down (d), strange (s), charm (c), bottom (b) and top (t). The up (u) and down (d) quarks are only stable. The other quarks are very unstable and decay very quickly. Quarks interact with each other by the exchange of particles called gluon. Quarks are the particles which make hadrons (baryons and mesons). These twelve fermions have corresponding anti particles called anti-fermions. Electron's antiparticle is positron having same mass but opposite charge of $+1$, and muon's anti particle is anti muon with charge $+1$, similarly is the case for all other fermions. Anti-fermion has same mass as that of the corresponding fermion but opposite charge.

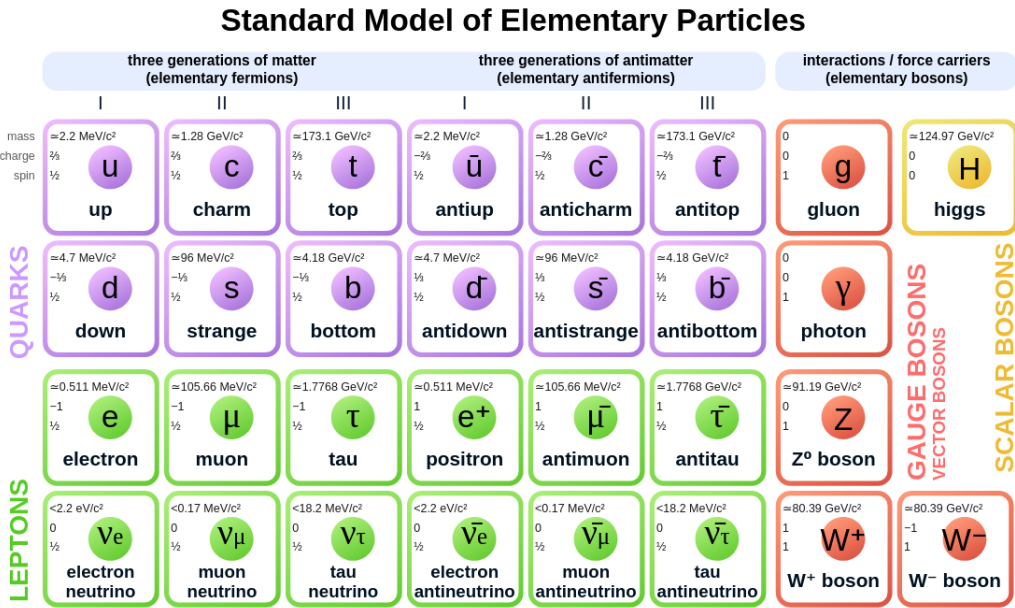


Figure 1.1: Fermions and Bosons in the Standard Model, figure adopted from [1].

1.1.1.2 Bosons

In standard model, vector bosons (photons, gluons, graviton, W and Z boson) have integer spin (spin=1,2) and scalar boson (Higgs) has no spin (spin=0). The vector bosons are mediator of interactions (force) between elementary particles and scalar boson gives mass to other elementary particles. Boson are different from fermions as they obey Bose-Einstein distribution whereas fermions obey Fermi-Dirac distribution. Boson can exist in both states either elementary, like photons, gluons or in a combined state, like mesons.

1.1.1.3 Gluons

Gluons mediate the strong interaction, which is responsible for the formation of hadrons. The hadrons are of two types, baryons and mesons. Baryon is composed of three quarks and meson has two quarks (quark-antiquark) state. Protons and neutrons are baryons, formed by the gluons and form atomic nucleus. Like quarks, gluons have a color and an anti color charge.

1.1.1.4 Electroweak Bosons

Weak bosons are of three types: W^+ , W^- , Z^0 . These bosons are the mediators of weak interaction. Unlike other bosons these are quite massive. The photon, which is a massless and charge less stable particle, which mediates the electromagnetic interaction. These four bosons are responsible for electroweak (combined electromagnetic and weak) interaction between fundamental particles.

1.1.1.5 Higgs boson

In the Standard Model, the only massive scalar boson with zero spin is the Higgs boson, an unstable particle with zero electric charge and no colour charge. Higgs boson decays into

Name	Discovered at	Mass	Charge	Colour	Spin	Lifetime
electron e	Cavendish Laboratory (1897)	0.511 MeV	-1	no	1/2	stable
muon μ	Caltech & Harvard (1937)	105.66 MeV	-1	no	1/2	2.2×10^{-6} sec
tau τ	SLAC (1976)	1776.82 MeV	-1	no	1/2	2.9×10^{-13} sec
electron neutrino ν_e	Savannah River Plant (1956)	< 2 eV	0	no	1/2	stable
muon neutrino ν_μ	Brookhaven (1962)	< 0.19 MeV	0	no	1/2	stable
tau neutrino ν_τ	Fermilab (2000)	< 18.2 MeV	0	no	1/2	stable
up quark u	SLAC (1968)	2.3 MeV	2/3	yes	1/2	stable
down quark d	SLAC (1968)	4.8 MeV	-1/3	yes	1/2	stable
charm quark c	Brookhaven & SLAC (1974)	1.275 GeV	2/3	yes	1/2	1.1×10^{-12} sec
strange quark s	Manchester University (1947)	95 MeV	-1/3	yes	1/2	1.24×10^{-8} sec
top quark t	Fermilab (1995)	173.21 GeV	2/3	yes	1/2	4.2×10^{-25} sec
bottom quark b	Fermilab (1977)	4.18 GeV	-1/3	yes	1/2	1.3×10^{-12} sec
photon γ	Washington University (1923)	0	0	no	1	stable
gluon g	DESY (1979)	0	0	yes	1	stable
W boson	CERN (1983)	80.385 GeV	± 1	no	1	3×10^{-25} sec
Z boson	CERN (1983)	91.1876 GeV	0	no	1	3×10^{-25} sec
Higgs boson H	CERN (2012)	125.7 GeV	0	no	0	1.56×10^{-22} sec

Figure 1.2: Known Elementary particles in Standard Model. Parameters are taken from [2].

other particles almost immediately after it's production. The Higgs boson are the quanta of field called Higgs field which gives mass to elementary particles via mechanism called Higgs mechanism.

1.2 Beyond Standard Model

The theoretical predictions that try to explain the shortcomings in SM are referred to as Physics Beyond Standard Model (BSM). The SM successfully explains particle physics phenomenology in \approx TeV scale. There are six major question in SM [3]:

- Higgs Sector (What is the nature of electro-weak symmetry breaking?)
- Naturalness (Is the mass of Higgs natural?)
- Neutrino mass (What is the mechanism by which neutrinos gain mass?)
- Baryon Asymmetry of the Universe (How the Universe has more baryons than anti baryons?)
- Strong CP Problem (Small neutron electric dipole moment?)
- Dark Matter (what is the nature of non-luminous but gravitationally interacting matter?)

1.2.1 Grand Unification

The Grand Unification theory (GUT) predicts that electromagnetic, strong and weak force can merge into a single force at very high energy scale. According to Grand Unified Theory we can merge all three fundamental forces into single one called electro nuclear force. Such unified force can be broken into three fundamental forces by a Higgs like mechanism. Grand unification models are expected at very high energy scale of about $\approx 10^{16}$ GeV.

1.2.2 Supersymmetry (SUSY)

Supersymmetry [4] predicts that each particle in SM either fermion or boson has a partner particle called superpartner. This can help us to explain why particles have mass. Symmetries

are very important in modern physics, since they give a nice way to construct Lagrangian for a field or particle from which equation of motion can be found. Well-known examples of symmetries are symmetry under Lorentz transformation, translational symmetry in space-time as well as symmetry under isospin transformations. Supersymmetry is different from these symmetries in that it is invariant under transformation of bosonic field/particle to fermionic field/particle and vice versa. Supersymmetry combines fermionic field and bosonic field in a single field called a super field.

There are two class of particles in SM, fermions or bosons based on their spin. All Fermions have $1/2$ units of spin, while the bosons have integer spin i.e. $0, 1, 2$. According to Supersymmetry theory each particle in SM has a partner particle whose spin differs from the particle in integer multiple of $1/2$. In this manner Supersymmetry brings two types of SM particles fermions and bosons together.

1.2.3 String Theory

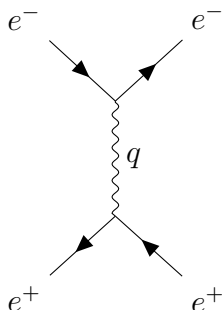
According to String Theory the sub-atomic particles are like a vibrating one dimensional strings rather zero dimensional point particles. The mode of vibration of the string corresponds to the mass, charge and other properties of particle. These strings exist in an eleven dimensional or twelve dimensional universe. These strings can vibrate with different frequencies. These frequencies are responsible for the strings mass, charge and spin. A string can have many shapes, open like a line or closed like a circle or more complicated shapes.

1.3 Elementary Particles Dynamics

There are four fundamental forces in nature through which matter particles interacts with each other. These forces are carried by particles called mediators of force. On the basis of mediating particles these interactions are divided into several types, each one explained below, briefly.

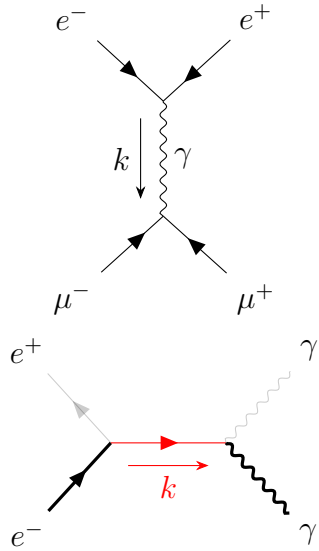
1.3.1 Quantum Electrodynamics

In Quantum Electrodynamics (QED) the electrically charged particles interact with each other by exchange of fields known as photon.



In above figure time flows horizontally, an electron and positron scattering mediated by a photon is shown. The anti-particle line is always directed backward in time while the particle is going forward. Pair production, Compton scattering and pair annihilation are the fundamental QED processes. In quantum electrodynamics the force mediators could be photons, electrons

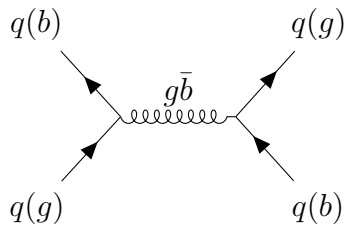
or positrons. According the Feynman rule, momentum is conserved at each vertex of Feynman diagram and for the whole process also.



1.3.2 Quantum Chromodynamics

Quantum chromodynamics is the theory of strong interaction between quarks and gluons, these are the fundamental particle that make up composite particles like hadrons.

Quarks have color charge and can be one of the three color charges red, blue, green. For any fundamental QCD process $q \rightarrow g + q$ the color charge of the quark can change but the flavour remains same. For example in a QCD interaction the color of up (u) quark may change but its flavour does not change. The color charge is always conserved in any QCD interaction. In the following Feynman diagram gluon must carry a unit of green and anti blue color charge to ensure color conservation.

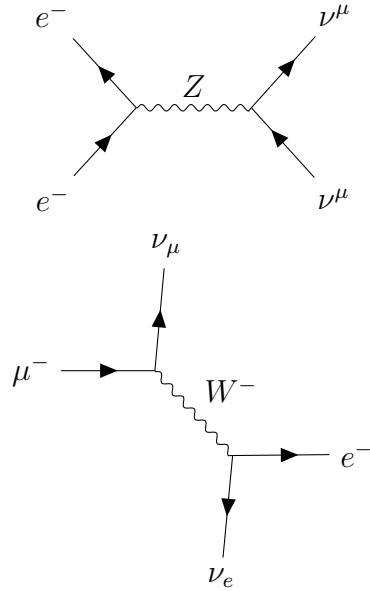


Gluons have color charge unlike photons which are electrically neutral, thus the gluons can interact with other gluons.

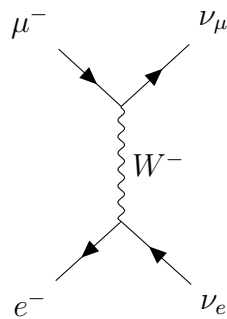
The coupling constant for QCD is different from the QED. In QED at each vertex we need a factor of $\alpha = 1/137$, because this number is very small thus we only need to consider Feynman diagrams with a small number of vertices. QCD coupling constant α_s depends upon the separation distance of the interacting particles (we call it a running coupling constant) at very small distance the value of strong coupling constant become very small, this phenomenon is known as asymptotic freedom. Thus quarks and anti-quarks inside the proton wander like free particles, such behavior was found experimentally in deep inelastic scattering experiments (DIS). Asymptotic freedom becomes more important in perturbation QCD theory.

1.3.3 Weak Interaction

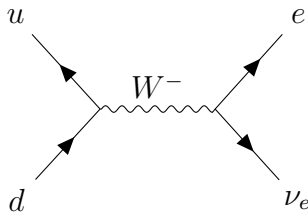
All quarks and all leptons interact through weak force (leptons have no color charge hence can not interact through strong interaction; neutrinos are charge less, so they cannot interact through electromagnetic forces; but all quarks and leptons can interact through weak interactions.) There are two types of weak interactions: charged weak interactions which are mediated by W boson and weak neutral interactions mediated by neutral Z boson.



The interactions in which the mediator is a Z boson is known as neutral weak interaction. The strong, electromagnetic and neutral weak interaction all share the feature that the same quark or lepton comes out when interaction occurs by an exchange of gluon, photon or Z boson. In QCD the color of the quark may change but flavour of particle does not. The charged weak interactions are the only interactions that change flavor of the particles and in this sense they are the only ones capable of causing a true decay.



Above Feynman diagram shows weak interaction of leptons in which a negative lepton (e^-, μ^-, τ^-) converts into the corresponding neutrino mediated by W^- boson, $l^- \rightarrow \nu_l + W^-$. Note in case of weak interaction of leptons, it can only convert into same generation i.e. e^- converts to ν_e , and $\mu^- \rightarrow \mu^-$ with the emission or absorption of W 's boson, but e^- never convert into μ^- nor μ^- to ν_e . Thus electroweak theory conserves the electron number, muon number, and tau number.



If a quark interacts with W^+ boson it will convert into an other quark of same generation i.e d -quark with charge $-1/3$ will convert into a u -quark of charge $2/3$, similarly for other quarks. In such interactions the flavor of quark changes but color remain same. W and Z bosons also known as Intermediate vector bosons or weak bosons are the mediator of Weak Interactions. They are also called vector bosons due to their spin ($s=1$). W bosons have charge ± 1 and Z boson is electrically neutral. W^+ and W^- are anti-particles of eachother and Z boson is its own anti-particle. The life time of these bosons is very small with a half-life of about $3 \times 10^{-25} \text{ sec}$.

The W boson is the only one which can cause nuclear transmutation by emission or absorption of leptons. The interaction with the exchange of Z boson is similar to the interactions in QED. Z boson can only transfer momentum or spin between interacting particles. In interaction with exchange of Z boson electrically charged particles can not be emit or absorbed.

The W and Z boson are massive elementary particles with masses 80.4 GeV [[ddd77f409a1d4f53a9ea8bbf](#)] and 91.2 GeV [[ddd77f409a1d4f53a9ea8bbf3f2e016d](#)] respectively, due to their high mass range of weak interaction is very small. Photon is the force carrier of Electromagnetic force and has no mass thus EM interactions have infinite range. The hypothetical Graviton also has no mass, Gluons also have no mass but range of strong interaction is not infinite due to the reason called color confinement.

1.3.3.1 Decay of W and Z Boson:

The W and Z bosons decay into lepton-anti lepton pairs and quark-antiquark pairs but these boson can not decay into top quark because its mass is higher than these bosons. In leptonic decay it decays into charged and neutral leptons and in hadronic decay into a quark and antiquark of different types with opposite electric charge. The W boson decays leptonically with a branching fraction $\frac{\Gamma_l}{\Gamma} = 32.12\%$ and hadronic $\frac{\Gamma_{hadron}}{\Gamma} = 67.60\%$ [5].

Similarly Z boson can decay leptonically as well as hadronically with $\frac{\Gamma_l}{\Gamma} = 30.7\%$ and $\frac{\Gamma_{hadron}}{\Gamma} = 69.2\%$ respectively. The hadronic to leptonic decay ratio for Z boson is $\frac{\Gamma_{hadron}}{\Gamma_{lepton}} = 20.767\%$ [6]

1.4 Theoretical Overview of Particle Physics

1.4.1 Theory of Quantum Electrodynamics

The problem with the non-relativistic Schrodinger equation is that, it has first order derivative of time component and second order derivative of space components. Klein-Gordon used the relativistic energy momentum relation and wrote the Schrödinger equation in a compact way [7].

$$(\partial_\mu \partial^\mu + m^2)\phi = 0, \quad (1.4.1)$$

In Eq. 1.4.1 $\partial_\mu = (\frac{\partial}{\partial(ct)}, \bar{\nabla})$ and $\partial^\mu = (\frac{\partial}{\partial(ct)}, -\bar{\nabla})$ with $\hbar = c = 1$. This Equation represents free particle case. Using Klein-Gordon equation for a wave function ϕ

$$\rho = \iota(\phi^* \frac{\partial \phi}{\partial t} - \phi \frac{\partial \phi^*}{\partial t}), \quad (1.4.2)$$

$$J = -\iota(\phi^* \nabla \phi - \phi \nabla \phi^*), \quad (1.4.3)$$

The Equation 1.4.2 represents probability density and Equation 1.4.3 represents probability current. Consider the plane wave solution for the K-G equation i.e $\phi = N \exp(\iota \bar{p} \cdot \bar{x} \pm \iota E t)$, we get;

$$E = \pm \sqrt{p^2 + m^2}, \quad (1.4.4)$$

$$\rho = 2E|N|^2, \quad (1.4.5)$$

The problem with K-G equation is that it has negative energy solutions ($E < 0$) and similarly with the probability density.

1.4.1.1 Dynamics of Photon

In electrodynamics, charge density ρ and current density J of electromagnetic field are determined by Maxwell's equations in vacuum, where \bar{E} is the electric field and \bar{B} is the magnetic field,

$$\bar{\nabla} \cdot \bar{E} = \frac{\rho}{\epsilon_0}, \quad (1.4.6)$$

$$\bar{\nabla} \times \bar{E} = -\frac{\partial \bar{B}}{\partial t}, \quad (1.4.7)$$

$$\bar{\nabla} \cdot \bar{B} = 0, \quad (1.4.8)$$

$$\bar{\nabla} \times \bar{B} = \bar{J} + \frac{\partial \bar{E}}{\partial t}, \quad (1.4.9)$$

The electric and magnetic fields in terms of an electromagnetic potential are given as,

$$\bar{E} = -\bar{\nabla} \phi - \frac{\partial \bar{A}}{\partial t}, \quad (1.4.10)$$

$$\bar{B} = \bar{\nabla} \times \bar{A}, \quad (1.4.11)$$

In relativistic notation, the field tensor for \bar{E} and \bar{B} , $F^{\mu\nu}$ [8] is,

$$F^{\mu\nu} = \begin{pmatrix} 0 & -E_x & -E_y & -E_z \\ E_x & 0 & -B_z & B_y \\ E_y & B_z & 0 & -B_x \\ E_z & -B_y & B_x & 0 \end{pmatrix}$$

The inhomogeneous Maxwell equations can be written in terms of field tensor:

$$\partial_\mu F^{\mu\nu} = J^\nu, \quad (1.4.12)$$

and similarly for homogeneous Maxwell equations:

$$\partial_\mu \tilde{F}^{\mu\nu} = 0, \quad (1.4.13)$$

The $\tilde{F}^{\mu\nu}$ is called dual or antisymmetric field tensor. The Equations 1.4.10 and 1.4.11 can be written in relativistic notation:

$$F^{\mu\nu} = \partial^\mu A^\nu - \partial^\nu A^\mu, \quad (1.4.14)$$

here $A^\mu = (\phi, \vec{A})$ is the four vector potential. In terms of four vector potential the inhomogeneous Maxwell Equations can be written :

$$J^\nu = \partial_\mu \cdot \partial^\mu A^\nu - \partial^\nu \cdot \partial_\mu A^\mu, \quad (1.4.15)$$

In the potential formulation we can not uniquely determine V (scalar potential) and A (vector potential). So we transform A^μ :

$$\hat{A}^\mu = A^\mu + \partial^\mu \chi, \quad (1.4.16)$$

This transformation $\hat{A}^\mu = A^\mu + \partial^\mu \chi$ is called gauge transformation and \vec{E} and \vec{B} fields remain invariant under gauge transformation. Here χ is some scalar function of position and time. The freedom to choose any $\hat{A}^\mu = A^\mu + \partial^\mu \chi$ is called gauge freedom. The gauge condition can be applied to potential in the following way:

$$\partial_\mu A^\mu = 0, \quad (1.4.17)$$

called Lorentz condition, Maxwell equations with this Lorentz condition applied become:

$$\partial_\mu \partial^\mu A^\nu = J^\nu, \quad (1.4.18)$$

Maxwell equation with Lorentz gauge condition is applied. For the empty space $J^\nu = 0$ and Maxwell equation reduces to,

$$\partial_\mu \partial^\mu A^\nu = 0, \quad (1.4.19)$$

this equation is recognised as Klein-Gordon equation for massless particles. In QED A^ν is the wave function of free photon, and plane wave solution for the massless photons are given by,

$$A^\nu = a\epsilon^\nu(p)e^{-i\vec{p}\cdot\vec{x}}, \quad (1.4.20)$$

Here ϵ^ν is polarization vector, by substituting this solution into Equation 1.4.19 we get

$$P^\mu P_\mu = 0, \quad E = pc, \quad (1.4.21)$$

which should be true for massless particles. Lorentz condition $\partial_\mu A^\mu = 0$ requires that

$$P^\mu \epsilon_\mu = 0 \quad (1.4.22)$$

In the Coulomb's gauge

$$\epsilon^0 = 0 \quad (1.4.23)$$

These equations show that the polarization vector of photon (ϵ) is perpendicular to the direction of propagation; if the direction of propagation is $z-axis$, then photon will be polarized in $xy-axis.$, thus we have only two linearly independent vectors perpendicular to \vec{p} ; for example, if \vec{p} is in the z direction, we might choose;

$$\epsilon^1 = (1, 0, 0) \quad (1.4.24)$$

$$\epsilon^2 = (0, 1, 0) \quad (1.4.25)$$

A particle with mass have $2s+1$ spin directions and massless particle has only two, independent of its spin, along its direction of motion it can only have $m_s = +s$ or $m_s = -s$.

1.4.1.2 Dynamics of Spin 1/2 Particles

The problem with Schrodinger equation is that it cannot explain the dynamics of relativistic particles because it is quadratic in space or position coordinate but first order derivative of time parameter, and problem with the Klein-Gordon equation is that, it cannot explain the dynamics of spin 1/2 particles. To address these problems Dirac introduced Dirac equation [9]. It was known that;

$$H^2\psi = (\bar{p}^2 + m^2)\psi, \quad (1.4.26)$$

Dirac introduced;

$$H\psi = (\bar{\alpha}\cdot\bar{p} + \beta m)\psi, \quad (1.4.27)$$

Here α and β are matrices with the following properties;

1. Eigen values = ± 1 .
2. Trace = 0.
3. α_i, β are hermitian matrices.
4. All matrices are linearly independent.

Thus 4×4 is the minimum number of dimensions required for the Dirac matrices. Dirac matrices may be written as;

$$\bar{\alpha}_i = \begin{pmatrix} 0 & \bar{\sigma}_i \\ \bar{\sigma}_i & 0 \end{pmatrix},$$

$$\beta = \begin{pmatrix} \mathbf{1} & 0 \\ 0 & \mathbf{1} \end{pmatrix}.$$

here $\bar{\sigma}_i$ are the 2×2 Pauli matrices, we can write Dirac matrices in standard notation;

$$\gamma^\mu = (\beta, \beta\bar{\alpha}); \quad (1.4.28)$$

here $\gamma^0 = \beta, \gamma^1 = \beta\alpha_1, \gamma^2 = \beta\alpha_2$ and $\gamma^3 = \beta\alpha_3$. Dirac equation in compact notation may be written as

$$(\iota\gamma^\mu\partial_\mu - m)\psi = 0. \quad (1.4.29)$$

1.4.1.3 Plane Wave Solution of Dirac Equation

For a particle at rest $p = 0$; ¹

$$\psi_A(t) = e^{-\iota(\frac{mc^2}{\hbar})t}\psi_A(0), \quad (1.4.30)$$

$$\psi_B(t) = e^{\iota(\frac{mc^2}{\hbar})t}\psi_B(0), \quad (1.4.31)$$

Where ψ_A represents a particle with positive energy and ψ_B represents a particle with negative energy. Here $\psi_A = \begin{pmatrix} \psi_1 \\ \psi_2 \end{pmatrix}$ and $\psi_B = \begin{pmatrix} \psi_3 \\ \psi_4 \end{pmatrix}$
when $p \neq 0$;

$$\psi = ae^{-\iota\frac{p\cdot x}{\hbar}}u, \quad (1.4.32)$$

$$\psi = ae^{\iota\frac{p\cdot x}{\hbar}}v, \quad (1.4.33)$$

here u and v are Dirac four dimensional spin matrices.

¹for detail see:David Griffith's Introduction to elementary particles(second revised edition),Section 7.2

1.4.1.4 Interacting Charged Fermions

Dirac equation for free a particle:²

$$(\gamma^\mu p_\mu - m)\psi = 0, \quad (1.4.34)$$

$$(\gamma^0 p_0 - \bar{\gamma} \cdot \bar{p} - m)\psi = 0, \quad (1.4.35)$$

$$E\psi = (\gamma^0 \bar{\gamma} \cdot \bar{p} + m\gamma^0)\psi, \quad (1.4.36)$$

For Interaction:

$$p^\mu \rightarrow p^\mu - QA^\mu, \quad (1.4.37)$$

for the case of electron

$$p^\mu \rightarrow p^\mu + eA^\mu, \quad (1.4.38)$$

so the Dirac equation for an electron interacting with E-M field (A^μ)

$$\gamma^\mu(p_\mu + eA_\mu)\psi - m\psi = 0, \quad (1.4.39)$$

$$E\psi = (\gamma^0 \bar{\gamma} \cdot \bar{p} + m\gamma^0)\psi - e\gamma^0 \gamma^\mu A_\mu \psi, \quad (1.4.40)$$

here

$$V = e\gamma^0 \gamma^\mu A_\mu \psi. \quad (1.4.41)$$

The potential for an electron interacting with EM field. The transition amplitude for the electron from state ψ_i to ψ_f is

$$T_{fi} = -\iota \int \psi_f^\dagger V \psi_i d^4x, \quad (1.4.42)$$

By putting the value in Eq. 1.4.42 from Eq. 1.4.41 we get:

$$T_{fi} = -\iota \int J^\mu A_\mu d^4x, \quad (1.4.43)$$

here J^μ is four vector current:

$$J^\mu = -e\psi^* \gamma^\mu \psi, \quad (1.4.44)$$

and A_μ is the E-M potential through which electron interacts. The source field A_μ must satisfy the equation

$$\partial_\mu \partial^\mu A^\mu = j^\mu, \quad (1.4.45)$$

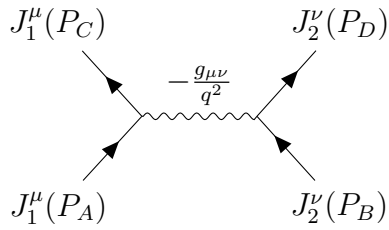
and its solution is

$$A^\mu = -\frac{1}{q^2} j^\mu, \quad (1.4.46)$$

Now Equation 1.4.43 become

$$T_{fi} = -\iota \int J_1^\mu \left(-\frac{g_{\mu\nu}}{q^2}\right) J_2^\nu d^4x, \quad (1.4.47)$$

²For detail see: chapter six of Quarks and Leptons:An introductory Course by Francis Halzen and Alan D.Martin



The above Feynman diagram represents electron-electron interaction, in which photon is a mediator of force.

$$J_1^\mu = -e\psi_B^*\gamma^\mu\psi_A, \quad (1.4.48)$$

$$J_2^\nu = -e\psi_D^*\gamma^\nu\psi_C, \quad (1.4.49)$$

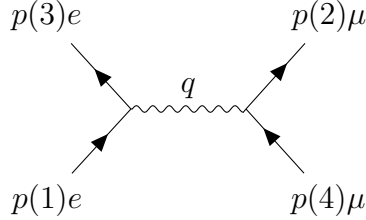
By substituting Equations 1.4.48 and 1.4.49 in 1.4.47 we get:

$$T_{fi} = -i(2\pi)^4\delta^4(P_A + P_c - P_B - P_D)\cdot\mathcal{M}, \quad (1.4.50)$$

$$\mathcal{M} = (-e\bar{U}_B\gamma^\mu U_A)(-\frac{g_{\mu\nu}}{(p_A - p_B)^2})(-e\bar{U}_D\gamma^\nu U_C), \quad (1.4.51)$$

\mathcal{M} is called "Lorentz Invariant Transition Amplitude"

Example(we may write electron-muon scattering amplitude as:)



By following Feynman rules we can write out Scattering amplitude (\mathcal{M} for the above diagram):

$$\mathcal{M} = -\frac{g_e^2}{(p_1 - p_3)^2}[\bar{u}_3(p_3)\gamma^\mu u_1(p_1)][\bar{u}_4(p_4)\gamma_\mu u_2(p_2)] \quad (1.4.52)$$

1.4.2 Theory of Quantum Chromodynamics

Quantum electrodynamics (QED) explains the interaction between charged particles; Quantum chromodynamics (QCD) describes the interaction between coloured particles; The mediator of electromagnetic interactions are photon and strong interactions are mediated by gluons which also massless particle. The coupling constant for the electromagnetic interaction is given by

$$g_e = \sqrt{4\pi\alpha} \quad (1.4.53)$$

and coupling constant for the strong force is set by strong coupling constant

$$g_s = \sqrt{4\pi\alpha_s} \quad (1.4.54)$$

Quarks can be labeled with different colour quantum number, red (r), blue (b) and green (g), therefore to describe the colour of quarks we must have an additional term in the Dirac spinor

which gives the colour factor of these quarks. For red:

$$c = \begin{pmatrix} 1 \\ 0 \\ 0 \end{pmatrix} \quad (1.4.55)$$

for blue:

$$c = \begin{pmatrix} 0 \\ 1 \\ 0 \end{pmatrix} \quad (1.4.56)$$

and for green:

$$c = \begin{pmatrix} 0 \\ 0 \\ 1 \end{pmatrix} \quad (1.4.57)$$

Each gluon carries one unit of colour and one unit of anti-colour then, there should be nine species of gluons. In term of SU(3) symmetry these nine states constitutes a 'colour octet' and a 'colour singlet'.³ Gluons are also massless spin 1 particles; similarly as for the photon, ϵ^μ is the polarisation vector of gluon which is perpendicular to the momentum of gluon:

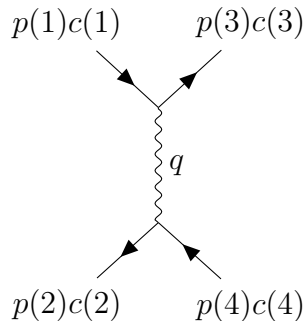
$$\epsilon^\mu p_\mu = 0 \quad (1.4.58)$$

And Coulomb gauge condition gives

$$\epsilon^0 = 0 \quad (1.4.59)$$

1.4.2.1 Quark anti-quark Interaction

In quark and an antiquark interaction, both have different flavors, the interaction amplitude is given by:



$$\mathcal{M} = \iota [\bar{u}(3)c_3^\dagger](-\iota \frac{g_s}{2} \lambda^\alpha \gamma^\mu)[u(1)c_1](\frac{\iota g_{\mu\nu}\delta_{\alpha\beta}}{q^2}) \times [\bar{\nu}(2)c_2^\dagger](-\iota \frac{g_s}{2} \lambda^\beta \gamma^\nu)[\nu(4)c_4] \quad (1.4.60)$$

Thus

$$\mathcal{M} = -\frac{g_s^2}{4q^2} [\bar{u}(3)\gamma^\mu u(1)][\bar{\nu}(2)\gamma_\nu \nu(4)][c_3^\dagger \lambda^\alpha c_1][c_2^\dagger \lambda^\alpha c_4] \quad (1.4.61)$$

Here g_e is replaced by g_s , and the extra term, which is called color factor.

³For detail see chapter 8 of 'Introduction to Elementary Particles' by David Griffith's

$$f = \frac{1}{4}(c_3^\dagger \lambda^\alpha c_1)(c_2^\dagger \lambda^\alpha c_4)$$

The color factor for the octet configuration is -1/6 and for the singlet configuration is -4/3. Thus the quark-antiquark potential are

$$\begin{aligned} V_{q\bar{q}} &= -\frac{4\alpha_s \hbar c}{3r} \\ V_{q\bar{q}} &= \frac{\alpha_s \hbar c}{6r} \end{aligned}$$

for color singlet and color octet configuration respectively.

1.4.2.2 Quark Quark Interaction

For the interaction between quark-quark the invariant amplitude can be written as:

$$\mathcal{M} = -\frac{g_s^2}{4q^2} [\bar{u}(3)\gamma^\mu u(1)][\bar{u}(4)\gamma_\mu u(2)][c_3^\dagger \lambda^\alpha c_1][c_4^\dagger \lambda^\alpha c_2], \quad (1.4.62)$$

The colour factor for this interaction is given by:

$$f = \frac{1}{4}(c_3^\dagger \lambda^\alpha c_1)(c_4^\dagger \lambda^\alpha c_2)$$

The color factor for the triplet configuration is -2/6 and for the sextet configuration is 1/3. Thus the quark-antiquark potential

$$\begin{aligned} V_{q\bar{q}} &= -\frac{2\alpha_s \hbar c}{3r}, \\ V_{q\bar{q}} &= \frac{\alpha_s \hbar c}{3r}, \end{aligned}$$

for color triplet and color sextet configuration respectively.

1.4.2.3 Asymptotic Freedom

In QED, the electron charge is directly related to momentum transfer of the interaction q .⁴ In QCD the running coupling constant is

$$\alpha_s(q^2) = \frac{\alpha_s(\mu^2)}{1 + [\frac{\alpha_s(\mu^2)}{12\pi}](11n - 2f) \ln(\frac{q^2}{\mu^2})}, \quad (1.4.63)$$

here n is the number of color(3) and f is the number of flavour(6). α_s is inversely proportional to q^2 and at short distance or high q^2 the α_s becomes very small and the strong force becomes relatively weak, this is also called asymptotic freedom. The coupling strength increase as we increase the distance between two quarks (antiquarks) and strong force becomes very large. If we try to separate two quarks then new quark-antiquark pairs are formed and process of hadronisation occurs. That's why the quarks are always confined inside hadrons and phenomenon is called quark confinement, that is why no single quark or gluon could be observed. In QCD long distance or low q^2 i.e. $q^2 = 0$ is not allowed, because at this scale α_s becomes very large, and perturbative QCD calculation can not be applied. For QCD perturbation expansions, we must set a reference scale where α_s is small enough that perturbative expansion can be done. Equation 1.4.63 is expressed in term of $\alpha_s(\mu^2)$ so that $\alpha_s(\mu^2) \ll 1$, the running coupling constant can be expressed in terms of a single parameter:

$$\alpha_s(q^2) = \frac{12\pi}{(11n - 2f) \ln(\frac{q^2}{\Lambda^2})} (q^2 \gg \Lambda^2), \quad (1.4.64)$$

⁴Equation 8.91 'introduction to Elementary Particles' by David Griffith's

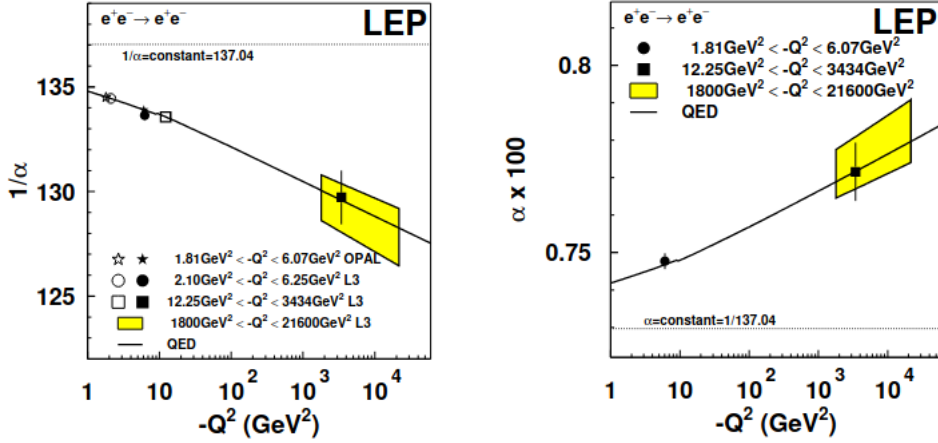


Figure 1.3: Trend of QED running coupling constant with Q^2 (left), QCD running coupling constant with Q^2 (right), figure adopted from [10].

1.4.2.4 Running Coupling

The coupling strength for QED, QCD and Electro weak (EW) processes are energy scale dependent. The pair production of electrically charged virtual particles leads to vacuum polarisation around charged fermions and consequently a distance-dependent shielding of their fundamental electric charge. This causes running coupling constant g_e to increase with the energy scale of the interaction q^2 , and decreasing length-scale. The running of QCD and EW coupling constants follow the opposite trend, at least up to the symmetry breaking scale. The equivalent effect for colour charge, quark pair production and gluon self-coupling contributions (cubic and quartic), effect the range of QCD interactions. If as in nature, $2N_f - 11N_c \neq 0$ ($N_f = 6, N_c = 3$) then quarks will experience asymptotic freedom such that g_s increases with length-scale and with decreasing Q^2 . As a result of the running of the strong coupling strength, at low energies q^2 the perturbative approximation are invalid. The bare quarks will produce qq pairs from the vacuum to exist as colour charge-neutral states in a process known as confinement. These colourless states are known as hadrons which include $q\bar{q}$ (mesons) and $qqq/\bar{q}q\bar{q}$ (baryons)

1.4.3 Theory of Weak Interactions

Weak interaction are mediated by (as photons for QED and gluons for QCD) the W and Z^0 bosons and these mediators are extremely heavy. Experimentally $M_w = 80.387 \pm 0.016$ GeV [PhysRevD.98.030001] and $M_z = 91.188 \pm 0.0031$ GeV [PhysRevD.98.030001].

We know that the massless photons and gluons have two polarization states after imposing Lorentz condition and Coulomb gauge condition but particles with mass and spin one, are allowed to have three polarization states $m_s = (-1, 0, 1)$, Thus for the W and Z boson the completeness relation is quite different and propagator factor no longer remain same but becomes, $\frac{\epsilon g_{\mu\nu}}{Mc^2}$ here we assume $q^2 \ll (Mc^2)$.

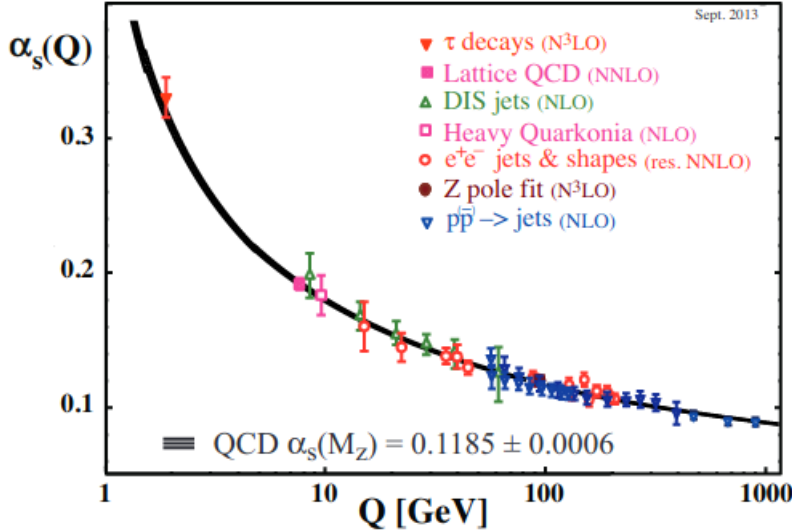
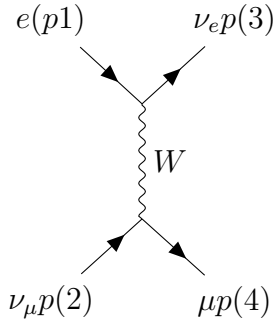


Figure 1.4: The change in the vale of α_S with the energy scale Q and the current world average value is illustrated, Figure taken from [11]

1.4.3.1 Charged Weak Interaction

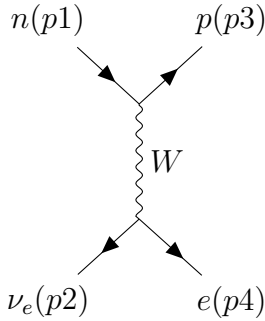


Considered the process, $\nu_\mu + e^- \rightarrow \mu^- + \nu_e$ The amplitude for this interaction is

$$\mathcal{M} = \frac{g_W^2}{8(M_w c^2)} [\bar{u}(3)\gamma^\mu(1 - \gamma^5)u(1)][\bar{u}(4)\gamma_\mu(1 - \gamma^5)u(2)], \quad (1.4.65)$$

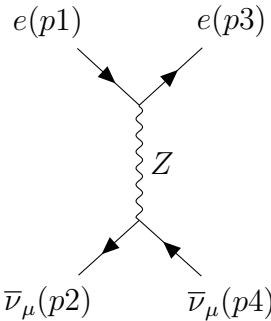
Here γ^μ alone represents vector coupling whereas $\gamma^\mu\gamma^5$ would be an axial vector. When we mix a vector to an axial vector then we are bound to violate the parity conservation, that is what happens in weak interactions. Here $g_w = \sqrt{4\pi\alpha_w}$ and its value is 0.653, and hence the weak fine structure constant is $\alpha_w = \frac{1}{29.5}$. This coupling constant is roughly 5 times larger than that of QED but weak interaction are feeble because of massive mediators W and Z bosons.

1.4.3.2 Decay of Neutron



The above Feynman diagram shows the beta decay of neutron, by applying Feynman calculus we find that the neutron life time $\tau = \frac{1}{\Gamma} = 1318$ s, as the experimental neutron lifetime is 885.7 ± 0.8 [serebrov2019neutron] seconds. The problem arises due to fact that we treat the proton and neutron as a point particles like leptons, which interact with the W boson. We don't know, what kind of structure protons and neutrons have and what kind of interactions are going on inside proton i.e. (valence quarks interaction with gluon, quark pairs formed by gluons, hadronisation) but all the finalized activity conserves charge. This problem arises because we don't know how quarks couple with the vector bosons.

1.4.3.3 Neutral Weak Interaction



The above Feynman diagram shows $\bar{\nu}_\mu + e \rightarrow \bar{\nu}_\mu + e$ process mediated by Z boson. The vertex factor for the Z^0 boson is not so simple;

$$\frac{-ig_z}{2}\gamma^\mu(c_v^f - c_A^f\gamma^5) \quad (1.4.66)$$

Where g_z is the neutral coupling constant, and the coefficient, c_v^f and c_A^f depend on the particular quark or lepton involved. All these parameters are determined by single parameter called θ_W the 'weak mixing angle'. The weak and electromagnetic coupling constant are related:

$$g_e = \frac{g_e}{\sin\theta_w}, g_z = \frac{g_e}{\sin\theta_w \cos\theta_w} \quad (1.4.67)$$

The experimental value of θ_w is 28.75. The amplitude for the above scattering at low energies ($q^2 \ll M_z^2 c^2$) is:

$$\mathcal{M} = \frac{g_z^2}{8(M_Z c)^2} [\bar{u}(3)\gamma^\mu(1 - \gamma^5)u(1)][\bar{u}(4)\gamma_\mu(c_v - c_A\gamma^5)u(2)] \quad (1.4.68)$$

1.5 Gauge Symmetry

The lagrangian densities for the fermionic and electromagnetic fields can be written [12] K-G equation:

$$\mathcal{L} = \frac{1}{2}(\partial_\mu\phi)(\partial^\mu\phi) - \frac{1}{2}m^2\phi^2, \quad (1.5.1)$$

Dirac equation:

$$\mathcal{L} = i\bar{\psi}\gamma^\mu\partial_\mu\psi - m\bar{\psi}\psi, \quad (1.5.2)$$

Maxwell equation:

$$\mathcal{L} = \frac{-1}{4}F^{\mu\nu}F_{\mu\nu} - j^\mu A_\mu, \quad (1.5.3)$$

Now if we transform the field ψ of the Dirac Lagrangian as $\psi \rightarrow \psi' = e^{i\alpha}\psi$ where α is some constant. Such transformation of field is called Global gauge transformation and Lagrangian \mathcal{L} remains invariant under such transformation. To make the Lagrangian invariant under local gauge transformation $\psi \rightarrow \psi' = e^{i\alpha(x)}\psi$ we have to introduce an extra term in the Dirac Lagrangian which corresponds to electromagnetic interaction and the Lagrangian becomes:

$$\mathcal{L} = i\bar{\psi}\gamma^\mu\partial_\mu\psi - m\bar{\psi}\psi + \frac{-1}{4}F_{\mu\nu}F^{\mu\nu} - j^\mu A_\mu, \quad (1.5.4)$$

1.5.0.1 Higgs Mechanism and Higgs Boson

The electromagnetic and weak force can be described with the same theory, thus with this unification we can say that electromagnetic and weak forces can be treated as a single force known as the electroweak force.

The unification theory correctly explains the electromagnetic and weak field and associated force carrying particles but the problem is, according to this theory all the mediators are massless but W and Z bosons have mass up to 100 times of mass of proton. The theory which solve this puzzle is called Higgs mechanism. Which says that W and Z bosons acquire mass with the interaction of invisible field called Higgs field.

To understand the electroweak interaction we have to construct Lagrangian that is invariant under the $SU(2) \times U(1)$ transformation. But we know that W and Z bosons are massive and with the mass term in Electro-weak Lagrangian we must break the gauge invariance. We can write the Lagrangian for weak interaction ⁵:

$$\mathcal{L} = \bar{\psi}i\gamma^\mu\partial_\mu\psi + i\frac{f}{2}\tau.W_\mu\psi - \frac{1}{4}W_{\mu\nu}W^{\mu\nu}, \quad (1.5.5)$$

here the last term corresponds to weak field tensor.

But we need mass for the W and Z boson and with the mass term Lagrangian is no more gauge invariant, so we have to break the gauge symmetry. So together with mass term in Lagrangian along with gauge symmetry we introduce a Lagrangian:

$$\mathcal{L} = \frac{-1}{4}B_{\mu\nu}B^{\mu\nu}, \quad (1.5.6)$$

where $B_{\mu\nu} = \partial_\mu B^\nu - \partial_\nu B^\mu$ and it transforms like A^μ

$$B^\mu \rightarrow B'\mu = B^\mu + \partial^\mu\Lambda, \quad (1.5.7)$$

⁵For detail see chapter 14 of Quarks and Lepton: An introductory course in Modern physics by Francis Halzen Alan D.Martin

where Λ is some scalar function and B^μ is some vector field. The Lagrangian becomes:

$$\mathcal{L} = \frac{-1}{4} B_{\mu\nu} B^{\mu\nu} + \mathcal{L}_{scalar}, \quad (1.5.8)$$

$$\mathcal{L}_{scalar} = (D_\mu \phi)^* (D^\mu \phi) - V(\phi^* \phi), \quad (1.5.9)$$

$$D_\mu = \partial^\mu - \iota g B^\mu, \quad (1.5.10)$$

and ϕ is some complex field given by $\phi(x) = e^{i\phi(x)} (\frac{v+h(x)}{\sqrt{2}})$, and $B^\mu \rightarrow B'^\mu = B^\mu + \frac{1}{g} \cdot \partial^\mu \theta$. Now If we make a gauge transformation

$$\phi \rightarrow \phi' = e^{i\theta} \cdot \phi, \quad (1.5.11)$$

$$B_\mu \rightarrow B'_\mu = B_\mu + \frac{1}{g} \partial^\mu \theta, \quad (1.5.12)$$

we also have a mass term in the Lagrangian which can be written as:

$$M_B = \frac{g^2 v^2}{2}, \quad (1.5.13)$$

and energy term:

$$V = \lambda(\phi^* \phi - \frac{v^2}{2})^2, \quad (1.5.14)$$

thus for minimum energy of scalar field ϕ by setting $\frac{\partial V}{\partial \phi} = 0$ we get:

$$\langle \phi \rangle = \begin{pmatrix} 0 \\ \frac{v}{\sqrt{2}} \end{pmatrix} \quad (1.5.15)$$

corresponds to vacuum. This means when we say vacuum we don't have presence of physical particles or physical fields. Then quantum fluctuation or particles can be created by giving energy greater than $\langle \phi \rangle$. Thus presence of $\langle \phi \rangle$ (Higgs field) gives the mass M_B through the interaction of B_μ field with ϕ Higgs field. The physical particles that corresponds to ϕ are

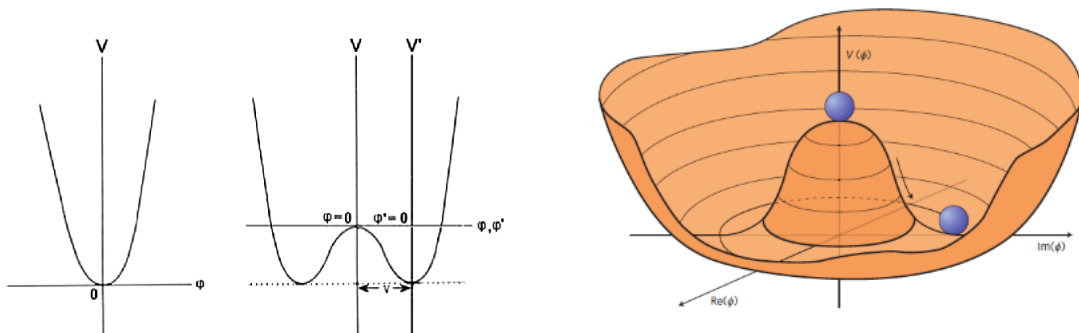


Figure 1.5: The potential V of a complex scalar field ϕ [13]

h 'Higgs Boson'. The vacuum potential configuration does not have $\phi = 0$ state and the field is said to have a non-zero vacuum expectation value v , Due to symmetric configuration of vacuum potential there will be two degenerate states, any vacuum state of the field will have $\phi = +v$ or $\phi = -v$ value. Thus the choice of any vacuum state breaks the symmetry of the Lagrangian,

also called *spontaneous symmetry breaking*. The masses for the vector bosons can be expressed in terms of ν and the electroweak coupling constant g :

$$m_W = \frac{1}{2}\nu g \quad m_Z = \frac{m_w}{\cos\theta_W} = \frac{1}{2}\nu\sqrt{g^2 + g'^2} \quad (1.5.16)$$

Where θ_W is defined by:

$$\tan\theta_W \equiv \frac{g'}{g} \longrightarrow \sin^2\theta_W = 1 - \frac{m_W^2}{m_Z^2}, \quad (1.5.17)$$

1.6 Hadron Collider Physics

Hadrons are the bound colourless states of quarks confined by gluon interactions, of which the proton is a stable example. Collisions in high energy experiments result in the hard or high- Q^2 scattering of accelerated particles dominating interactions between composite particles, which produce additional soft-QCD processes. This results in a perturbative high energy process and a non-perturbative low energy background present in proton-proton collisions.

In hadron collision experiments at a sufficiently high momentum transfer, one can approximate all partons as free particles. Thus hadron-hadron interaction can be thought of as single parton-parton interaction. [14]. The parton momentum can be expressed in terms of the fraction of the hadron momentum $p_{parton} = x.p_{hadron}$, where x is also referred as "Bjorken scaling variable". Then, the probability of finding two parton flavors f_I with momentum fraction x_i interacting at an energy scale μ_F in a hadron-hadron collision is given by the parton distribution function (PDF) as $\text{PDF}(x_1, f_1\mu_F)$ and $\text{PDF}(x_2, f_2, \mu_F)$ which will be discussed in detail in chapter 3.

In other words, at sufficiently high energies, interactions between the constituents of a proton are neglected. This allows factorisation of the perturbative calculable partonic cross section from that of the overall interaction, assuming asymptotic freedom for each possible set of initial states. Each contribution is weighted by the relevant parton distribution functions (PDFs), which act as the parameterisation of the contents of hadrons in the collisions taking place.

$$\sigma_{AB \rightarrow x} = \int dx_A dx_B f_a(x_a, \mu_F, \mu_R) f_b(x_b, \mu_F, \mu_R) \sigma_{ab} \rightarrow x \quad (1.6.1)$$

The factorisation theorem provides the hadronic cross section in these terms, where A and B are the colliding hadrons, a and b are the scattered partons and $f_a(x_a, Q^2)$, $f_b(x_b, Q^2)$ are the PDFs for parton a and b . The partonic cross section depend upon $\alpha_s(\mu_R^2)$, where μ_R and μ_F are the re-normalisation and factorisation scale and x is independent of the number of final state particles or kinematic configuration.

CHAPTER 2

The Large Hadron Collider

The Large Hadron Collider (LHC) [15] is the most powerful particle accelerator that can accelerate the particles near to the speed of light. The accelerator is located in an underground tunnel 100 metres deep, at the European Organization for Nuclear Research (CERN), Switzerland. The length of LHC is 27-kilometre and has number of accelerators and detectors around its length as shown in Fig. 2.1.

In LHC two proton beams are accelerated and made to collide at four different collision points around the ring of LHC. LHC uses superconducting magnets which guide the particle beams. These magnets are kept at very low temperature and in ultra high vacuum. The data from the collision of beams are gathered in CERN control center and stored for the further analysis.

2.1 Detectors at Large Hadron Collider

There are many experiments that are currently being performed in the LHC. In these experiments four major experiments are ATLAS, ALICE, CMS and LHCb [16]. There are several other small experiments installed at LHC namely, TOTEM, MoEDAL and LHCf.

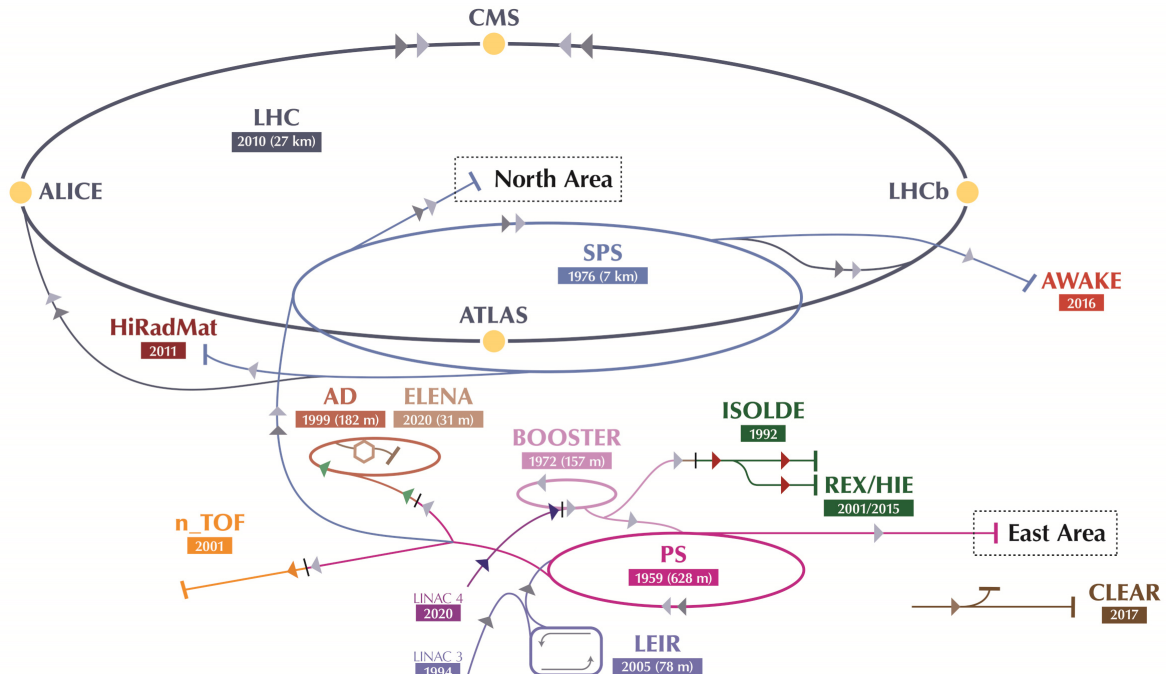


Figure 2.1: Schematic layout of the LHC experiment at CERN, figure taken from [16]

2.1.0.1 A Toroidal LHC Apparatus (ATLAS)

ATLAS [17] is general purpose detector designed to study a wide range of particle physics including Higgs boson, top quark physics and physics beyond Standard Model. ATLAS shown in Fig. 2.2 has a large magnetic system which is in the shape of doughnut. This has cylindrical shaped superconducting magnetic coils of 25 m long. ATLAS is the largest Collider detector ever constructed.

Table 2.1: Parameters of LHC detectors

ATLAS	
Size	$46m \times 26m \times 26m$ (length,height,width)
Weight	7000 tonnes
Material cost	540 MCHF
Location	Meyrin, Switzerland
CMS	
Size	$21m \times 15m \times 15m$ (length,height,width)
Weight	≈ 13000 tonnes
Material cost	500 MCHF
Location	Cesssy, France
LHCb	
Size	$21m \times 10m \times 13m$ (length,height,width)
Weight	≈ 6000 tonnes
Material cost	75 MCHF
Location	Ferney-Voltaire,France
ALICE	
Size	$26m \times 16m \times 16m$ (length,height,width)
Weight	≈ 10000 tonnes
Material cost	115 MCHF
Location	Sergy,France
LHCf	
Size	30cm long, 60m high and 10m wide
Weight	40kg
Location	Meyrin, Switzerland (near ATLAS)
TOTEM	
Size	44m in length having 8 detectors
Weight	≈ 20 tonnes
Design	Roman pot, GEM detectors and cathode strip chambers
Material cost	6.5 MCHF
Location	France (near CMS)

2.1.0.2 Compact Muon Solenoid (CMS)

CMS [18] is also another general purpose experiment as ATLAS, but constructed with a different technical design. CMS has a large solenoided shape super magnet which can generate a field of 4 T. The CMS has a unique and compact design compared to ATLAS shown in Fig. 2.3.

2.1.0.3 Large Hadron Collider beauty (LHCb)

LHCb [19] is designed to study of B-particles (particles have b-quarks) to understand the asymmetry between matter and antimatter. It is shown in Fig. 2.4.

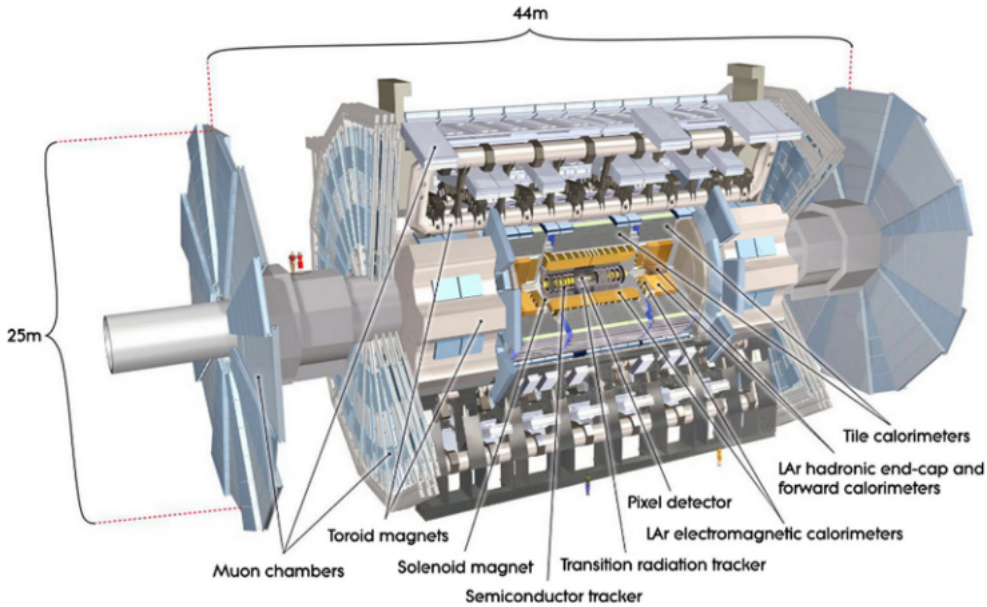


Figure 2.2: Inner view of ATLAS detector, figure taken from [20].

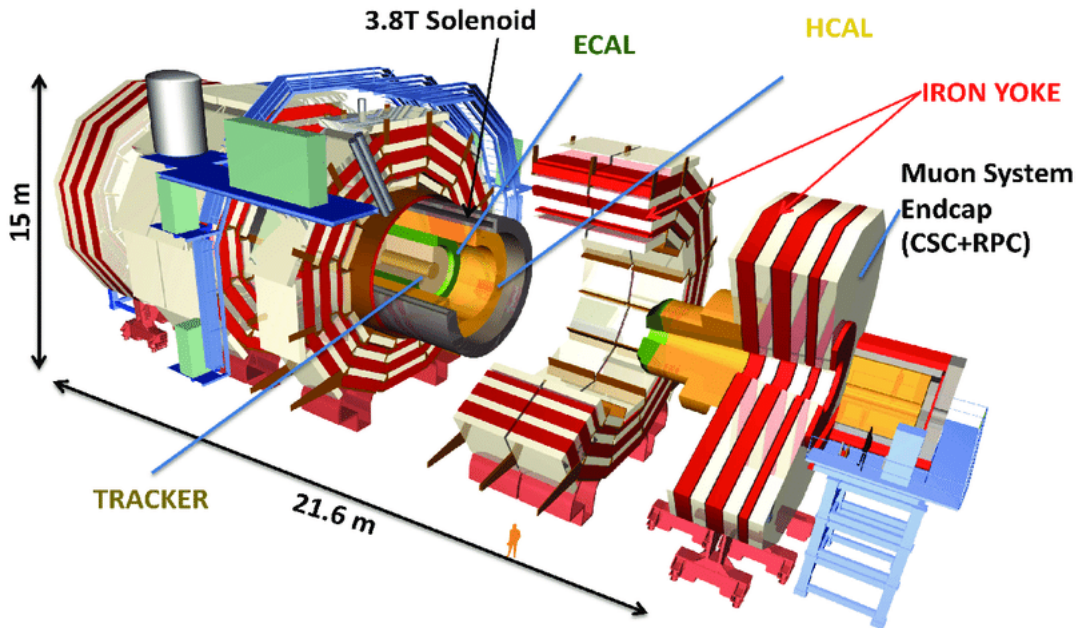


Figure 2.3: Schematic illustration of the CMS detector, figure taken from [21].

2.1.0.4 A Large Ion Collider Experiment (ALICE)

The ALICE [22] is designed to study the properties of quarkgluon plasma, a rare state of matter. Quark-gluon plasma is the state of matter under very high temperature and densities in which quarks are free and not confined inside a hadron.

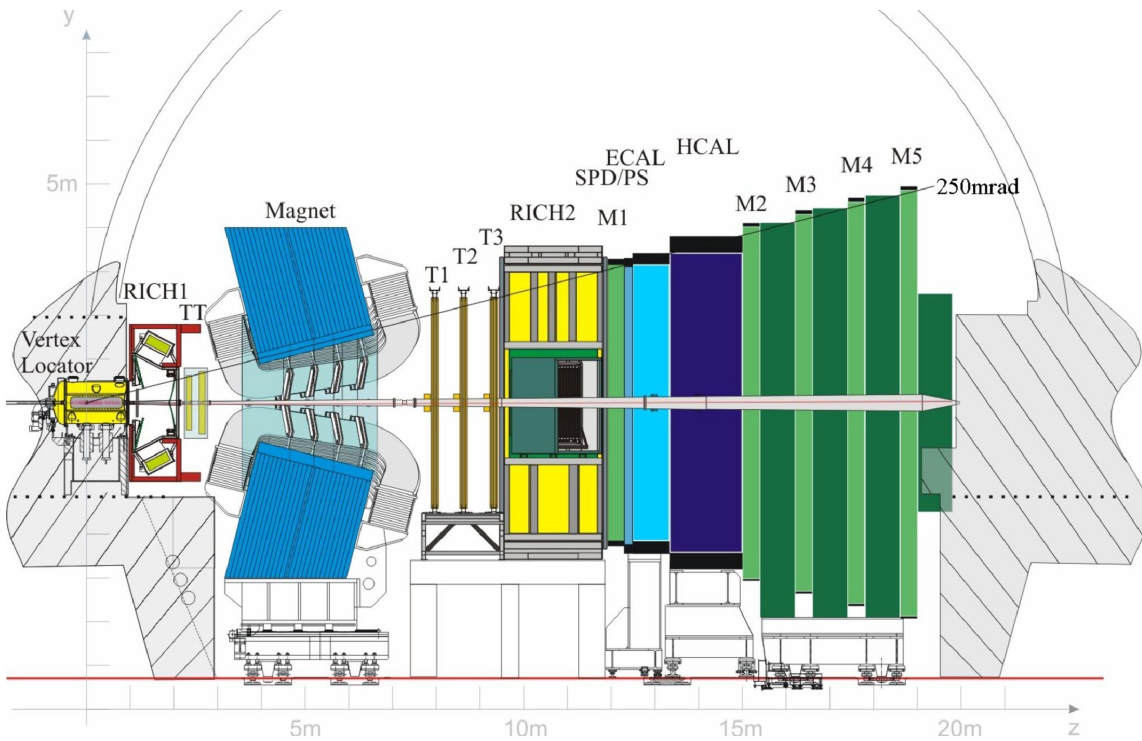


Figure 2.4: Inside view of the LHCb detector at LHC, figure taken from [14].

2.1.0.5 Large Hadron Collider Forward (LHCf)

The large hadron collider forward (LHCf) [23] is a small experiment that is designed to study different aspect of nuclear physics.

2.1.0.6 TOTEM

TOTEM [] is designed to measure the total cross section, elastic and diffractive scattering of the proton. TOTEM is able to detect particles that are produced very close to the beam pipe of LHC. The TOTEM is placed in a specially designed vacuum chambers called Roman pots. These Roman pots are connected to the beam pipes around LHC. There are total of 26 Roman pots in LHC which are located near CMS experiment as shown in Fig. 2.5.

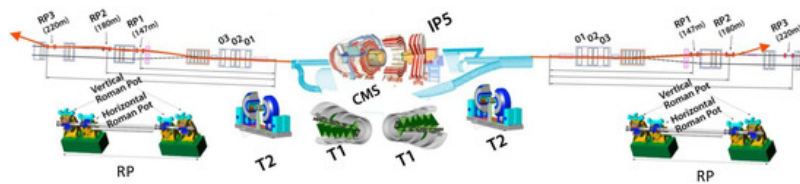


Figure 2.5: Sketch of the TOTEM and CMS experiments at the LHC figure taken from [4]

2.2 Parameters Of LHC

2.2.1 LHC Co-ordinate System

The CMS and ATLAS detectors work using the right-handed cartesian system with center being the origin of the co-ordinates at the point where the interaction takes place. The $x - axis$ is

directed towards the center of the hadron collider, the $y - axis$ is directed in the upward direction that is perpendicular to the ground whereas the third $z - axis$ is parallel to the proton beam, as shown in Fig. 2.6. The polar angle, θ , is the angle measured w.r.t the beam axis. The azimuthal angle, ϕ , is the angle between the x-y planes. The distance Δr between two particles is defined in the $\eta - \phi$ plane as

$$\Delta r = \sqrt{\Delta\eta^2 + \Delta\phi^2} \quad (2.2.1)$$

where $\Delta\eta = |\eta_a - \eta_b|$, $\Delta\phi = |\phi_a - \phi_b|$ and η, ϕ are polar and azimuthal angle of the particle tracks.

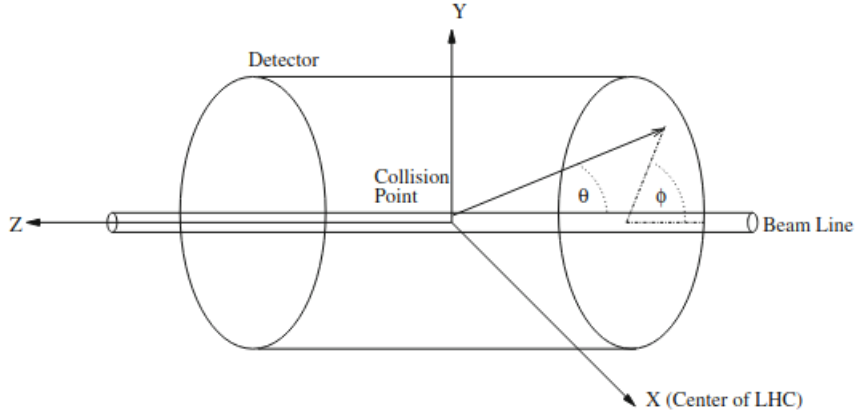


Figure 2.6: ATLAS and CMS coordinate system, figure taken from [20]

2.2.2 Pseudo rapidity

In hadron collider physics, a useful term defined as rapidity of the particle is given as

$$y = \frac{1}{2} \ln \frac{E + p_z}{E - p_z} \quad (2.2.2)$$

where p_Z is the momentum of particle along $z - axis$. The term pseudo rapidity ' η ' is derived from rapidity, commonly measured in polar angle θ with respect to beam axis. Pseudo rapidity is defined by the equation $\eta = -\ln(\tan \frac{\theta}{2})$.

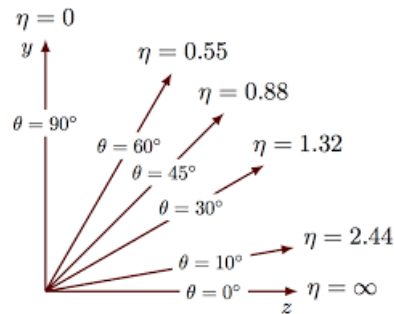


Figure 2.7: Pseudo rapidity values in 1st quadrant

where ' θ ' is the angle between particle direction and beam direction. The transverse momentum ' p_T ' is defined as the component of particle momentum in x-y plane. The transverse energy is defined as $E_T = E \sin \theta$.

The energy which is carried by non detectable particles is called missing energy, because these particles have no interaction through strong or electromagnetic forces, these particles are called neutrinos. In general, missing energy arises due to presence of non-detectable particles in the detector. The particle travelling in transverse direction to the beam axis have zero initial momentum, so if we have final momentum in x or y direction, it represents the missing transverse energy, because the total transverse momentum of initial state is zero, sum of final state particles transverse direction should also be zero. Missing transverse momentum [24] can be defined by following equation,

$$\vec{E}_T^{missing} = -\sum_i \vec{p}_T^i \quad (2.2.3)$$

Where, the index i sums over all visible particles. The assumption that transverse energy and momentum are equal, holds only for particles that are massless. The missing transverse momentum is defined as

$$\vec{p}_T^{missing} = -\sum_{i=1}^N \vec{p}_T^i \quad (2.2.4)$$

In an event N is the total number of final state particles. The p_T and $p_T^{missing}$ are invariant under Lorentz boost along the beam direction which is $z-axis$. For particles of mass very smaller than their energy ($m \ll E$) the rapidity can be approximated by pseudo rapidity η .

2.2.3 Luminosity

Luminosity [25] is a important parameter of the accelerator. To observe new phenomena in experimental high energy physics, we required high center of mass energy such as up to 14 TeV , as well as large number of useful interactions. These useful interactions are used to reconstruct data for the analysis. In the study of rare events with very small cross section σ , luminosity becomes more important. The total number of interactions that an accelerator can produce is called its luminosity and it is the proportionality factor between event production rate $\frac{dR}{dt}$ and the cross section σ :

$$\frac{dR}{dt} = \mathcal{L}_{ins} \cdot \sigma \quad (2.2.5)$$

Luminosity can be defined simply by, ratio of the number of events produced (dN) in a certain time (dt) to cross section σ .

$$\mathcal{L}_{ins} = \frac{dN}{\sigma dt} \quad (2.2.6)$$

The unit of luminosity is $\text{cm}^{-2}\text{s}^{-1}$. The rate of collisions also relate to instantaneous luminosity \mathcal{L}_{ins} as:

$$N = \mathcal{L}_{ins} \times \sigma \quad (2.2.7)$$

Where σ is cross section of expected process. Equation 2.2.7 shows that the instantaneous luminosity cannot be kept stable during the data taking [26]. \mathcal{L} decreases due to loss of protons in bunches, which leads to decrease in collision rate. Therefore, another useful quantity in detector physics integrated luminosity \mathcal{L}_{int} is introduced by integrating the instantaneous luminosity over time, having units inverse barns denoted by b^{-1} (per cm^2). It is used to measure how much data is recorded by LHC and CMS.

The data acquisition system of detector is not always 100 % efficient due to which the amount of data recorded by a detector is usually smaller than the amount of data delivered, and not all the data is good enough for analysis purpose, as some of the subsystems may be in an error state that corrupt the data recorded or other unexpected behaviour of the LHC or CMS may have interrupted the data recording. The total amount of data used in an analysis can be much smaller than the total amount of data delivered. Fig. 2.8 shows the predicted increase in luminosity of CMS detector with center of mass energy.

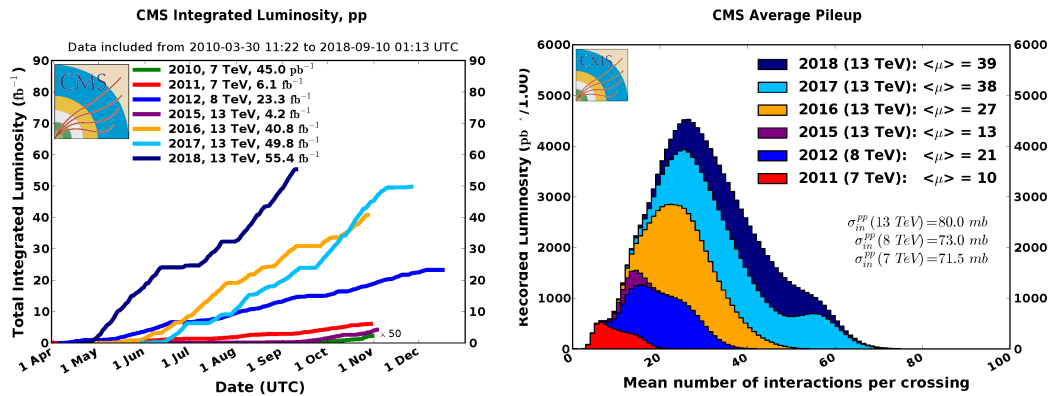


Figure 2.8: \mathcal{L}_{int} delivered to CMS versus data taking period for pp collisions at different LHC energies. The distribution of $\langle \mu \rangle$ versus luminosity recorded by CMS for the 2011 - 2012 and 2015 - 2018 data taking period figure adopted from [25].

2.2.4 Pile-up (PU)

Another important parameter of the accelerator is pileup. During a bunch crossing multiple proton-proton interactions can occur which are referred to as pileup. These interactions are proportional to the event cross section times luminosity. There are two types of pileups:

- in-time PU comes from the collisions happening in the same bunch crossing.
- out-of-time PU comes from the collisions from the previous bunch crossings whose signal has not yet been recorded by the detector.

In-time PU is calculated by the number of primary vertices (N_{PV}) while out-of-time PU is parametrized by the mean number of interactions per bunch crossing (μ). In 2012 an average of 21 pileup interactions was observed at 8 TeV. This increased in 2016 due to the higher luminosity and cross section at 13 TeV, to about 27 interactions on average.

2.2.5 Beam Spot

This spot is the brightest region where the two beams travelling in opposite direction are brought into collision. It is an important and an essential parameter for the computation of different parameters which are used in further data analysis. It is very necessary to measure beam spot very accurately and precisely, especially the beam spot width, the value of beam spot width is further used by computation procedure of different observables. It is also a reference point for studying the track performance.

2.3 CMS Detector

The Compact Muon Solenoid (CMS) [18], as the name represents is compact due to small size when compared to ATLAS detector, muon is a fundamental particle detected by CMS, and solenoid for the large superconducting magnet. The side view of CMS detector is shown in Fig. 2.9. The scientific goals of CMS experiment are same as for the ATLAS. After the discovery of Higgs boson, the study of Higgs boson properties in detail and search for the physics beyond the Standard Model are the main goals of CMS experiment. CMS has a different technical

solution, especially its magnetic system design.

The CMS detector built 100m underground in France countryside, near the village of Cessy. One of the main goals to built CMS experiment was the search of Higgs boson that is responsible of electroweak symmetry breaking. This goal was achieved in 2012 by the discovery of scalar boson named "SM Higgs Boson" [27]. CMS experiment covers many aspects of proton-proton collisions at very high center of mass energy i.e. (14 TeV) of the LHC. Some of the main characteristics of CMS are as follows:

- CMS provides a better muon identification and momentum measurement over wide range of angle.
- CMS tracking system provides good identification of the charged particles.
- A wide geometric coverage, better electromagnetic energy resolution.

2.3.1 Structure of CMS

The CMS detector has a long cylinder of length 21.6 m with a diameter of 15 m and weight 12500 tons. It is designed to operate at a center-of-mass energy of 14 TeV and a luminosity of $10^{34} \text{ cm}^{-2}\text{s}^{-1}$. The CMS uses superconducting solenoid magnet that surrounds all the inner detectors. CMS is equipped with different types of silicon tracker, i.e., silicon pixel and strip tracker, lead-tungstate (PbWO_4) Electromagnetic Calorimeter and a brass scintillator sampling Hadronic Calorimeter. An iron yoke which holds both superconducting solenoid and muon detector.

CMS has also right handed coordinate system, with the origin at the interaction point of beam inside the detector. CMS has cylindrical symmetry, it is convenient to use cylindrical co-ordinates (r, θ, ϕ) shown in figure 2.10.

The CMS structure can be summarized as below:

- The interactions between bunches of particles take place at the core of the apparatus with a maximum instantaneous luminosity of $21 \text{ nb}^{-1}\text{s}^{-1}$ achieved in LHC RUN 2.
- The inner part of detector is silicon tracker which extend from interaction point to $|r| < 1.2\text{m}$, covering $|\eta|$ range < 2.5 .
- The Electromagnetic calorimeter (ECAL) extends over $1.2\text{m} < r < 1.8\text{m}$ and covers pseudo-rapidity range $|\eta| < 1.3$.
- The Hadronic Calorimeter (HCAL) covers $1.8 \text{ m} < r < 2.9 \text{ m}$ by covering $|\eta| < 5$.
- The superconducting solenoid magnet provides a magnetic field of 4 T along the beam direction, which bends the charged particles trajectories in order to measure their momentum. The solenoid surrounds all the inner detectors and extends from $2.9 \text{ m} < r < 3.8 \text{ m}$ over $|\eta| < 1.5$.
- The muon system is the outer most part of the CMS detector. It is extended from $4 \text{ m} < r < 7.4 \text{ m}$ and covers $|\eta| < 2.4$.

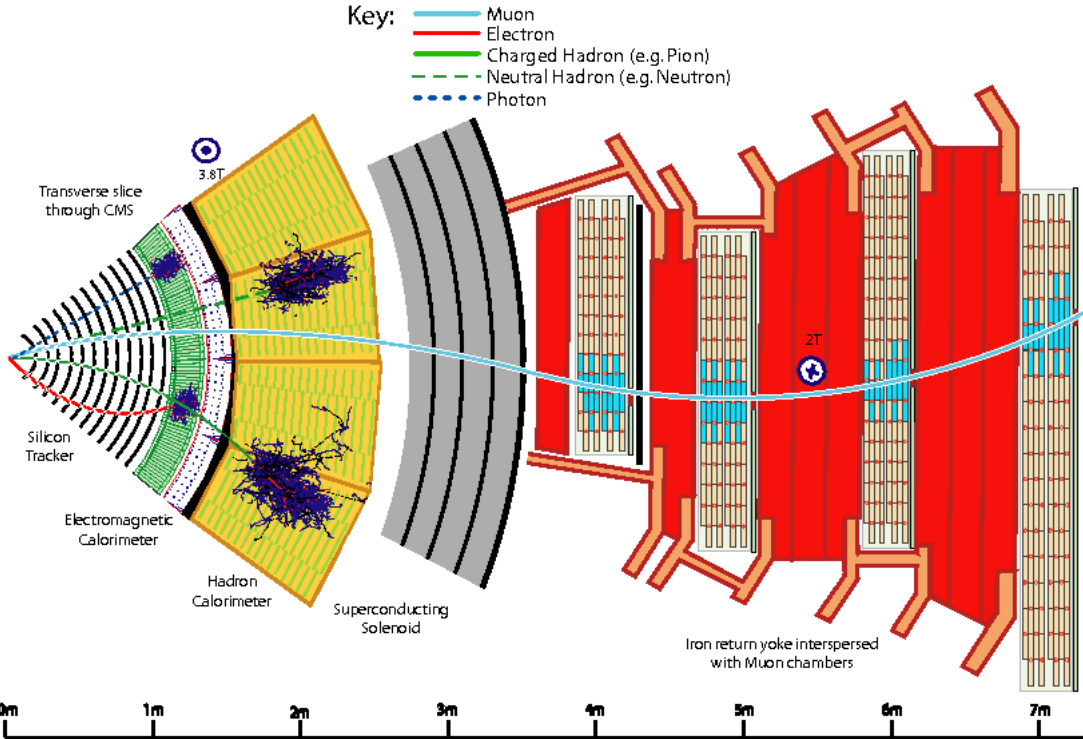


Figure 2.9: Cut view of CMS detector, the distance of different components from center is illustrated in figure taken from [28]

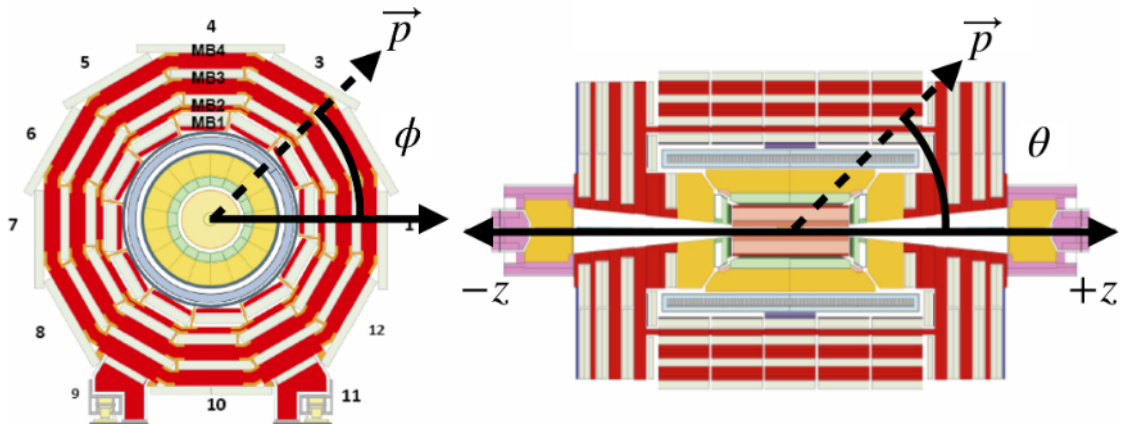


Figure 2.10: Polar coordinates used by CMS. Figure taken from reference [29].

2.3.2 CMS Tracker

The tracker is located very close to the interaction point as shown in Fig. 2.11 hence it receives the largest number of particles produced. The tracker is designed to measure highest resolution of charged particles trajectories with transverse momentum up to 1 GeV in a range $|\eta| = 2.5$. At LHC design luminosity of about $10^{34} \text{ cm}^{-2}\text{s}^{-1}$, the tracker records roughly 100 tracks per bunch crossing, i.e., for every 25 ns . So it is necessary to choose the construction material carefully to resist high radiation and particle flux.

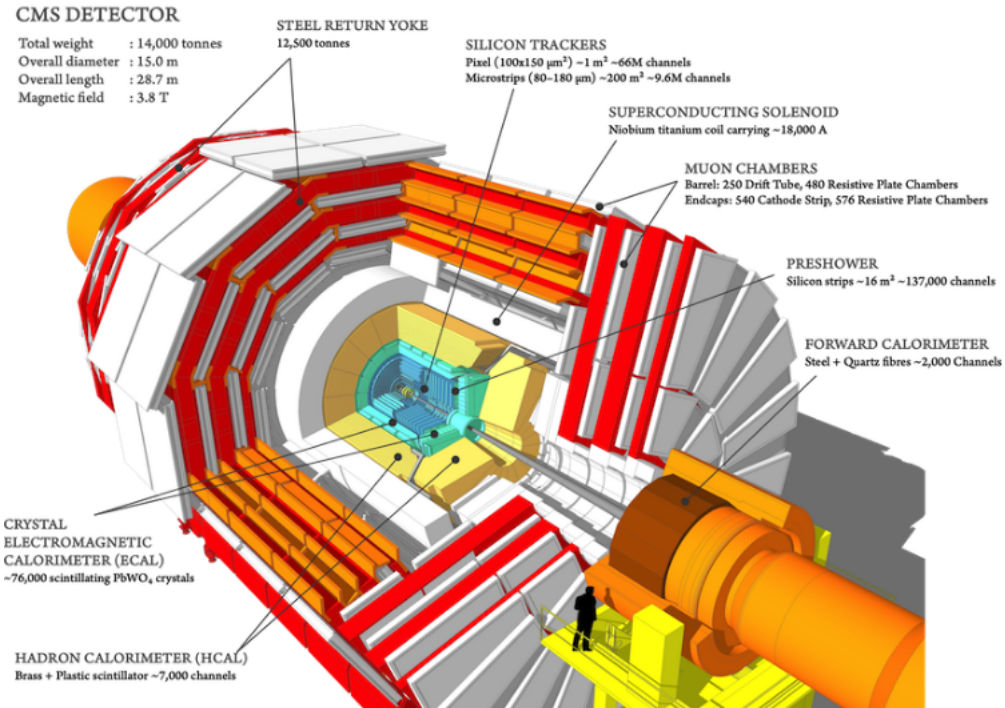


Figure 2.11: Schematic view of CMS detector. Figure taken from [30].

2.3.3 Electromagnetic Calorimeter (ECAL)

The ECAL [31] sits in between the tracker and Hadron Calorimeter (HCAL). It is designed to detect and measure the energy of photons, electrons and positrons with great precision. There are three partitions in ECAL: Barrel, End caps and Pre shower. The ECAL barrel (EB) has 61200 PbWO_4 crystals, in a cylindrical shape design that begins at a radius of 1.29 m and covers the range $|\eta| < 1.479$. The barrel has a number of module and super module. The barrel region is complemented by 7324 crystals that are mounted on two end caps located at 314 cm from the vertex and cover the range $1.47 < |\eta| < 3.0$.

The pre shower detector is placed in front of the end cap crystal and covers a range of $1.653 < |\eta| < 2.6$. It discriminates the electromagnetic shower formed by the photons, coming from the neutral pion decay. It also helps to identify the position of electrons and photons. The layout of ECAL can be seen in Fig. 2.12.

2.3.4 Hadron Calorimeter (HCAL)

The Hadron Calorimeter [32] is designed for the study of many processes, which include energy and direction of hadronic jets, reconstruction of the hadron decays and missing transverse energy in the events. There are four modules of HCAL, the hadron barrel (HB), hadron calorimeter end caps (HE), the outer calorimeter (HO), and the forward calorimeter (HF).

The hadron barrel (HB) shown in Fig. 2.13 sits in between ECAL and superconducting magnetic coil at a distance $1.77 \text{ m} < r < 2.95 \text{ m}$. The hadron calorimeter end caps (HE) cover the solid angle between $1.3 < |\eta| < 3$. The hadron barrel (HB) calorimeter measures 860 cm in length with inner and outer radius of 177 cm and 295 cm respectively. HB is divided into two half-barrel HB+ and HB-. The end caps of HE cover range $1.3 < \eta < 3.0$. The HB+ and HB- have thirty six identical wedges. Each wedge is constructed from flat steel and brass plate and is

aligned parallel to beam axis. The HE is also radially divided into 14 rings. The HO of HCAL is made with plastic scintillator in several layers and the most outer part of HCAL is HO which is 11.2 m away from the collision point.

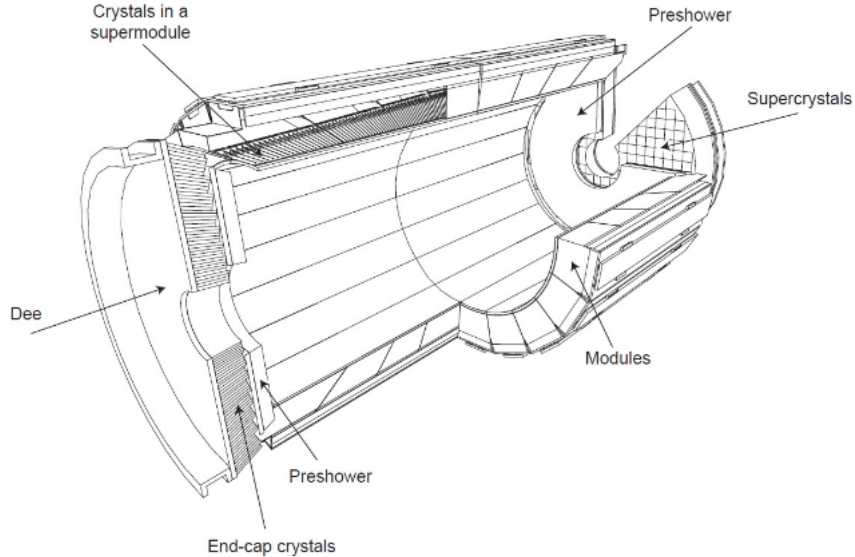


Figure 2.12: CMS ECAL layout, figure taken from [18].

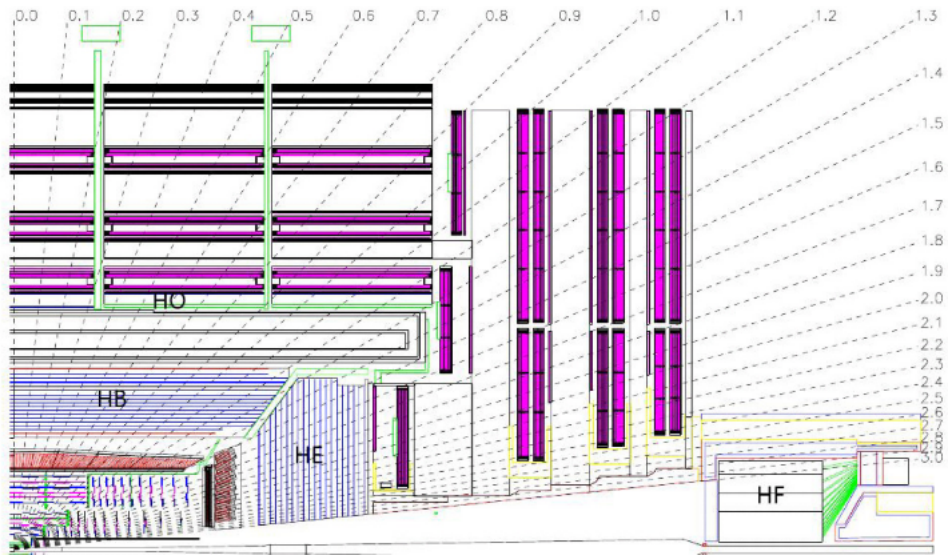


Figure 2.13: Layout of CMS HCAL, figure taken from [18].

2.3.5 Magnetic System of CMS

The distinct feature of CMS is its superconducting magnet [33] designed to provide magnetic field of 4 T in a region of length 12.5 m and 6 m in width, one of the biggest solenoid ever made.

In CMS detector we need high magnetic field to bend particle trajectories which is obtained by combination of different magnets made by NbTi cables. The energy stored at an operating temperature of 4.6 K and at full current is $\approx 2.6\text{ GJ}$. The magnetic flux of these coils is returned through an iron yoke weighing 10,000 *tons*. It is shown in Fig. 2.14.

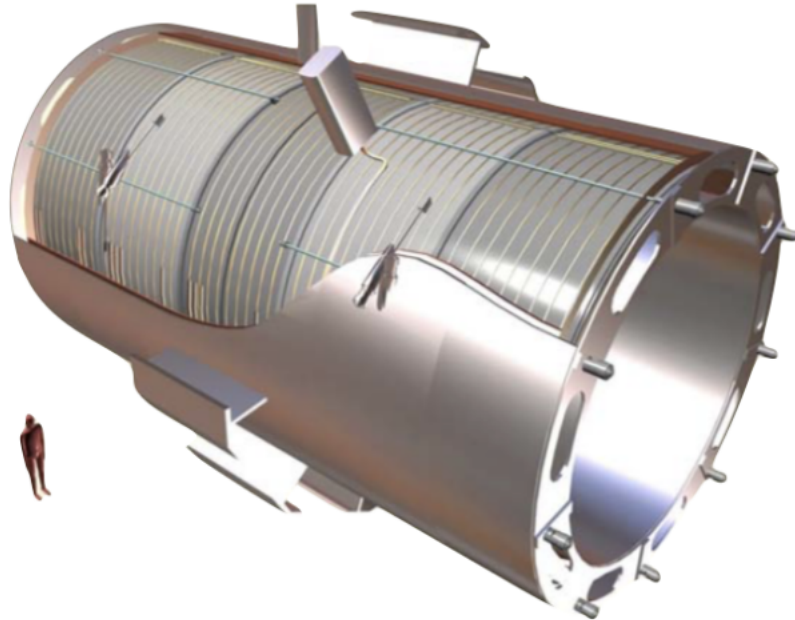


Figure 2.14: View of CMS superconducting solenoid. Figure adopted from [18].

2.3.6 CMS Muon System

The CMS muon system [34] is specially designed to detect muons with high transverse momentum. Its main function is to identify muon, measurement of its momentum and triggering. The muon system of CMS is divided into three independent subsystems, which consist of three gaseous particle detectors, the drift tube system, cathode strip chambers and the resistive plate chambers.

2.3.6.1 Drift Tube Chamber

The barrel region of CMS muon system is instrumented with drift tube (DT) chambers covering the pseudo-rapidity range up to $|\eta| = 1.2$. The DT chambers arranged into five iron wheels, each wheel have four concentric ring called stations. The function of these stations is to measure the muons coordinates in the transverse plane as well as its z direction.

The detector of this chamber is a drift tube of rectangular shape of size $13 \times 42 \text{ mm}^2$ and having length $2 - 4 \text{ m}$. The whole volume is filled with gas mixture of 85% argon and 15% carbon dioxide.

2.3.6.2 Cathode Strip Chamber

The cathode strip chamber is installed at the end cap of CMS muon system. This chamber is designed especially to identify muons in the region $0.9 < |\eta| < 2.4$. The chamber is divided into four stations for each end cap, perpendicular to the beam pipe and separated by the flux return plate as can be seen in Fig. 2.15.

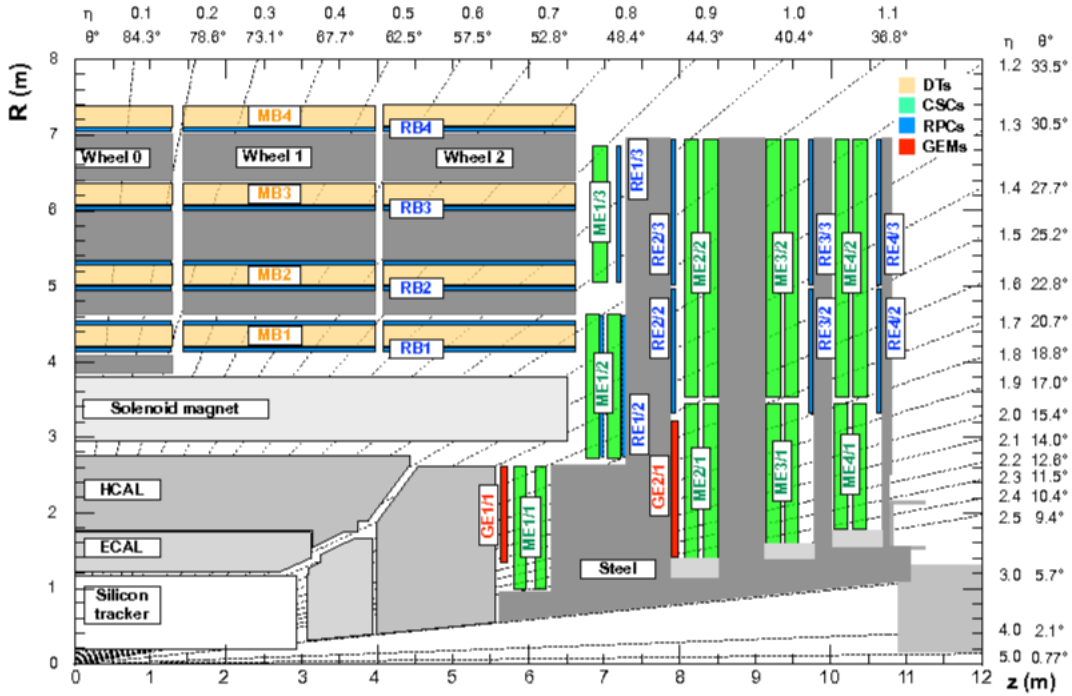


Figure 2.15: CMS muon detector system. Figure adopted from [34].

The cathode strip chamber is filled with 40% argon and 50% carbon dioxide as active gas and remaining 10% with carbon tetrafluoride. This chamber is arranged in four disks called stations, each of which has two rings divided into eighteen or thirty six CSCs. These stations are equipped with sensitive wires which provide muon recognition.

2.3.6.3 Resistive Plate Chamber

The resistive plate chambers (RPC) are installed at both barrel and end cap regions. They are also gaseous detector. The RPCs are made of four Bakelite planes coated with graphite which act as the electrode and two gas gaps of 2mm.

2.3.7 CMS Trigger System

LHC provides proton-proton and heavy ions collisions at a very high rate as shown in Fig. 2.16. High particle density in each bunch corresponds to an event rate of 40 MHz with 20 head-on collisions per event, thus interaction rate exceeds 1 GHz. Such a high data stream cannot be handled with current available technology. Therefore, CMS experiment uses a dedicated trigger system. The trigger system selects possible events of interest among all the simultaneous events occurring.

The trigger system [35] is divided into two main stages:

1. Level-1 trigger (L1) system consists mainly of programmable electronic components.
2. High Level Trigger (HLT) system is fully software based.

The L1 trigger preselects events of interest in order to be further analysed by the HLT. L1 trigger is responsible for the identification of different leptons, quark jets and missing transverse energy. It consists of three main subsystems:

- Calorimeter Trigger
- Muon Trigger
- Global Trigger

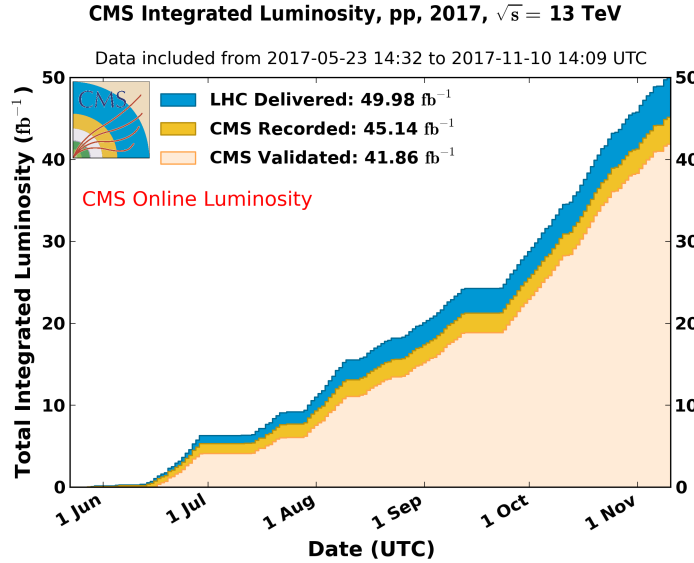


Figure 2.16: CMS recorded luminosity at 13 TeV .

The event selection at the **HLT** [36] is similar to that used in the offline processing. HLT reconstructs the leptons, jets and applies the identification criteria in order to select only those events which are of possible interest for data analysis. A view of the CMS L1 trigger is shown in Fig. 2.17.

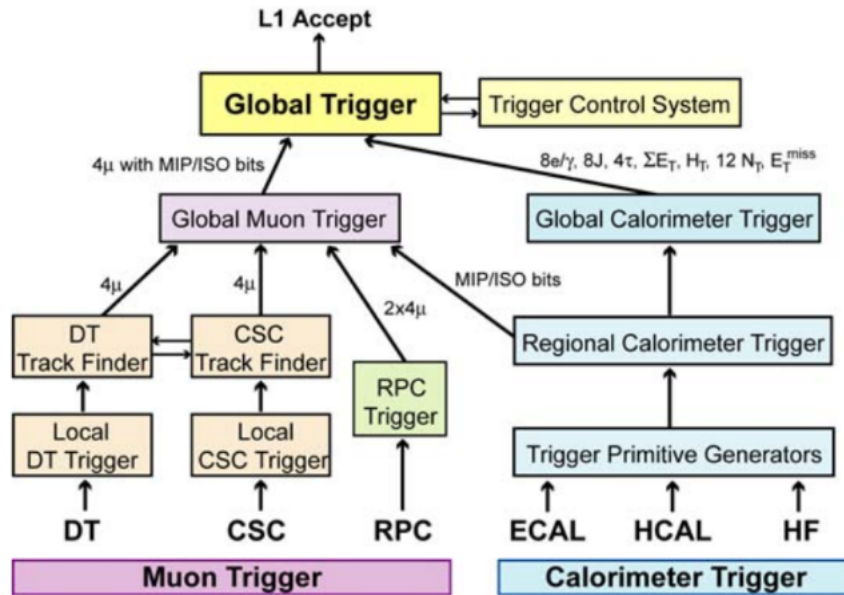


Figure 2.17: The L1 trigger system of CMS, figure taken from [18].

CHAPTER 3

Theory of Single Vector Bosons

The vector boson production cross section measurement during hadron collision, provides a deep understanding of quantum chromodynamics (QCD) and electroweak (EW) processes. The production of W and Z bosons are best examples of hard scattering processes at Large Hadron Collider. Theoretical predictions in perturbative chromodynamics are available at next-to-next-to-leading order (NNLO) [37, 38].

The cross sections of Z and W boson and their ratios are experimentally measured by the ATLAS and CMS detector at the Large Hadron Collider (LHC) in proton-proton collisions at various center of mass energies. This thesis presents theoretically predicted cross section of the W and Z boson production cross section in a proton proton collision at $\sqrt{s} = 13 \text{ TeV}$ [39].

3.1 Significance of W and Z Boson Production Cross Section

The W and Z electroweak bosons were discovered at UA1 [40] and UA2 [41], and their detailed measurements have been done at electron-positron and hadron Collider. LEP (Linear electron-positron) performed many accurate measurements for the study of these vector bosons, with a precision of 1 % [42]. At Large hadron colliders, single vector boson production has been performed at various center of mass (C.O.M) energies i.e. $\sqrt{0.63} \text{ TeV}$ at the CERN $Spp\bar{S}$ (Super Proton Anti proton Synchrotron) by UA1 and UA2, at $\sqrt{1.8} \text{ TeV}$ at the Tevatron by CDF (Collider Detector at Fermi lab) [43] and at $\sqrt{1.96} \text{ TeV}$ by D0 (DZero) [44]. There are large number of W and Z events produced in Large Hadron Collider, which help us to measure production cross section of these bosons easily, roughly around 140,000 events for $Z \rightarrow ee$ and 500,000 $W \rightarrow e\nu$ events are recorded with 2.2 fb^{-1} of data. Measurements of production cross section of vector bosons at the $Spp\bar{S}$ and the Tevatron are very important, as these measurements provide data for the development of leading-order (LO) and next-to-leading order (NLO) theoretical predictions and results of these measurements are also used for comparison with data at the LHC. LHC provides measurement of W and Z boson at higher energy regimes, so we can improve our theory of perturbative Quantum Chromodynamics (QCD). The results at higher energy regime also provide more constraints on the parton distribution function (PDF) along with improvement in electroweak precision measurements, i.e mass of charged vector boson W and $\sin^2\theta$. These new measurements of vector bosons at LHC provide deep insight for the study of new physics including measurement of Higgs boson parameters, top quark physics and physics beyond the standard model.

Increase in energy at LHC benefits for the predictions of perturbative QCD, Fig. 3.1 illustrates these benefits. We can reach further lower Bjorken x -value for any process, e.g the production

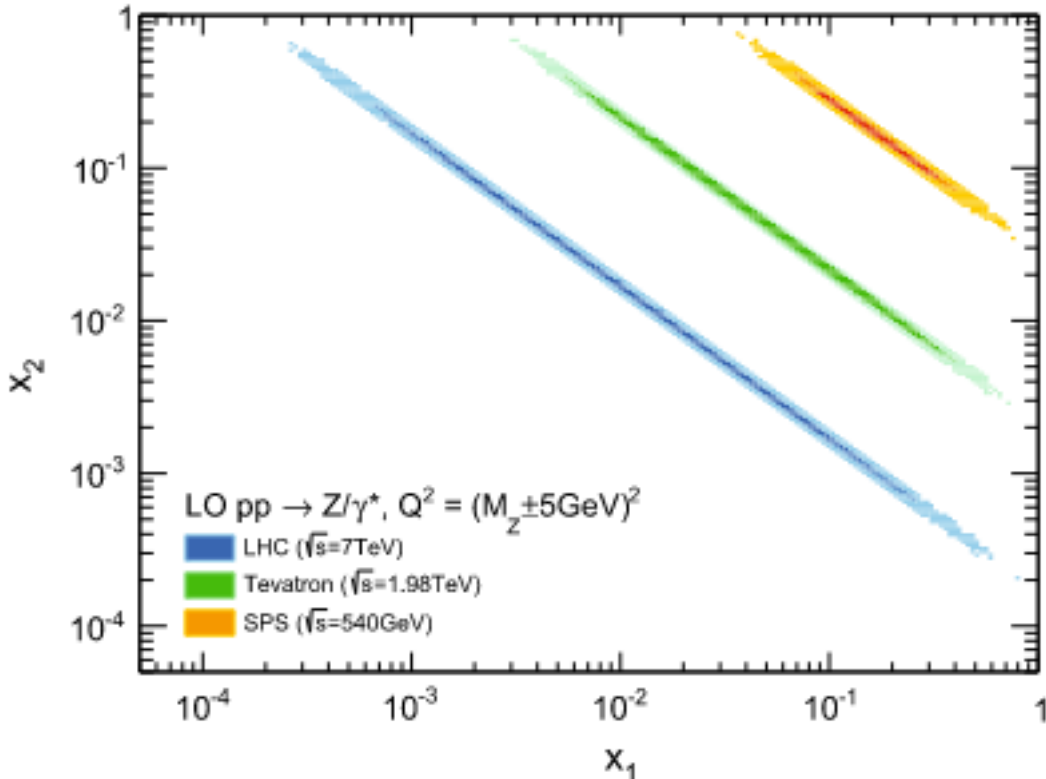


Figure 3.1: Correlation of LHC, Tevatron and SPS hadron Collider between the x values of the interaction of two partons [20]

of Z vector boson shown here. With these new energy regimes we can reach more low x region as compared to SPS and Tevatron experiments. This may improve statistical and systematic uncertainties. Millions of vector boson events have been detected at CMS and ATLAS experiments. These new detectors can measure electrons up to $|\eta| < 4.9$ and jets to $|\eta| < 4.4$ and a large fraction of low- x events can be reconstructed by the LHC detectors.

3.2 Theory of Single Vector Boson Production

The theoretical predictions used for comparison of W and Z boson production cross section have been improved. The theoretical predictions in perturbative QCD theory are available up to next-to-next-to-leading order (NNLO). Theoretical predictions at next-to-leading order(NLO) for the production cross section of vector boson in association with jets exist for five partons in the final state. The uncertainties in theoretical prediction are comparable with experimental uncertainties. We will discuss about different types of theoretical uncertainties in last section of this chapter.

3.2.1 Cross Section Calculation

There are two energy regimes for the calculation of production cross section in proton-proton collisions at Large Hadron Collision(LHC)

- High-energy regime also called short distance regime
- Low-energy regime also called long distance regime

In perturbative QCD there are two terms in the factorization theorem: one is $\hat{\sigma}_{q\bar{q}} \rightarrow n$ at short-distances for the parton-parton interaction and other is for large distances and explain the internal structure of proton. In case of very large momentum transfer q in the interaction of parton, the interactions can be evaluated with perturbative QCD theory. The long-distance term or for low momentum transfer q , where perturbative QCD theory can not be applied, parton density function (PDFs) describes the proton structure. These PDFs Functions can be written as $f_{\frac{a}{A}}(x, Q^2)$ for the parton a in the proton A , in which $x = \frac{p_a}{p_A}$ is shared momentum fraction for parton a from proton's momentum and Q^2 is the energy scale of the scattering process.

The long-distance physics or physics at low momentum transfer and short distance physics or physics at high momentum transfer in parton-parton interaction, is separated by a scale called factorization scale $\mu_F = Q$ [45]. The cross section in the interaction of proton-proton is expressed by

$$\sigma_{p_A p_B \rightarrow n} = \Sigma_q \int dx_a dx_b f_{\frac{a}{A}}(x_a, Q^2) \times f_{\frac{b}{B}}(x_b, Q^2) \hat{\sigma}_{ab \rightarrow n} \quad (3.2.1)$$

as shown in Figure 3.2. $f_{\frac{a}{A}}$ denotes the PDF of parton a and $f_{\frac{b}{B}}$ is for parton b in protons

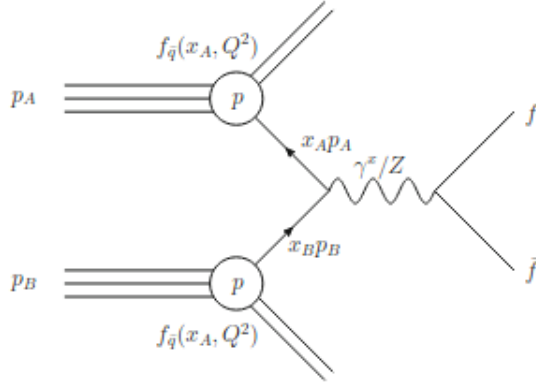


Figure 3.2: Schematic of proton-proton collision at LHC.

A and B respectively. All quark flavours are included in the sum and integration is performed over momentum fraction of parton a , x_a and momentum fraction of parton b , x_b .

If we include the QCD corrections, then parton-parton cross section in term of α_s is,

$$\sigma_{p_A p_B \rightarrow n} = \Sigma_q \int dx_a dx_b f_{\frac{a}{A}}(x_a, Q^2) f_{\frac{b}{B}}(x_b, Q^2) \times [\hat{\sigma}_0 + \alpha_s(\mu_R^2) \hat{\sigma}_1 + \dots]_{ab \rightarrow n} \quad (3.2.2)$$

In Equation 3.2.2, σ_1 is the correction in parton-parton cross section of order one, and σ_0 is the base-level parton-parton cross section. Therefore reference scale for the running strong coupling constant $\alpha_s(\mu_R^2)$ is set by μ_R (re-normalisation scale). The re-normalisation scale [45] is set to eliminate the ultraviolet divergences in finite order cross section calculations.

3.2.2 Parton Distribution Functions

The quantum numbers of a hadron are determined by valance quarks. For example proton has two up quarks (u_v) and one down quark (d_v) and neutron has one up quark (u_v) and two down quarks (d_v). Along with these valance quarks, there are many quarks and anti quarks inside hadrons due to presence of gluons. Deep Inelastic Scattering (DIS) experiments are best to probe the internal structure of nucleons, in which lepton acts as a probe by transferring four momentum $|q|$ to the nucleon in the collision. Electron-proton DIS experiment at SLAC in

1966 was the first evidence for the parton structure inside nucleons.

The resolving power of probe in DIS is $\approx \frac{\hbar}{|q|}$, and the level of structure that can be revealed is increased with $|q|$ i.e. we can get a resolution of 0.002 fm at $|q| = 100 \text{ GeV}$, which is enough to probe the internal structure of proton.

The momentum distribution function of parton within nucleons is simply called Parton Distribution Function (PDF). The PDF gives the probability (normalised to the number of partons) of finding the parton with momentum fraction x at an energy scale $Q^2 = -q^2$. DIS experiments show that at low Q^2 the three valence quarks are more and more dominant. For the high Q^2 values there will be many quark-antiquark pairs with low momentum fraction x . The result of DIS experiments show that, $\approx 50\%$ of nucleon's momentum is carried by quarks and antiquarks and remaining is carried by gluons, momentum fraction carried by gluons is increased with Q^2 . QCD predicts how parton distribution changes with Q^2 energy scale and these predictions are governed by the QCD evolution equation DGLAP in perturbative QCD domain, that is where the value of $\alpha_s(Q^2)$ is much smaller than one. There are different levels of approximations for DGLAP equation, relative to the power of $\alpha_s(Q^2)$ in the perturbative domain, named as Leading-Order (LO), i.e. first order in $\alpha_s(Q^2)$, Next-to-Leading-Order (NLO) and Next-to-Next-to-Leading-Order (NNLO). The Parton Distribution Function (PDF) has an essential role in calculation of cross section. A PDF $f_i(x, \mu_F, \mu_R)$ gives the probability of finding a parton i with a momentum fraction x with factorisation and re-normalisation scale μ_F , and μ_R , where μ_F is also called the probed scale of scattering experiment. The factorisation and re-normalisation [45] scale parameters μ_F and μ_R are used to prohibit infrared and ultraviolet divergences. For the hard scattering processes these scales are of the order of momentum scale i.e. for the Drell-Yan process [46] these scales have typical value which implies $\mu_F = \mu_R = m_Z$. Usually both scales are equal. For the prediction of cross sections these scale are varied simultaneously within $0.5Q < \mu_F, \mu_R < 2.0Q$, where Q is the probe scale of the scattering process.

Perturbative QCD theory cannot predict the actual mathematical form of PDF $f_i(x, \mu_F)$, it gives Q^2 dependence but cannot predict dependence of parton distributions function on x at given Q^2 . Data from Deep inelastic scattering experiments (DIS), are the main source of PDF determination.

For PDFs fit to data, a starting scale is chosen where perturbative QCD predictions can be applied, and we assume many functional forms of the PDFs. Parametrisation of the PDF $f_i(x, \mu_F)$ takes the form

$$f_i(x, \mu_F) = a_0 x^{a_1} (1-x)^{a_2} P(x, a_3, a_4, \dots) \quad (3.2.3)$$

In which P is a polynomial function and a_j is experimentally measured fit value that can not be theoretically predicted. In second step, we choose factorisation scheme, this scheme modeled how heavy quarks are treated, and an order of perturbation theory to be used.

There are several groups who performed PDFs fitting. The results of CTEQ [48], MSTW [47], ABKM [49] and NNPDF [50] collaborations some of which are shown in Fig. 3.3, use all available data for their fits. There are several assumptions and model uncertainties on which PDF approach and fitting is based.

There are different multi purpose event generators, which include all the theoretical aspects of the proton-proton collision. These events generators use different theoretical models which include, shower model for initial and final MPI model [51] and hadronisation and final decay model. Some frequently used generators are PYTHIA [52], HERWIG [53], SHERPA [54] and POWHEG [55]. These generators have all aspects of Standard Model and new physics. The detail of each generator, and what it can do can be found in [20].

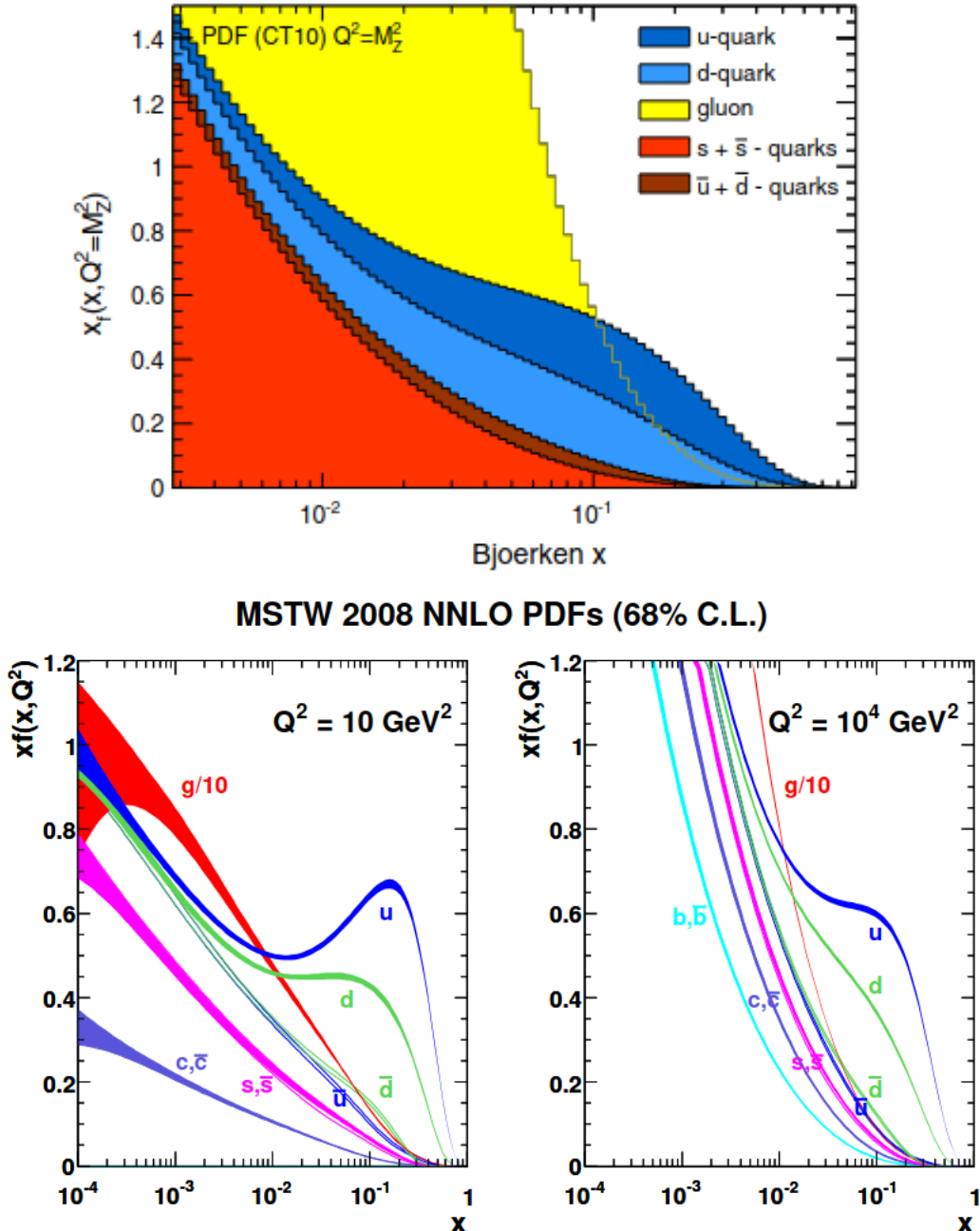


Figure 3.3: Parton Distribution Function evaluated at $Q^2 = m_Z^2$ top [20], MSTW 2008 NNLO PDFs at $Q^2 = 10 \text{ GeV}^2$ and $Q^2 = 10^4 \text{ GeV}^2$ bottom [47]

3.3 Measurement of Cross Section at The LHC

Experimentally, the production cross section is measured by the following equation:

$$\sigma_V^{inc} = \frac{N_{signal}}{\epsilon \cdot BR \cdot \int \mathcal{L} dt} \quad (3.3.1)$$

where $N_{signal} = N_{data} - N_{bkg}$ which is number of signal events, N_{data} is the number of selected events from data and N_{bkg} are the background events. The factor ϵ depends on determination of criteria for the signal selection. To specify the decay channel of W and Z boson branching ratio factor (BR) is used. Integrated luminosity $\int \mathcal{L} dt$, tells about the size of data sample used.

The ϵ is defined as :

$$\epsilon = \frac{N_{reco.}^{selected}}{N_{gen.}^{all}} \quad (3.3.2)$$

$$\epsilon = \frac{N_{reco.}^{selected}}{N_{gen.}^{selected}} \cdot \frac{N_{gen.}^{selected}}{N_{gen.}^{all}} \quad (3.3.3)$$

$$\epsilon = C.A \quad (3.3.4)$$

where $N_{reco.}^{selected}$ are events selected at the reconstruction level and $N_{gen.}^{all}$ is the number of all generated events. A represents fiducial acceptance factor and C is for detector-induced correction factor. Ratio of the number of selected events at generator level ($N_{gen.}^{selected}$) to the total number of generated events ($N_{gen.}^{all}$) is called fiducial acceptance. The main source of uncertainties in the fiducial acceptance are scale and PDF uncertainties.

The detector correction factor C is ratio of ($N_{reco.}^{selected}$) from data sample to the number of selected events ($N_{gen.}^{selected}$) from Monte Carlo. The dominant uncertainties in the detector correction factor are experimental sources. The fiducial cross-section, defined as:

$$\sigma_V^{fid} = \frac{N_{data} - N_{bkg}}{C.BR. \int \mathcal{L} dt} = \sigma_V^{inc}.A \quad (3.3.5)$$

3.4 Event Selection for Vector Bosons

3.4.0.1 ATLAS

Events for Z boson, i.e., $Z \rightarrow l^+l^-$ required Di lepton invariant mass of $66 \text{ GeV} < m_{ll} < 116 \text{ GeV}$. Muons must be in $|\eta| < 2.4$ with $p_T(\text{min.}) > 20 \text{ GeV}$. Electrons are required to fulfill $1.52 < |\eta| < 2.4$ with $E_T(\text{min.}) > 20 \text{ GeV}$.

W boson decays to an energetic lepton and corresponding neutrino, neutrinos cannot be detected hence leads to missing transverse energy. Thus the mass of W boson cannot be reconstructed due to this missing energy. The invariant mass projection to the transverse plane, defined as

$$m_T = \sqrt{2.p_T^l.p_T^\nu.(1 - \cos(\phi^l - \phi^\nu))} \quad (3.4.1)$$

can be reconstructed, where p_T^l is lepton transverse momentum and p_T^ν is neutrino transverse momentum, ϕ^l and ϕ^ν are azimuthal angles for lepton and neutrino respectively. For the W boson events selection at ATLAS required one reconstructed, single lepton with $E_T^{\text{miss.}}$ of 25 GeV and $m_T(\text{min.}) > 50 \text{ GeV}$. Selection for the Z boson by ATLAS is shown in Fig. 3.4

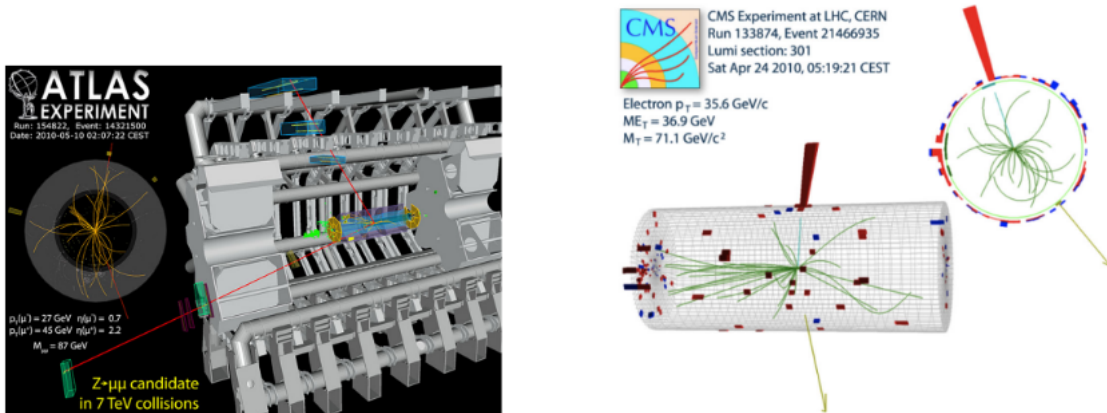


Figure 3.4: $Z \rightarrow \mu\mu$ in ATLAS detector (left) and $W \rightarrow e\nu$ in CMS detector (right) [20].

3.4.0.2 CMS

For $Z \rightarrow \mu\mu$, oppositely charged muons are required for $|\eta| < 2.1$ and transverse momentum requirement of $p_T > 20\text{GeV}$. For the electron decay channel $Z \rightarrow ee$, $|\eta| < 1.44$ and $E_T > 20\text{GeV}$ are required.

The selection criterion for W boson events, required single electron with $E_T > 25\text{ GeV}$ and $|\eta| < 2.5$ or single muon with $p_T > 25\text{ GeV}$ and $|\eta| < 2.1$. A typical $W \rightarrow e\nu$ event in the CMS detector is shown in Fig. 3.4. Tables 3.1 and 3.2 show the kinematic cuts used by CMS and ATLAS.

Table 3.1: Kinematic cuts for CMS analysis [56] at 7 TeV for leptonic channel of Z and W boson respectively.

CMS		
Electron-channel	$Z \rightarrow l^+l^-$	$W \rightarrow l^\pm\nu$
	$E_T(e^+) > 25\text{GeV}$	one e^\pm with $E_T > 25\text{GeV}$
	$E_T(e^-) > 25\text{GeV}$	$ \eta_{e^\pm} < 1.44$
	$ \eta_{e^\pm} < 1.44$	
	$60\text{ GeV} < m_{ee} < 120\text{ GeV}$	
Muon-channel		
	$p_T(\mu^+) > 25\text{GeV}$	one e^\pm with $p_T > 25\text{GeV}$
	$p_T(\mu^-) > 25\text{GeV}$	$ \eta_{\mu^\pm} < 2.1$
	$ \eta_{\mu^\pm} < 2.1$	
	$60\text{ GeV} < m_{\mu\mu} < 120\text{ GeV}$	

Table 3.2: Kinematic cuts for ATLAS analysis [57] at 13 TeV for the leptonic channel of Z and W boson respectively.

ATLAS		
Electron-channel	$Z \rightarrow l^+l^-$	$W \rightarrow l^\pm\nu$
	$E_T(e^+) > 25\text{GeV}$	$p_T^{(e^\pm)} > 25\text{GeV}$
	$E_T(e^-) > 25\text{GeV}$	$p_T^{(\nu)} > 25\text{GeV}$
	$ \eta_{e^\pm} < 1.37$	$ \eta_{e^\pm} < 1.52$
	$66\text{ GeV} < m_{ee} < 116\text{ GeV}$	$m_T > 50\text{GeV}$
Muon-channel		
	$p_T(\mu^+) > 25\text{GeV}$	$p_T^{(\mu^\pm)} > 25\text{GeV}$
	$p_T(\mu^-) > 25\text{GeV}$	$p_T^{(\nu)} > 25\text{GeV}$
	$ \eta_{\mu^\pm} < 2.4$	$ \eta_{\mu^\pm} < 2.4$
	$66\text{ GeV} < m_{\mu\mu} < 116\text{ GeV}$	$m_T > 50\text{GeV}$

The transverse mass distribution for electron and lepton channel of W boson event and dilepton mass distribution for the Z boson event can be seen in Fig. 3.5.

3.5 Inclusive Cross Section of W and Z Bosons

For the DrellYan processes [46] as shown in Fig. 3.6, the theoretical prediction at NNLO are known in term of α_s (strong coupling constant) for the inclusive production cross section of the Z and W vector boson.

Z bosons are produced by the quarks-antiquark annihilation, i.e. $u\bar{u}$, $d\bar{d}$ and also $s\bar{s}$. W^\pm

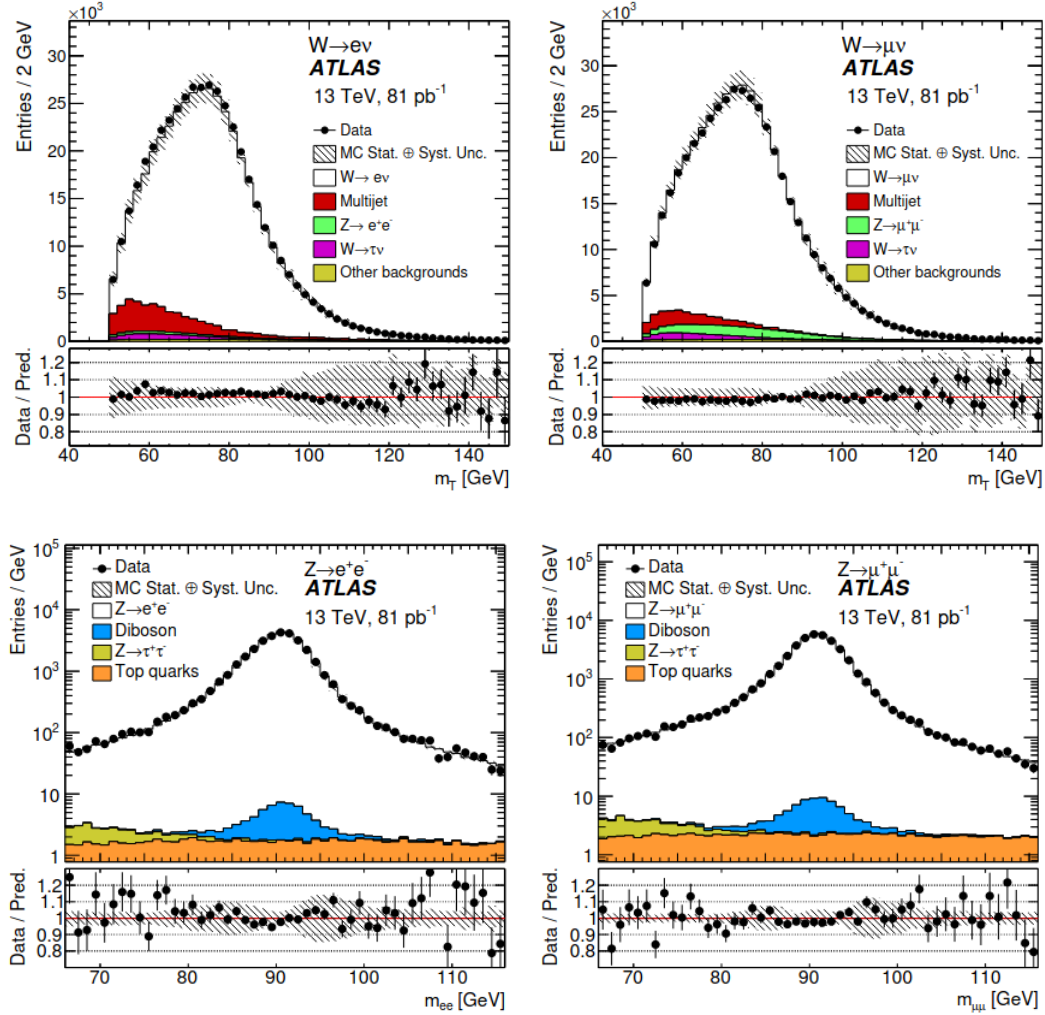


Figure 3.5: Transverse mass m_T distributions of $W \rightarrow e\nu$ and $W \rightarrow \mu\nu$ process (top) and dilepton mass m_{ll} distribution (bottom) [57]

boson production is different from Z boson because it depends on the charge of W , W^+ boson is produced in $u\bar{d} \rightarrow W^+$ process and W^- in $d\bar{u} \rightarrow W^-$ process. W^+ is produced from the annihilation of u -valence quarks and \bar{d} -sea quark, W^- from d -valence quark and \bar{u} quark. Since there are two u - quarks (valence) and one d - quark (valence) available in the proton, therefore more W^+ bosons are expected than W^- bosons. Thus QCD predictions can be tested precisely from the ratio of W^+ and W^- production as cross section ratios cancel many of the theoretical and experimental uncertainties.

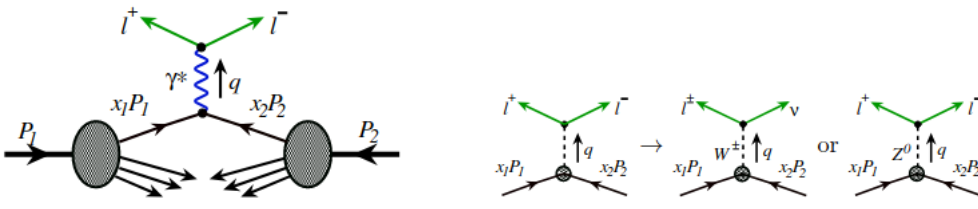


Figure 3.6: Graphical sketch for the generalized partonic hard part of the Drell-Yan process [46]

Integrated luminosity is one of the main source of experimental uncertainties. In cross-section ratio measurement, this uncertainty is reduced, along with some other experimental and theoretical uncertainties. Therefore along with cross-section of W and Z boson, cross section ratios $\frac{\sigma(W^+ + \sigma(W^-))}{\sigma(Z)}$ and $\frac{\sigma(W^+)}{\sigma(W^-)}$, have unique importance.

The cross-section ratio for $\sigma(W^+ + W^-)/\sigma(Z)$ represents the cross section dependence on the quarks-distribution functions.

$$\sigma(W^+ + \sigma(W^-)) = u_v(x) + \bar{d}_v(x) + d_v(x) + \bar{u}_s(x) \quad (3.5.1)$$

$$\sigma(Z) = (g_V(u)^2 + g_A(u)^2 \cdot u_q(x)) + (g_V(d)^2 + g_A(d)^2 \cdot v_q(x)) \quad (3.5.2)$$

with

$$u_q(x) = (u_v(x) + \bar{u}_s(x)) \quad (3.5.3)$$

$$v_q(x) = (d_v(x) + \bar{d}_s(x)) \quad (3.5.4)$$

where $u_v(x)$ and $\bar{u}_s(x)$ are valance quark distributions and $u_s(x)$ and $d_s(x)$ are the respective sea-quark distributions. If we assume that light sea quark and anti-quark have same distribution, then the PDF dependence will be reduced, i.e, $\bar{q}(x) = q(x)$ for $q = u, d, s\dots$. Thus the ratio of W to Z boson helps us to constrain the strange quark distribution [58].

The above statement doesn't hold for cross-section ratios, such as ratio of W^+ to W^- , W^+ or W^- to Z boson. These cross section ratios have a large dependence on difference in the $u-$ and $d-$ quark distribution functions, and is very sensitive to this difference in valance-quark distributions. However, for the PDFs constraints, along with inclusive cross section the differential cross section measurements are also very important.

3.5.1 Differential Production Cross Section of W and Z Boson:

The differential cross section also measured at LHC with great precision, and differential cross section of vector bosons plotted versus their rapidity distribution, provides extra constraint on the PDFs.

Rapidity distribution for the process $Z \rightarrow l^+l^-$, can be directly measured from detector data, because four-momenta of the decaying leptons can be precisely measured and thus rapidity can be measured precisely. This will help us to constrain the PDFs of $u\bar{u}$, $d\bar{d}$, and $s\bar{s}$. The differential cross section measurement helps us to improve strange-quark PDFs. Fig. 3.8 shows different quark/antiquark annihilation processes for different rapidity (y_Z) values. The rapidity distribution of Z boson from the annihilation of $u\bar{u}$, $d\bar{d}$ and $s\bar{s}$ processes gives additional constraints on PDFs, as well as the rapidity distribution in the central region for $s\bar{s}$ process, is important to determine its PDFs. ATLAS and CMS both, published differential cross section $\frac{d\sigma}{dy_Z}$ for different integrated luminosities $\int \mathcal{L} dt$ in the fiducial region defined by kinematic cuts earlier.

The W boson decays into lepton and corresponding neutrino, i.e., $W^\pm \rightarrow l^\pm \nu$. The direct measurement of rapidity distribution of W^\pm boson is not possible, because the p_z of decayed neutrino can't be reconstructed, thus pseudo rapidity of the decay lepton η_l is measured and correlated to y_W by an indirect method. The rapidity distribution of W^\pm boson is sensitive to the $u\bar{d}$ and $d\bar{u}$ quark distribution as shown in Fig. 3.8. The y_Z measurement helps us to constrain the PDFs of strange quark.

Differential cross-section measurements of the W and Z bosons provide important constraints

for the PDFs. Fig. 3.7 shows the difference in PDFs of \bar{u} and \bar{s} quarks with and without LHC data based on the NNPDF group.

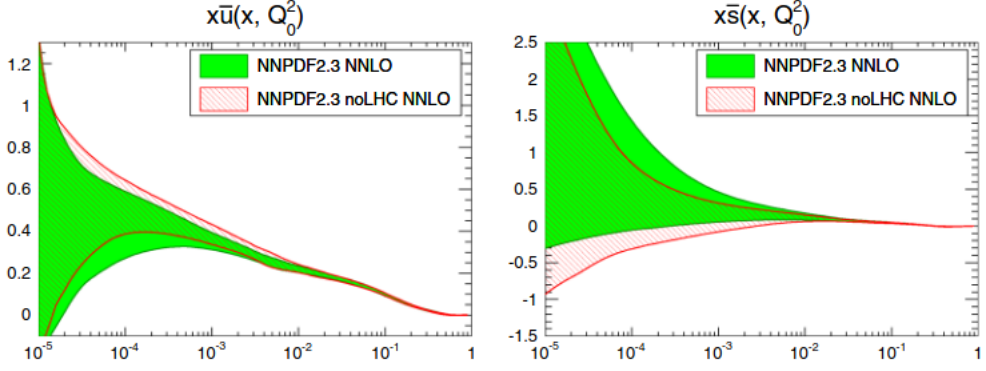


Figure 3.7: Comparison of PDFs of \bar{u} and \bar{s} quarks with LHC and without LHC data. [20]. Comparison plots can also be found in [59].

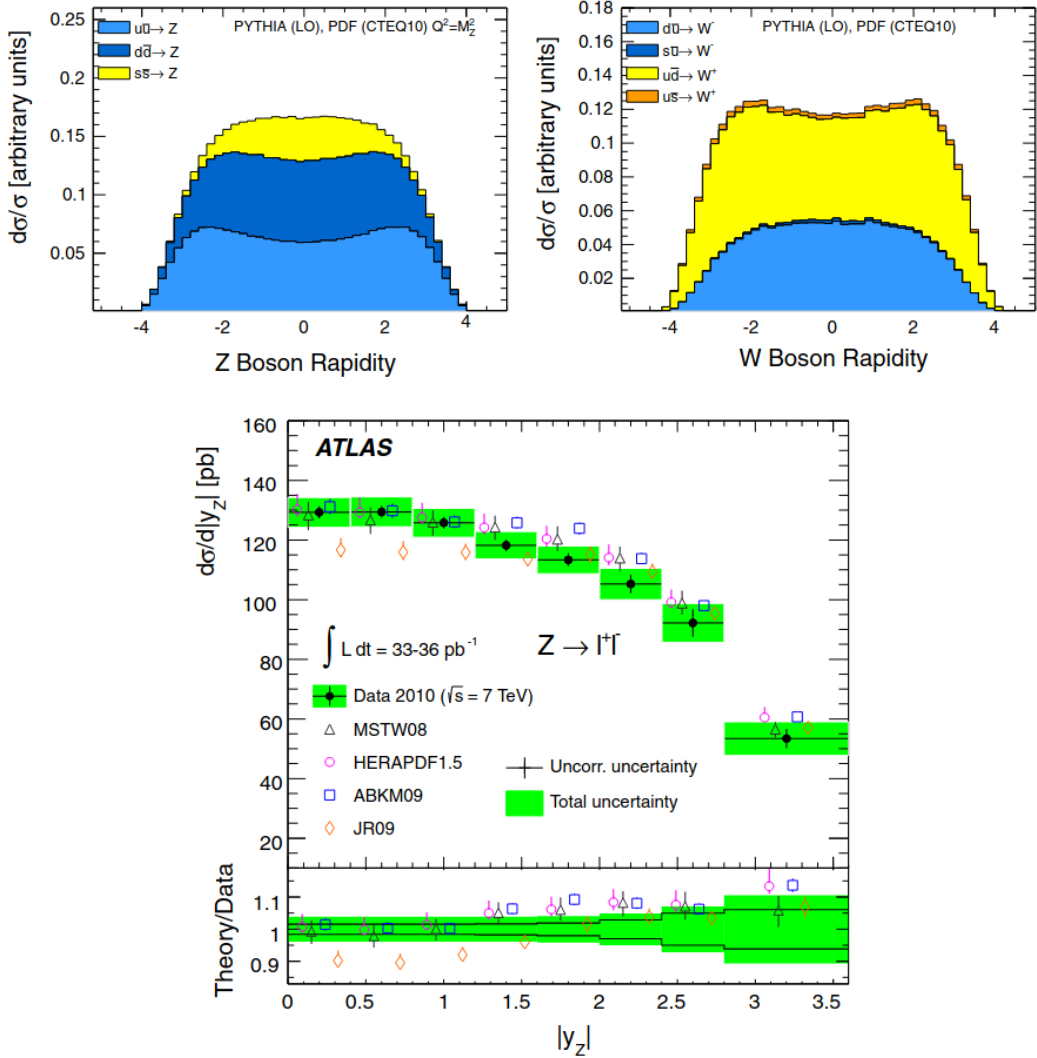


Figure 3.8: Z boson rapidity distribution (*left*) and W boson rapidity distribution (*right*) in 7 TeV pp collisions(*top*), for $Z \rightarrow l^+l^-$ the combined $d\sigma/d|y_Z|$ cross-section measurement compared to NNLO theoretical predictions (*bottom*) [20]

3.6 Measurement of p_T of Vector Bosons

The W boson mass at LHC can be measured by the accurate measurement and understanding of transverse momentum p_T , the p_T distribution of product leptons of $W^\pm \rightarrow l^\pm \nu$ is an important parameter for m_W .

The p_T distribution of electron and muon channel for the $Z \rightarrow l^+l^-$ process can be computed directly from four momentum information of resulting leptons.

The $p_T(Z)$ distribution is an important tool for the Monte-Carlo (MC) generators, and transverse momentum of Z boson helps to measure the $p_T(W)$, of which direct measurement is not possible. The transverse momentum of W boson cannot be measured directly from the decayed leptons because we don't know about neutrino momentum. However, the $p_T(W)$ is measured by the p_T (*hadron*) from which it was produced. The $p_T(W)$ is balanced by the hadronic transverse momentum p_T (*hadron*), i.e.

$$p_T(W) = -p_T(\text{had}) = p_T(l^\pm + p_T(\nu)), \quad (3.6.1)$$

where $p_T(\text{had})$ is the recoil of hadron (Fig. 3.9), hence $p_t(W)$ can be measured from hadronic

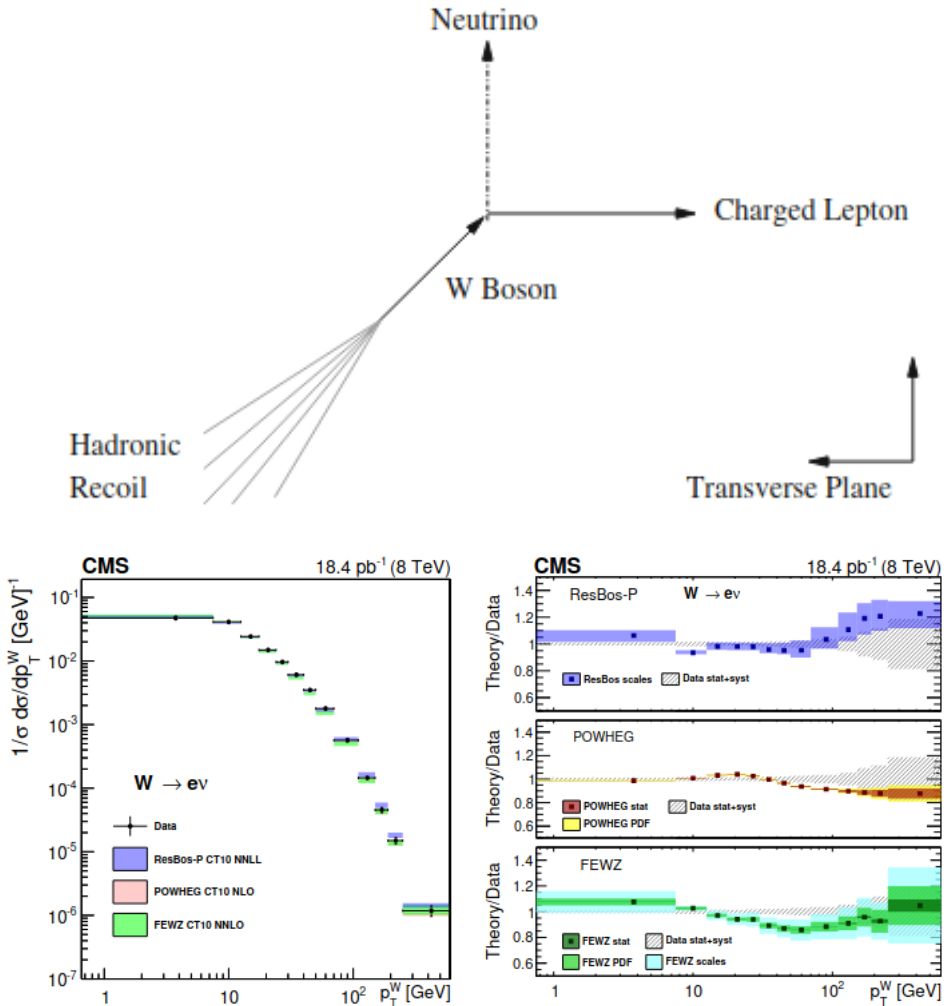


Figure 3.9: Hadronic recoil illustration in $W^\pm \rightarrow l^\pm \nu$ events (*top*). Differential cross sections (Normalized) for W boson as a function of $p_T(W)$ for electron. Ratios of theoretical predictions to the data (*bottom*) [35].

transverse momentum $p_t(\text{hadron})$, which is due to hadronic activities in QCD interactions of

hadrons. Due to several experimental uncertainties in the hadronic recoil, a theoretical model is used to define the relation between $p_T(\text{had})$ and $p_T(W)$. Data of Z boson events helps to model this theoretical model. We consider that the hadronic recoil p_T (*hadron*) is same for the W and Z bosons, and with different approach we can find p_T (W).

3.7 Measured Cross Section of W and Z Bosons at Different C.O.M Energy

The production cross section of W and Z vector bosons is measured at LHC in ATLAS and CMS experiments at different center-of-mass energies, i.e., 7 TeV , 8 TeV and 13 TeV with certain uncertainties ($\pm \text{stat.} \pm \text{syst.} \pm \text{lumi.}$). The measured value of cross section increased with the increase in center-of-mass energy as shown in Fig. 3.10. The production cross-section

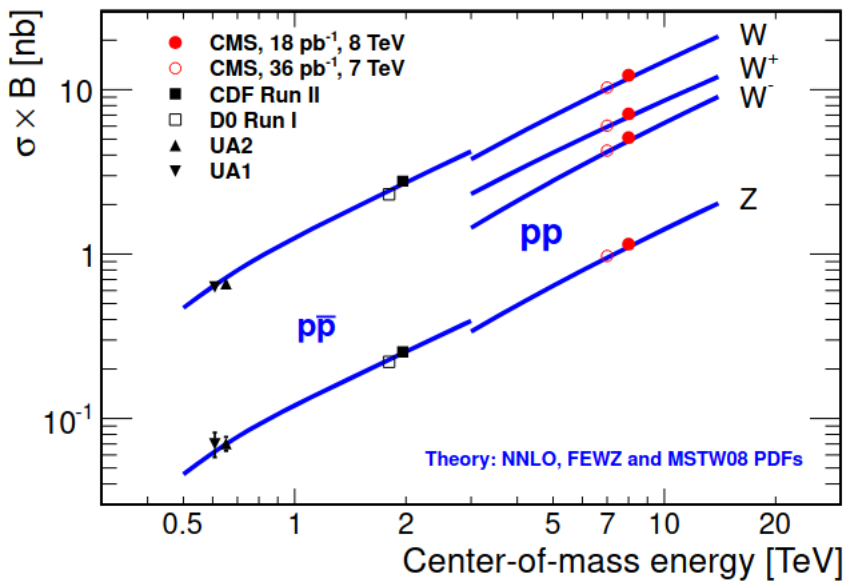


Figure 3.10: The predicted increase in cross section of vector bosons [60].

of W and Z boson, measured ($\sigma \times BR(W \rightarrow l\nu, Z \rightarrow ll)$) and predicted at various c.o.m energies is listed in the following Tables 3.3, 3.4, 3.5, 3.6, 3.7 and 3.8.

Table 3.3: Measured and NNLO predicted Ratios of W^+/W^- and W^\pm/Z . The measured values are at 7 TeV with an integrated luminosity of 36 pb^{-1} at CMS [56].

Channel	Measured Ratio	Predicted Ratio (NNLO) (value \pm PDF)
W^+/W^-	$1.418 \pm 0.008 \pm 0.02$	1.43 ± 0.001
W^\pm/Z	$10.56 \pm 0.12 \pm 0.12$	10.47 ± 0.04

Table 3.4: The measured total σ^{tot} cross section for leptonic channel of W^- , W^+ , W^\pm and Z -boson, and predicted total cross section. The measured values with certain uncertainties ($\pm stat.$, $\pm syst.$, $\pm lumi.$) are at 7 TeV with integrated luminosity 36 pb^{-1} at CMS and the predictions are at NNLO [56].

channel	Measured Cross section [nb]	Predicted Cross Section (NNLO) [nb] (value \pm PDF)
W^-	$4.34 \pm 0.02 \pm 0.11 \pm 0.25$	4.29 ± 0.11
W^+	$6.115 \pm 0.02 \pm 0.07 \pm 0.24$	6.15 ± 0.17
W^\pm	$10.48 \pm 0.03 \pm 0.16 \pm 0.43$	10.44 ± 0.27
Z	$0.99 \pm 0.011 \pm 0.02 \pm 0.03$	0.97 ± 0.03

Table 3.5: The measured total σ^{tot} cross sections with uncertainties ($\pm stat.$, $\pm syst.$, $\pm lumi.$) for lepton channels of W^- , W^+ , W^\pm and Z -boson, and predicted total cross section. The measured values are at 8 TeV with integrated luminosity 18.2 pb^{-1} at CMS and predictions are at NNLO [60].

channel	Measured Cross section [nb]	Predicted Cross section [nb] (value \pm PDF)
W^-	$5.09 \pm 0.02 \pm 0.11 \pm 0.18$	5.06 ± 0.13
W^+	$7.11 \pm 0.03 \pm 0.14 \pm 0.13$	7.12 ± 0.20
W^\pm	$12.21 \pm 0.02 \pm 0.55 \pm 0.43$	12.18 ± 0.32
Z	$1.15 \pm 0.01 \pm 0.02 \pm 0.03$	1.13 ± 0.04

Table 3.6: Measured and predicted Ratios W^+/W^- and W^\pm/Z . The measured values are at 8 TeV with integrated luminosity 18.2 pb^{-1} at CMS and predictions are at NNLO [60].

Channel	Measured Ratio (Value \pm stat. \pm syst.)	Predicted Ratio(NNLO) (value \pm PDF)
W^+/W^-	$1.395 \pm 0.01 \pm 0.020$	1.418 ± 0.02
W^\pm/Z	$10.63 \pm 0.11 \pm 0.25$	10.47 ± 0.04

Table 3.7: The measured total σ^{tot} cross sections for the lepton channel of W^- , W^+ , W^\pm , and Z -boson, and predicted total cross section. The measured values are at 13 TeV with integrated luminosity 43 pb^{-1} at CMS [61].

channel	Measured Cross section[nb]	Predicted Cross section [nb] (NNLO) (value \pm PDF \pm scale \pm other)
W^-	$8.68 \pm 0.08 \pm 0.25 \pm 0.42$	$8.37_{-0.21}^{+0.24} \pm 0.11 \pm 0.12$
W^+	$11.39 \pm 0.09 \pm 0.34 \pm 0.55$	$11.33_{-0.27}^{+0.24} \pm 0.15 \pm 0.16$
W^\pm	$20.07 \pm 0.12 \pm 0.57 \pm 0.96$	$19.7_{-0.47}^{+0.56} \pm 0.26 \pm 0.28$
Z	$1.92 \pm 0.02 \pm 0.06 \pm 0.09$	$1.87 \pm 0.05 \pm 0.03 \pm 0.03$

Table 3.8: Measured and predicted Ratios W^+/W^- and W^\pm/Z . The measured values are at 13 TeV with integrated luminosity 43 pb^{-1} [61].

Channel	Measured Ratio (Value \pm stat \pm syst)	Predicted Ratio(NNLO) (value \pm PDF)
W^+/W^-	$1.31 \pm 0.02 \pm 0.03$	1.35 ± 0.01
W^\pm/Z	$10.46 \pm 0.06 \pm 0.16$	10.55 ± 0.07

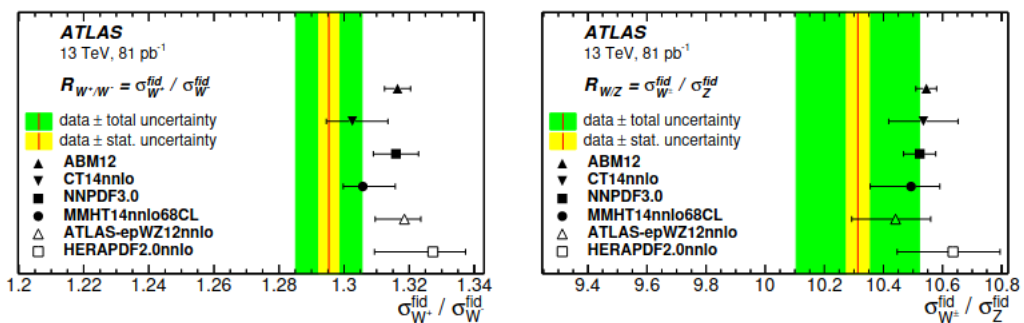
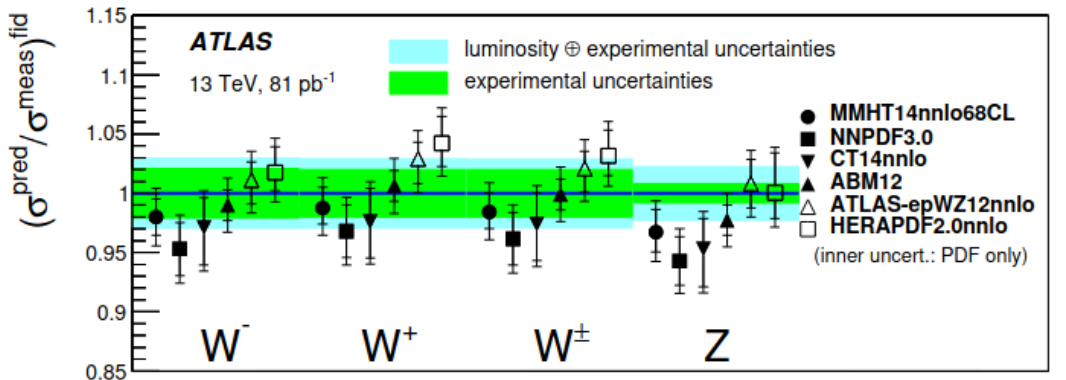


Figure 3.11: Ratio of Measured to predicted cross section(*top*), comparison of measured and predicted cross section ratio of W and Z boson (*bottom*). [57]

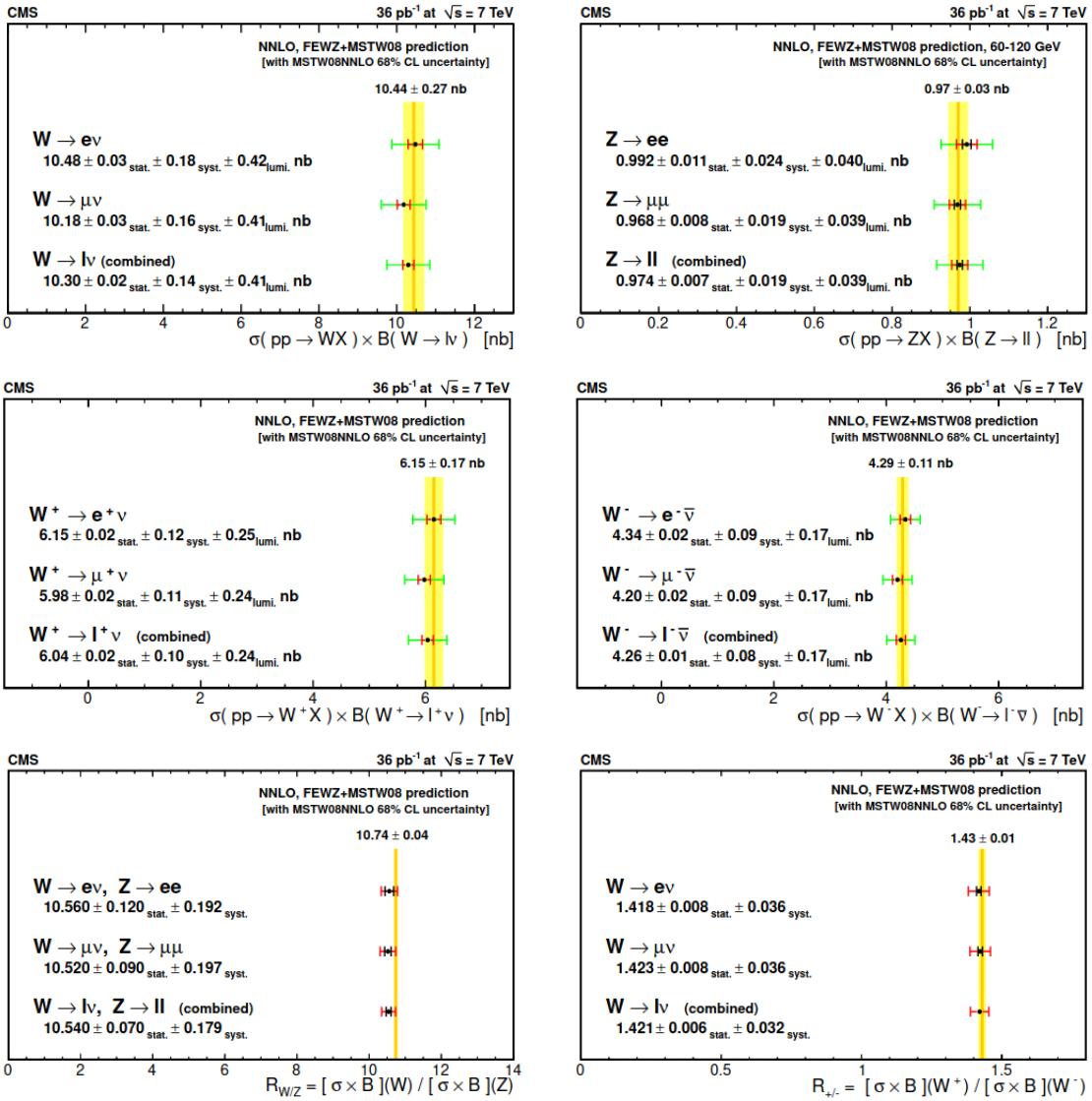


Figure 3.12: Measurements of vector boson cross section production multiplied with leptonic branching ratio (*top*). Measurements of W^+ and W^- production cross section times branching ratio (*middle*). Ratio of W^+ to Z and W^+ to W^- *bottom*. The yellow line showing the measured value with various experimental uncertainties at 7 TeV , 36 pb^{-1} [56]

Fig. 3.11 shows the ratio of the experimentally measured and theoretically predicted cross section for the leptonic channel (e and μ) using various PDFs and also ratio of production cross section of charged W boson and W^\pm boson to Z boson compared to theoretical predictions with different PDF sets.

Fig. 3.12 shows the summary of the measurement in the electron and muon channels by CMS at 7 TeV , and results are compared with the theoretical predictions.

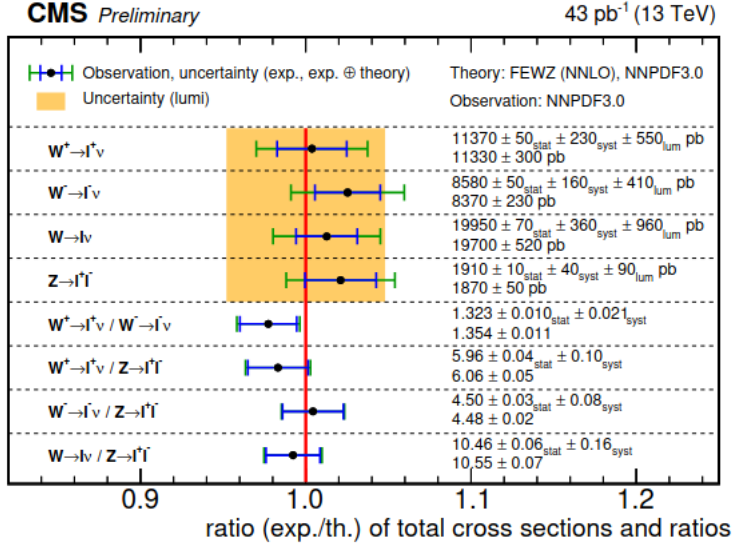


Figure 3.13: The CMS measured total cross sections of W , W^+ , W^- and Z boson times branching fraction and theoretically predicted cross section. In each column upper value represent measured cross section with uncertainties and lower value represent theoretically predicted cross section, and their ratio also. [61]

Figs. 3.13, 3.14 and 3.15 shows the comparision of measurements at CMS with predictions by NNPDF3.0 (NNLO) at 13 TeV .

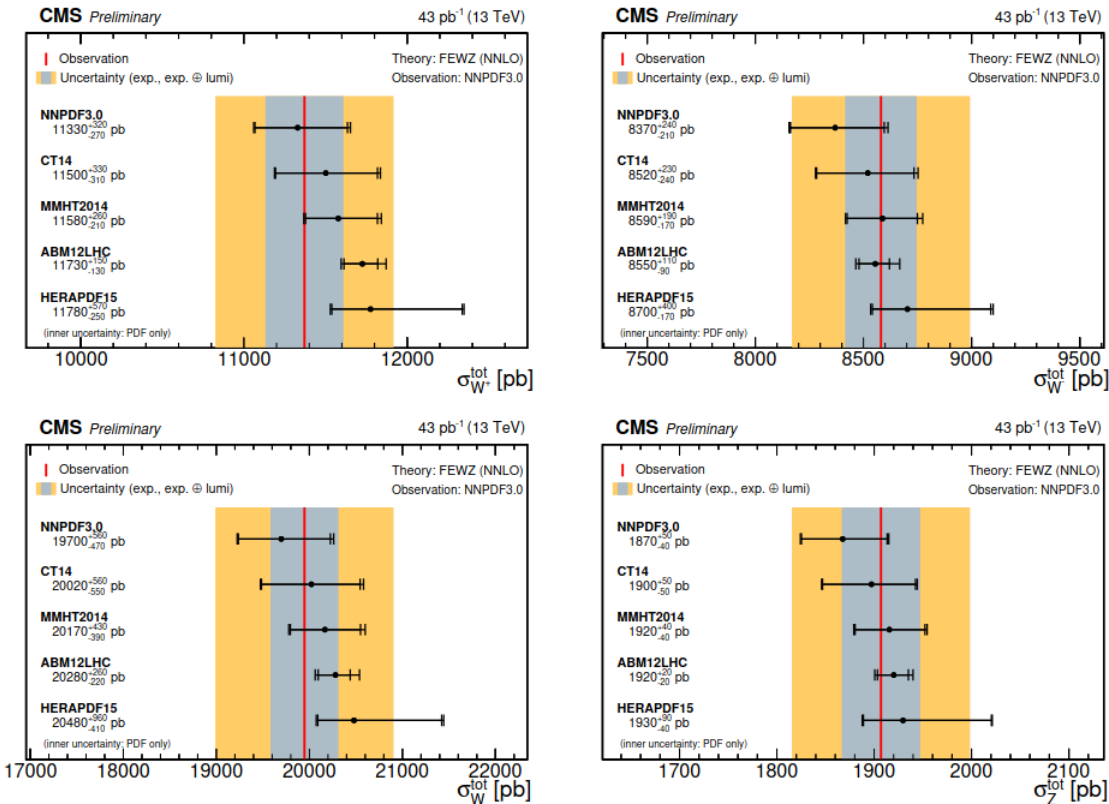


Figure 3.14: Measured cross section (red line) and predicted cross section with different PDFs. The data points with error bars represent theoretically predicted value with various uncertainties [61]

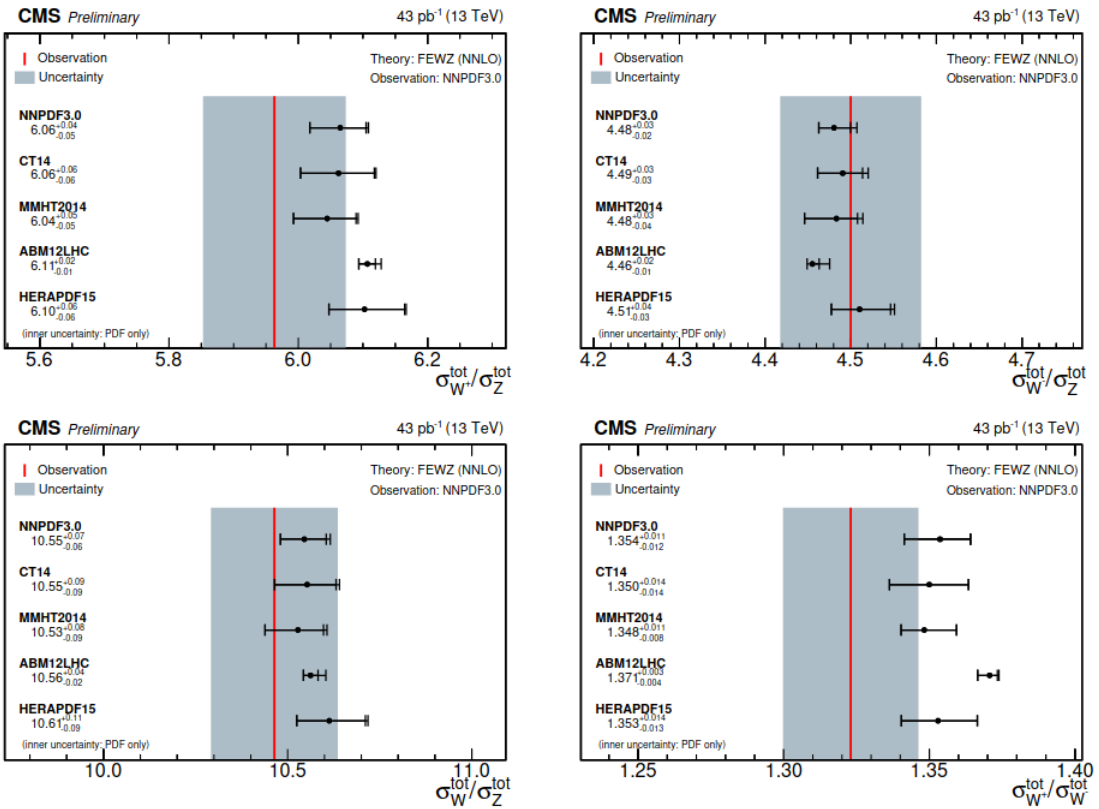


Figure 3.15: Measured total cross section ratios of vector bosons and predicted cross section ratios of vector boson with different PDFs set [61].

3.8 Uncertainties in the Predictions

Imperfect knowledge of the proton parton distribution functions is the main source of uncertainties in predictions. The PDFs uncertainties can be evaluated from sum in quadrature by the difference of central PDF and Eigenvectors or error vectors of respective PDF set. The uncertainties determination depends upon the given PDF set, for Monte Carlo set (NNPDF) uncertainties are determined differently from Hessian PDF set and same for all other sets.

3.8.1 Computation of Hessian PDF uncertainties

In hessian matrix approach the experimental uncertainties are propagated by diagonalising the $n \times n$ hessian matrix, more details can be found in [62].

Hessian: Consider a variable Y ; the central value for Y using central PDF is given by Y_0 . Y_i^+ and Y_i^- is the value of that variable corresponding to positive and negative direction of the error vector i respectively [62].

$$\Delta Y_{\max}^+ = \sqrt{\sum_{i=1}^N [\max(Y_i^+ - Y_0, Y_i^- - Y_0, 0)]^2} \quad (3.8.1)$$

$$\Delta Y_{\max}^- = \sqrt{\sum_{i=1}^N [\max(Y_0 - Y_i^+, Y_0 - Y_i^-, 0)]^2} \quad (3.8.2)$$

ΔY^+ is the PDF error which indicates increase in the observable Y , and ΔY^- the PDF error indicates decrease in the observable Y . The sum is over all N eigenvector directions.

Symmetric Hessian: For the simple symmetric case where only the value of variable using

central PDF Y_0 and N error vector using PDF Y_i , ($i = 1, \dots, N$) are provided, the central value and PDF uncertainties are calculated as:

$$\Delta Y^+ = \Delta Y^- = \Delta Y = \sqrt{\sum_{i=1}^N (Y_i - Y_0)^2} \quad (3.8.3)$$

3.8.2 Computation of Monte Carlo PDF uncertainties

For the NNPDF Monte Carlo set, a PDFs set with replicas is given. The average value for any observable X (for example cross section) which depends on the PDFs sets is computed from usual formula:

$$\langle X(q) \rangle = \frac{1}{N_{rep}} \sum_{i=1}^{N_{rep}} X(q^i) \quad (3.8.4)$$

where N_{rep} is the number of replicas in the Monte Carlo PDF set. The associated uncertainty in the observable is found, according to the usual formula:

$$\sigma_X = \left[\frac{N_{rep}}{N_{rep} - 1} (\langle X(q)^2 \rangle - \langle X(q) \rangle^2) \right]^{1/2} \quad (3.8.5)$$

$$\sigma_X = \left[\frac{1}{N_{rep} - 1} \sum_{i=1}^{N_{rep}} (X(q^i) - \langle X(q) \rangle)^2 \right]^{1/2} \quad (3.8.6)$$

NNPDF group provide both $N_{rep} = 100$ and $N_{rep} = 1000$ replicas set. Equation 3.8.5 provides the 1sigma PDF uncertainty on a general quantity which depends on PDFs.

Different PDFs groups provide both 68% and 90% confidence-level(C.L.) uncertainties. Some PDFs groups provide sets for both the 68% confidence-level (C.L.) and 90% C.L. Uncertainties. These uncertainties can be co-related by a factor of 1.64485. In general we can evaluate PDFs uncertainties for both confidence level 68% and 90% i.e. NNPDF3.1 [63].

3.8.3 Theoretical Uncertainties

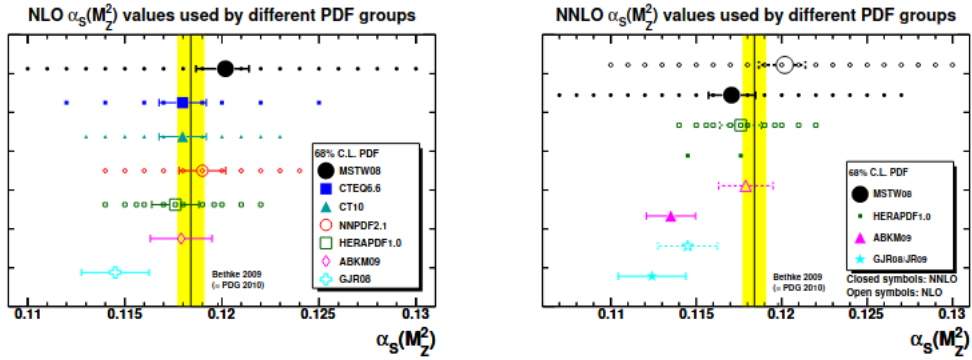
The determination of theoretical uncertainties improves the PDFs relation to measurable quantities. The study of experimental uncertainties is much advanced than theoretical uncertainties, and only some of the theoretical uncertainties are explored in detail.

The determination of strong interactions between the quarks is the first source of theoretical uncertainty. The QCD parameters including the value of the strong coupling constant α_s and the heavy quark masses m_c (*charmquarks*) and m_b (*bottomquark*), and variation of re-normalisation μ_R and factorisation μ_F scales are the source of theoretical uncertainties.

Of these uncertainties, the uncertainty due to choice of strong coupling constant value α_s is explored in detail by each PDF group. The uncertainty due to choice of heavy quark masses (charm and bottom) is also explored by some PDF groups e.g. NNPDF3.1, Cteq18, HERA etc. The uncertainties due to variation in factorisation and re-normalisation scales are explored by NNPDF3.1.

3.8.3.1 The value of α_s ant its uncertainty

The theoretical uncertainty due to the choice of strong coupling constant α_s value is studied and explored by each PDFs group. Different PDFs groups used different value of α_s as shown in Fig. 3.16. The choice of α_s has clear importance for the PDFs prediction, especially for the gluons distribution.


 Figure 3.16: The value of α_s used by different PDF groups

The values of $\alpha_s(m_Z^2)$ and its uncertainties used by different PDFs group are summarized in Fig. 3.16. The world average value of $\alpha_s(m_Z^2)$ is $\alpha_s = 0.1184 \pm 0.0007$ [47].

The uncertainty on the value of α_s , $\Delta\alpha_s = \pm 0.001$ at 68% C.L. and $\Delta\alpha_s = \pm 0.002$ at 90% C.L. has been used for the CTEQ, NNPDF studies. The predictions in the value of cross section changes with the choice of α_s value used.

Various theoretical uncertainties for the 7 TeV are shown in Fig. 3.17.

LHC, $\sqrt{s} = 7$ TeV	$B_{\ell\nu} \cdot \sigma_{W^\pm}$	$B_{\ell\nu} \cdot \sigma_{W^\pm}$	$B_{\ell\nu} \cdot \sigma_{Z^0}$	$B_{\ell+\ell-} \cdot \sigma_{Z^0}$	R_{WZ}	R_{WZ}
Uncertainties (%)	68%	90%	68%	90%	68%	90%
PDF only	+1.7 -1.6 +2.6 -1.9	+3.4 -3.1 +4.6 -3.9	+1.7 -1.6 +2.5 -1.8	+3.4 -3.1 +4.4 -3.9	+0.2 -0.1 +0.3 -0.2	+0.4 -0.3 +0.5 -0.4
PDF+ α_S	+1.1 -1.2 +0.1 -0.1 +2.8 -2.2	+1.8 -2.1 +0.2 -0.3 +4.9 -4.5	+1.4 -1.5 +0.0 -0.0 +2.9 -2.3	+2.3 -2.4 +0.0 -0.0 +5.0 -4.6	+0.2 -0.3 +0.1 -0.1 +0.4 -0.3	+0.4 -0.5 +0.2 -0.2 +0.7 -0.7
Charm mass, m_c	+1.1 -1.2 +0.1 -0.1 +2.8 -2.2	+1.8 -2.1 +0.2 -0.3 +4.9 -4.5	+1.4 -1.5 +0.0 -0.0 +2.9 -2.3	+2.3 -2.4 +0.0 -0.0 +5.0 -4.6	+0.2 -0.3 +0.1 -0.1 +0.4 -0.3	+0.4 -0.5 +0.2 -0.2 +0.7 -0.7
Bottom mass, m_b	+0.5 -0.8 +2.8 -2.4	+0.9 -1.3 +5.0 -4.6	+0.5 -0.7 +2.9 -2.4	+0.5 -1.1 +5.0 -4.7	+0.8 -1.1 +5.0 -4.6	+0.1 -0.1 +0.4 -0.4
PDF+ $\alpha_S+m_{c,b}$	+0.5 -0.8 +2.8 -2.4	+0.9 -1.3 +5.0 -4.6	+0.5 -0.7 +2.9 -2.4	+0.5 -1.1 +5.0 -4.7	+0.8 -1.1 +5.0 -4.6	+0.1 -0.1 +0.4 -0.4
Scales (μ_R, μ_F)	+0.5 -0.8 +2.8 -2.4	+0.9 -1.3 +5.0 -4.6	+0.5 -0.7 +2.9 -2.4	+0.5 -1.1 +5.0 -4.7	+0.8 -1.1 +5.0 -4.6	+0.1 -0.1 +0.4 -0.4
PDF+ $\alpha_S+m_{c,b}+\mu_{R,F}$	+0.5 -0.8 +2.8 -2.4	+0.9 -1.3 +5.0 -4.6	+0.6 -0.8 +2.7 -2.3	+1.0 -1.3 +4.8 -4.8	+1.0 -1.3 +4.8 -4.8	+0.1 -0.1 +1.1 -0.8

LHC, $\sqrt{s} = 7$ TeV	$B_{\ell\nu} \cdot \sigma_{W^+}$	$B_{\ell\nu} \cdot \sigma_{W^-}$	R_\pm			
Uncertainties (%)	68%	90%	68%	90%	68%	90%
PDF only	+1.8 -1.6 +2.6 -1.9	+3.6 -3.2 +4.9 -4.0	+1.7 -1.7 +2.5 -1.9	+3.5 -3.3 +4.4 -4.2	+1.0 -0.7 +1.1 -0.7	+2.2 -1.5 +2.3 -1.5
PDF+ α_S	+1.2 -1.3 +0.1 -0.1 +2.9 -2.3	+1.9 -2.2 +0.2 -0.2 +5.2 -4.6	+1.0 -1.1 +0.1 -0.1 +2.7 -2.2	+1.5 -1.8 +0.2 -0.3 +4.7 -4.6	+0.2 -0.2 +0.0 -0.0 +1.1 -0.8	+0.4 -0.4 +0.0 -0.0 +2.4 -1.5
Charm mass, m_c	+1.2 -1.3 +0.1 -0.1 +2.9 -2.3	+1.9 -2.2 +0.2 -0.2 +5.2 -4.6	+1.0 -1.1 +0.1 -0.1 +2.7 -2.2	+1.5 -1.8 +0.2 -0.3 +4.7 -4.6	+0.2 -0.2 +0.0 -0.0 +1.1 -0.8	+0.4 -0.4 +0.0 -0.0 +2.4 -1.5
Bottom mass, m_b	+0.5 -0.8 +2.8 -2.4	+0.9 -1.3 +5.0 -4.6	+0.6 -0.8 +2.7 -2.3	+1.0 -1.3 +4.8 -4.8	+0.1 -0.1 +1.1 -0.8	+0.2 -0.2 +0.4 -0.4
PDF+ $\alpha_S+m_{c,b}$	+0.5 -0.8 +2.8 -2.4	+0.9 -1.3 +5.0 -4.6	+0.6 -0.8 +2.7 -2.3	+1.0 -1.3 +4.8 -4.8	+0.1 -0.1 +1.1 -0.8	+0.2 -0.2 +0.4 -0.4
Scales (μ_R, μ_F)	+0.5 -0.8 +2.8 -2.4	+0.9 -1.3 +5.0 -4.6	+0.6 -0.8 +2.7 -2.3	+1.0 -1.3 +4.8 -4.8	+0.1 -0.1 +1.1 -0.8	+0.2 -0.2 +0.4 -0.4
PDF+ $\alpha_S+m_{c,b}+\mu_{R,F}$	+0.5 -0.8 +2.8 -2.4	+0.9 -1.3 +5.0 -4.6	+0.6 -0.8 +2.7 -2.3	+1.0 -1.3 +4.8 -4.8	+0.1 -0.1 +1.1 -0.8	+0.2 -0.2 +0.4 -0.4

 Figure 3.17: Summary of theoretical uncertainties in prediction of W and Z boson cross-sections at 7TeV [63]

3.8.3.2 Computation of PDF+ α_s uncertainties

If PDF uncertainty and the $\alpha_s(m_Z^2)$ uncertainty are correlated then PDF+ α_s uncertainty at 68% C.L. or 1- σ uncertainty can be calculated. First calculate the 1- σ PDF uncertainty at fixed α_s value, and then compute 1- σ uncertainty in α_s with PDFs fixed at their central value, 1- σ change in α_s corresponds to the change of 0.001 in its value and 2- σ corresponds to the change of 0.002.

For example, if $\Delta\sigma_{PDF}$ is the PDF uncertainty in the cross section σ and $\Delta_{\alpha_s(m_Z^2)}\sigma$ is the α_s uncertainty, the combined PDFs+ α_s uncertainty in $\Delta\sigma$ is

$$\Delta\sigma = \sqrt{\Delta\sigma_{PDF}^2 + \Delta\sigma_{\alpha_s}^2} \quad (3.8.7)$$

Different PDFs groups used different strategies for computation of PDF+ α_s uncertainty.

3.8.3.3 NNPDF-Combined PDF and α_s uncertainties:

For NNPDF3.1 PDFs, PDF set are given with value α_s in the range from 0.108 to 0.124 in step of $\Delta\alpha_s = 0.002$ and few are also given with step of 0.001, for cross section which depends on the PDFs and the strong coupling $\sigma(PDF, \alpha_s)$, we have

$$(\delta\sigma)_{\alpha_s}^{\pm} = \sigma(PDF^{(\pm)}, \alpha_s^{(0)} \pm \delta_{\alpha_s}) - \sigma(PDF^0, \alpha_s^{(0)}) \quad (3.8.8)$$

where PDF^{\pm} is the value for the observable obtained when the value of α_s is varied 0.001, i.e., $\alpha_s^0 \pm \delta_{\alpha_s}$. The PDF+ α_s uncertainty is

$$(\delta\sigma)_{PDF+\alpha_s}^{\pm} = \sqrt{[(\delta\sigma)_{\alpha_s}^{\pm}]^2 + [(\delta\sigma)_{PDF}^{\pm}]^2} \quad (3.8.9)$$

with $(\delta\sigma)_{PDF}^{\pm}$ is the PDF uncertainty on the observable σ with the central value of α_s . Figure 3.18 shows the W^{\pm} and Z^0 cross section, multiplied by the leptonic branching ratio and uncertainties in cross section predictions by different PDF groups.

The percentage uncertainties in the NNLO predictions at 7 TeV energy for both 68% and 90% confidence levels using MSTW08 PDFs is summarized in Fig. 3.17 for W , W^+ , W^- , and Z bosons production cross section. The uncertainty in cross section ratios are also predicted.

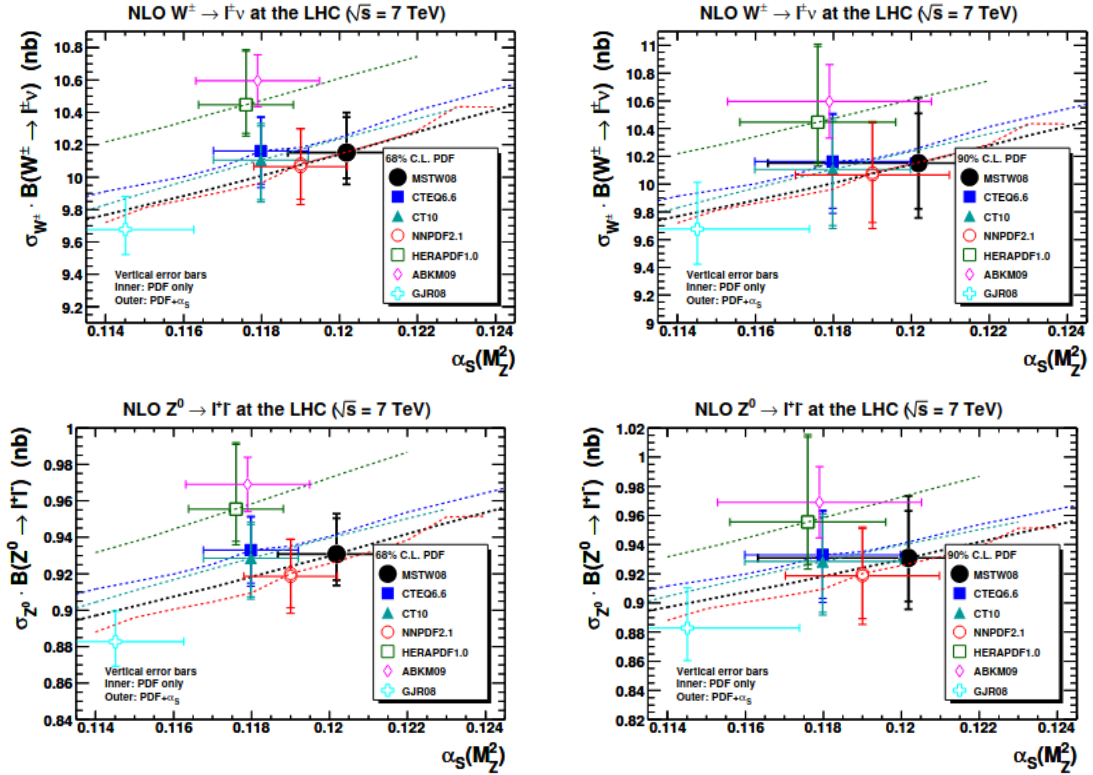


Figure 3.18: W^\pm and Z^0 total cross sections, plotted as a function of $\alpha_S(M_Z^2)$, at NLO. [63]

CHAPTER 4

Results and Discussions

4.1 Work Summary

The experimentally measured production cross section $\sigma \times BR(W \rightarrow l\nu, Z \rightarrow ll)$ of vector bosons is compared with the theoretical predictions of W , Z , W^+ and W^- vector boson using NNPDF3.1 PDF set. The cross sections are predicted at Leading-order (LO), Next-to-Leading Order (NLO) and Next-to-Next-to-Leading (NNLO) perturbative theory. The Uncertainties in the cross-section predictions including PDF, α_s , combined $PDF + \alpha_s$ are measured. The uncertainty in the prediction due to the choice of perturbative QCD scale, i.e., Factorisation scale μ_F and renormalisation scale μ_R are also measured. These uncertainties are measured for both confidence levels 68% C.L. and 90% C.L. The ratio of predicted cross sections of vector bosons are calculated with LO, NLO and NNLO. These predicted ratios are compared with the measured cross-section ratios at 68% C.L. and 90% C.L. The uncertainties in predictions due to choice of strong coupling constant α_s at 13 TeV and 14 TeV are measured.

The kinematics of vector bosons, transverse momentum (p_T), pseudo rapidity (η) and rapidity (y) at LO, NLO and NNLO are predicted, with variation of QCD scale parameter, μ_R and μ_F . The kinematics of decayed leptons from W and Z boson are also plotted.

For the prediction NNPDF3.1 PDF is used and for event generation we use POWHEG-V2, MadGraph and Pythia8.

4.2 NNPDF3.1 Parton Distribution Function

A precise understanding of PDF played an important role in the discovery of Higgs boson at LHC, and also gives a clear insight for the search of new physics at LHC. The NNPDF3.1 PDF is the most recent PDF set and is an up gradation of NNPDF3.0, and is released at LO, NLO and NNLO accuracy.

In the following plots Fig. 4.1, Fig. 4.2, Fig. 4.3 and Fig. 4.4 are the Parton Distribution Functions (PDFs) for the quarks and anti-quarks are plotted at various $\mu_F = Q^2$ for LO, NLO and NNLO.

4.2.1 NNPDF3.1 PDFs

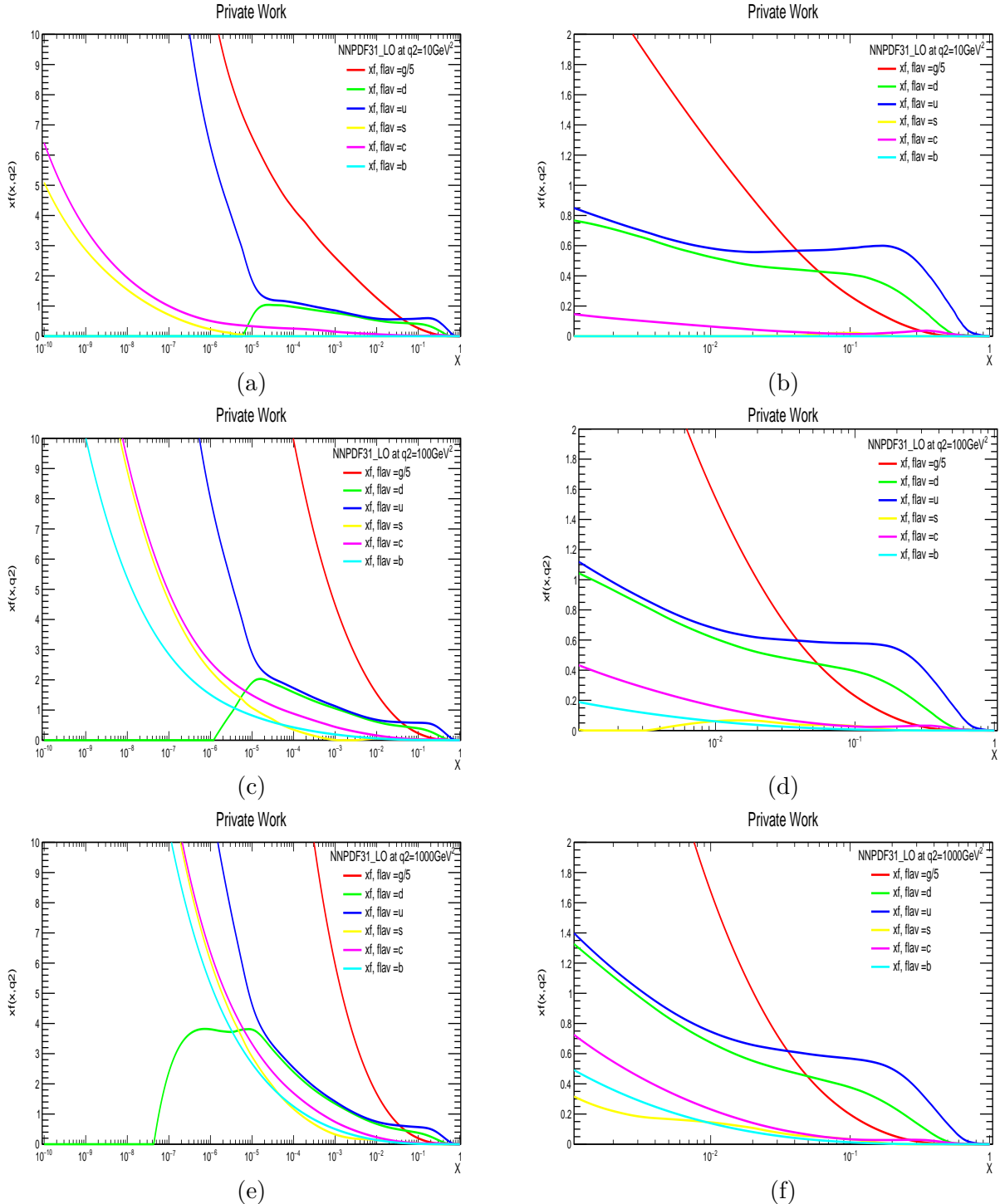


Figure 4.1: The NNPDF3.1-LO PDFs for the gluon (g), down (d), up(u), strange (s), charm (c) and bottom (b) quarks. (a), (b): for $Q^2 = 10 \text{ GeV}^2$, (c), (d): for $Q^2 = 100 \text{ GeV}^2$ and (e), (f): for $Q^2 = 1000 \text{ GeV}^2$

CHAPTER 4: RESULTS AND DISCUSSIONS

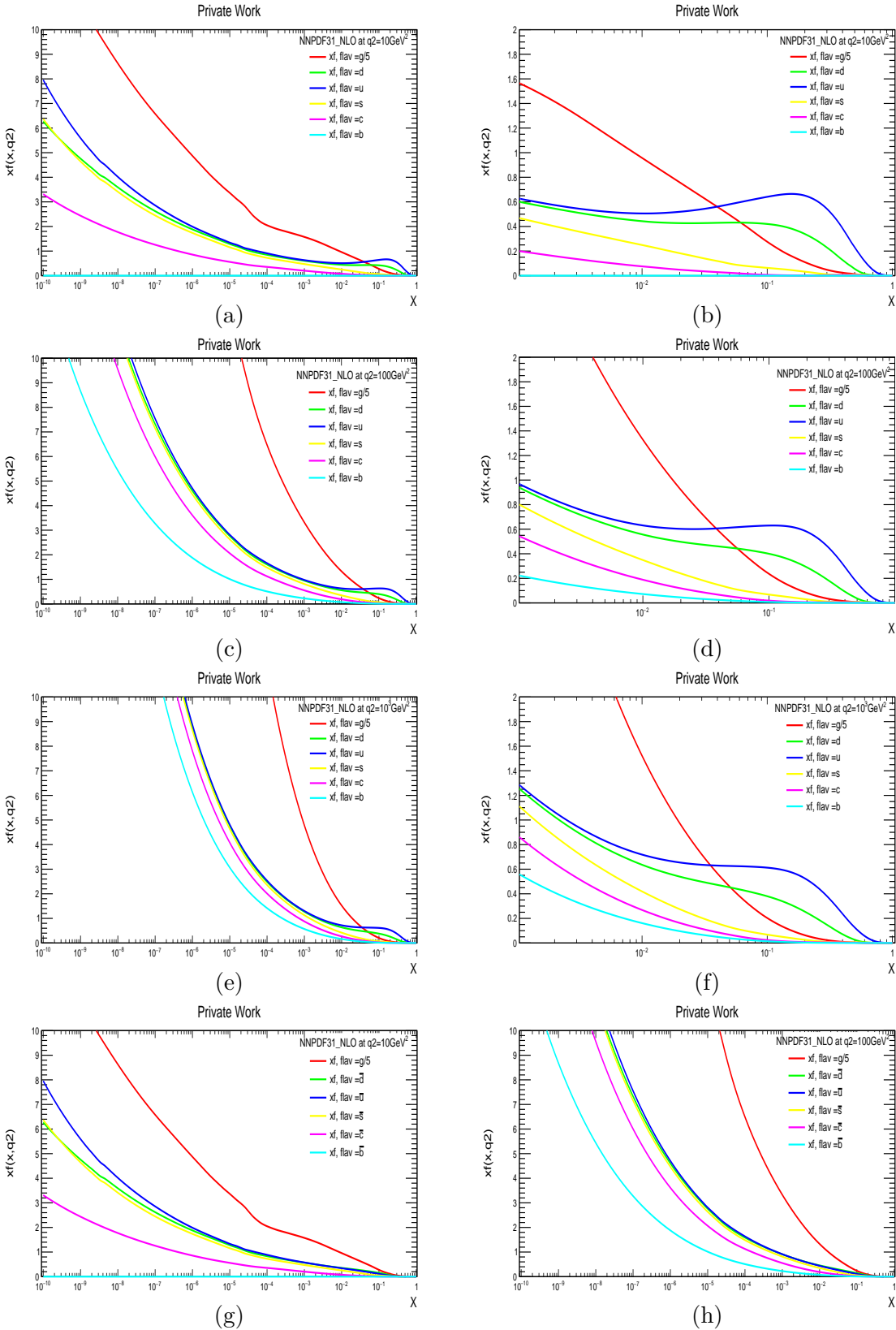


Figure 4.2: The NNPDF3.1-NLO PDFs as a function of x for the gluon (g), down (d), up(u), strange (s), charm (c) and bottom (b) quarks and also for the corresponding anti-quarks. (a), (b): for $Q^2 = 10 \text{ GeV}^2$, (c), (d): for $Q^2 = 100 \text{ GeV}^2$ and (e), (f): for $Q^2 = 1000 \text{ GeV}^2$, (g), (H): for anti-quarks at 10 GeV^2 and 100 GeV^2 respectively.

CHAPTER 4: RESULTS AND DISCUSSIONS

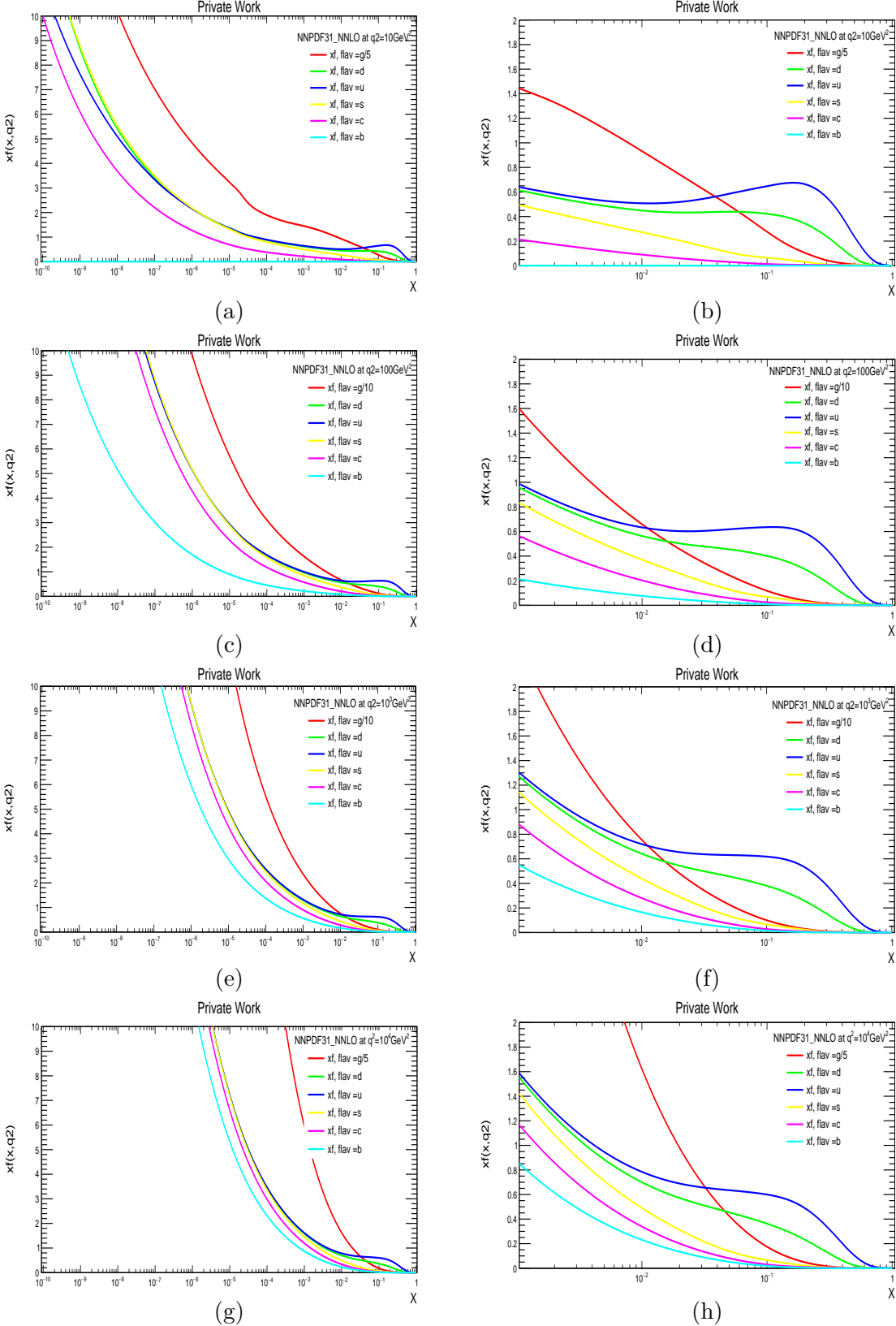


Figure 4.3: The NNPDF3.1-NNLO PDFs as a function of x for the gluon (g), down (d), up(u), strange (s), charm (c) and bottom (b) quarks. (a), (b): for $Q^2 = 10 \text{ GeV}^2$, (c), (d): for $Q^2 = 100 \text{ GeV}^2$ and (e), (f): for $Q^2 = 1000 \text{ GeV}^2$, (g), (h): for 10000 GeV^2 . The gluon PDFs are scaled down by a factor of 5 and 10.

CHAPTER 4: RESULTS AND DISCUSSIONS

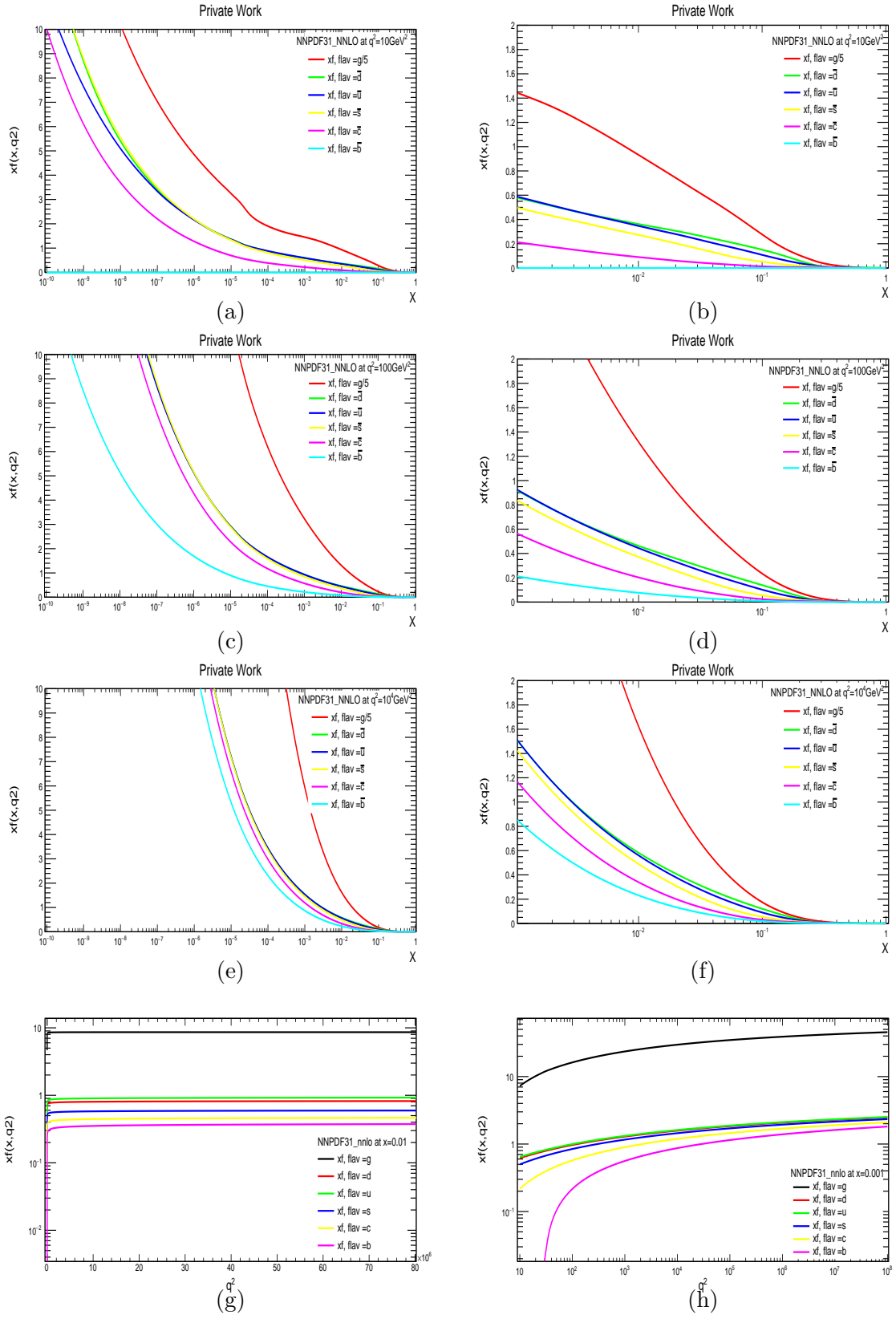


Figure 4.4: The NNPDF3.1-NNLO PDFs as a function of x for the gluon (g), down (d), up (u), strange (s), charm (c) and bottom (b) anti-quarks. (a), (b): for $Q^2 = 10 \text{ GeV}^2$, (c), (d): for $Q^2 = 100 \text{ GeV}^2$ and (e), (f): for $Q^2 = 10000 \text{ GeV}^2$, (g), (h): PDF function of quarks as a function of q . The gluon PDFs are scaled down by a factor of 5.

4.3 Results

4.3.1 Measurements vs Predictions

The comparison of the measurement of the inclusive production cross section times leptonic branching ratios of W and Z bosons with the theoretical predictions is made. The cross sections are measured with both CMS and ATLAS data at 13TeV with $\mathcal{L}_{int} = 81\text{ pb}^{-1}$ in proton-proton collision. The maximum instantaneous luminosity measured was $L = 1.7 \times 10^{33}\text{ cm}^{-2}\text{s}^{-1}$. The theoretical prediction for W , Z , W^+ and W^- production cross section times $\text{BR}(W \rightarrow l\nu, Z \rightarrow ll)$ are predicted for both 13 TeV and 14 TeV center of mass energy and we also made a comparison with the previous results obtained at 7 TeV and 8 TeV . The Theoretical predictions are made using NNPDF3.1 PDF at LO, NLO and NNLO and various uncertainties in predictions are also measured.

The ratios of the cross sections i.e $R_{W^\pm} = \frac{\sigma_{W^\pm}}{\sigma_{W^-}}$ and $R_{WZ} = \frac{\sigma_{W^\pm}}{\sigma_Z}$ measured at 8 TeV and 13 TeV are compared and prediction for 14 TeV is made.

4.3.1.1 8 TeV

The Tables 4.1 and 4.2 shows the measured cross sections of W and Z boson times branching fraction $\sigma \times \text{BR}(W \rightarrow l\nu, Z \rightarrow ll)$ and theoretically predicted cross sections. The uncertainty in the measured values are due to statistical, systematic and luminosity errors. The measured values are taken from reference [60].

Table 4.1: The measured total σ^{tot} cross sections for leptonic decay channels (electron, muon) of W^- , W^+ , W^\pm and Z -bosons at CMS with 8 TeV , 18.2 pb^{-1} , and predicted total cross section at 8 TeV . The uncertainties in measurement due to statistical, systematic and luminosity error. The NNPDF3.1-NNLO PDF is used for the predictions.

channel	Measured Cross section [nb]	Predicted Cross section [nb] (value±PDF)
W^-	$5.09 \pm 0.02 \pm 0.11 \pm 0.18$	5.21 ± 0.04
W^+	$7.11 \pm 0.03 \pm 0.14 \pm 0.13$	7.39 ± 0.06
W^\pm	$12.21 \pm 0.02 \pm 0.55 \pm 0.43$	12.60 ± 0.08
Z	$1.15 \pm 0.01 \pm 0.02 \pm 0.03$	1.26 ± 0.01

Table 4.2: Measured values with statistical and systematic errors and predicted Ratios W^+/W^- and W^\pm/Z at 8 TeV . For prediction NNPDF3.1-NNLO PDF is used.

Channel	Measured Ratio	Predicted Ratio (value±PDF)
W^+/W^-	$1.40 \pm 0.01 \pm 0.02$	1.42 ± 0.01
W^\pm/Z	$10.63 \pm 0.11 \pm 0.25$	10.00 ± 0.11

4.3.1.2 13 TeV

Tables 4.3 and 4.4 show the measured cross section of vector bosons and predictions at 13 TeV with NNPDF3.1-NNLO PDF.

Table 4.3: The measured [57] [61] total σ^{tot} cross sections with statistical, systematic and luminosity error for the electron channel of W^- , W^+ , W^\pm and Z -boson, and predicted total cross section at 13 TeV. The NNPDF3.1-NNLO PDF is used for the predictions.

channel	Measured Cross section [nb]	Predicted Cross section [nb] (value \pm PDF \pm α_s \pm PDF+ α_s)
W^-	$8.79 \pm 0.02 \pm 0.24 \pm 0.18$	$8.95 \pm 0.07 \pm 0.07 \pm 0.09$
W^+	$11.83 \pm 0.02 \pm 0.34 \pm 0.25$	$12.03 \pm 0.11 \pm 0.09 \pm 0.14$
W^\pm	$20.64 \pm 0.02 \pm 0.55 \pm 0.43$	$20.98 \pm 0.13 \pm 0.16 \pm 0.20$
Z	$1.98 \pm 0.007 \pm 0.04 \pm 0.04$	$2.14 \pm 0.02 \pm 0.01 \pm 0.02$

Table 4.4: Measured ratio with statistical ans systematic errors and predicted Ratios W^+/W^- and W^\pm/Z at 13 TeV. For prediction NNPDF3.1-NNLO PDF is used. The measured values are taken from reference [57]

Channel	Measured Ratio	Predicted Ratio (value \pm PDF \pm PDF+ α_s)
W^+/W^-	$1.295 \pm 0.003 \pm 0.01$	$1.34 \pm 0.016 \pm 0.02$
W^\pm/Z	$10.31 \pm 0.04 \pm 0.20$	$9.8 \pm 0.09 \pm 0.13$

4.3.1.3 14 TeV

Tables 4.5 and 4.6 shows the predicted cross section for the vector bosons at 14 TeV with NNPDF3.1-NNLO PDF.

Table 4.5: Predicted total cross section of W^- , W^+ , W^\pm and Z boson at 14 TeV .The NNPDF3.1-NNLO PDF is used for the predictions.

channel	Cross section [nb] (To be measured)	Predicted Cross section [nb] (value \pm PDF \pm α_s \pm PDF+ α_s)
W^-	_____	$9.70 \pm 0.08 \pm 0.14 \pm 0.16$
W^+	_____	$12.94 \pm 0.12 \pm 0.12 \pm 0.23$
W^\pm	_____	$22.63 \pm 0.15 \pm 0.17 \pm 0.22$
Z	_____	$2.316 \pm 0.02 \pm 0.02 \pm 0.02$

Table 4.6: Predicted Ratios W^+/W^- and W^\pm/Z at 14 TeV . For prediction NNPDF3.1-NNLO PDF is used.

Channel	Cross section ratios (To be measured)	Predicted ratios (value \pm PDF \pm PDF+ α_s)
W^+/W^-	_____	$1.33 \pm 0.01 \pm 0.03$
W^\pm/Z	_____	$9.77 \pm 0.09 \pm 0.21$

4.4 Theoretical Predictions and Uncertainties in Cross Section of W and Z Bosons.

The predicted increase in measurement of cross section of W and Z bosons with the center of mass energy can be seen in Fig. 4.5. The cross section value at 14 TeV yet to be measured. The Predicted cross section of W , Z , W^+ and W^- in pb are plotted with various uncertainties in predictions. These uncertainties are determined at both 68% and 90% C.L. The errors are determined with both Monte-Carlo replicas and Hessian error eigen vector method. The variation in predictions with the variation in QCD scale are also determined. Results are shown in Fig. 4.10 Fig. 4.11, Fig. 4.12, Fig. 4.13 and Fig. 4.14

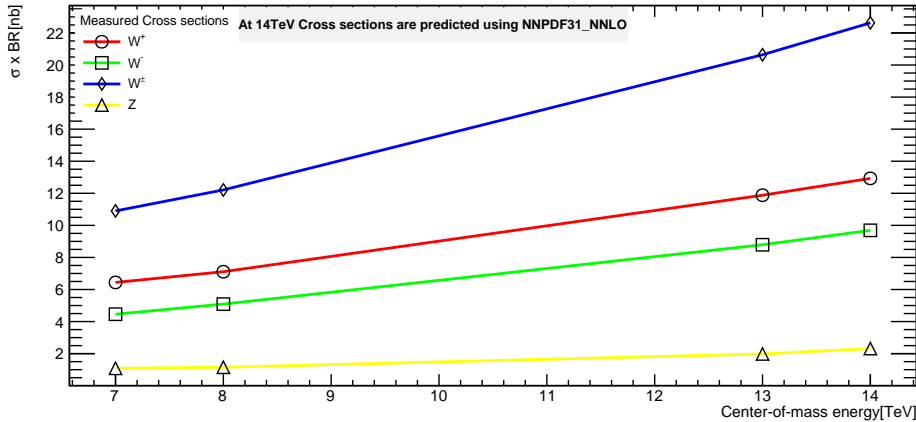
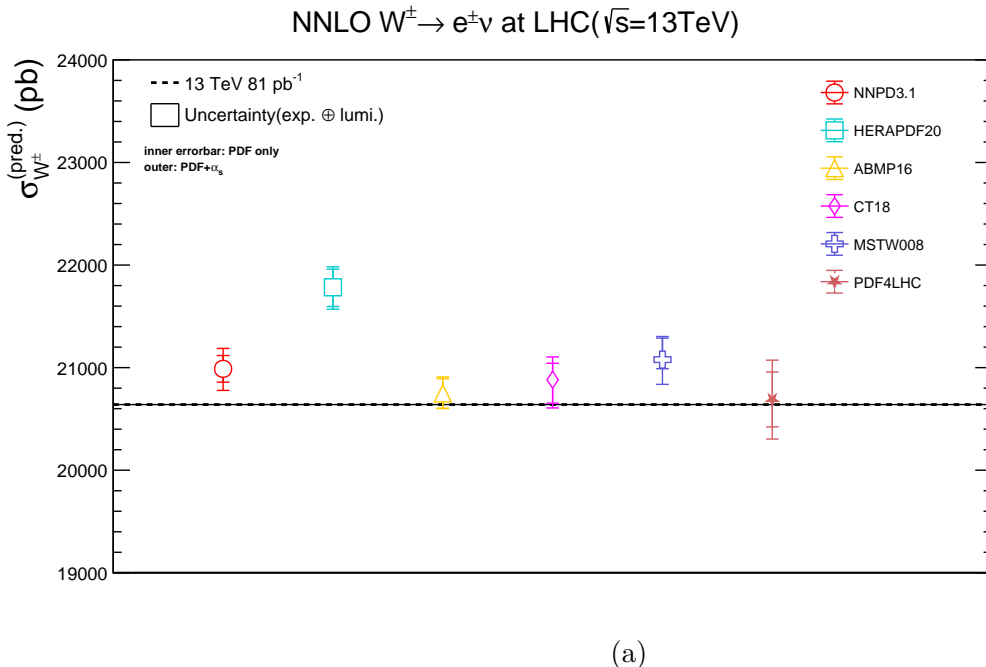
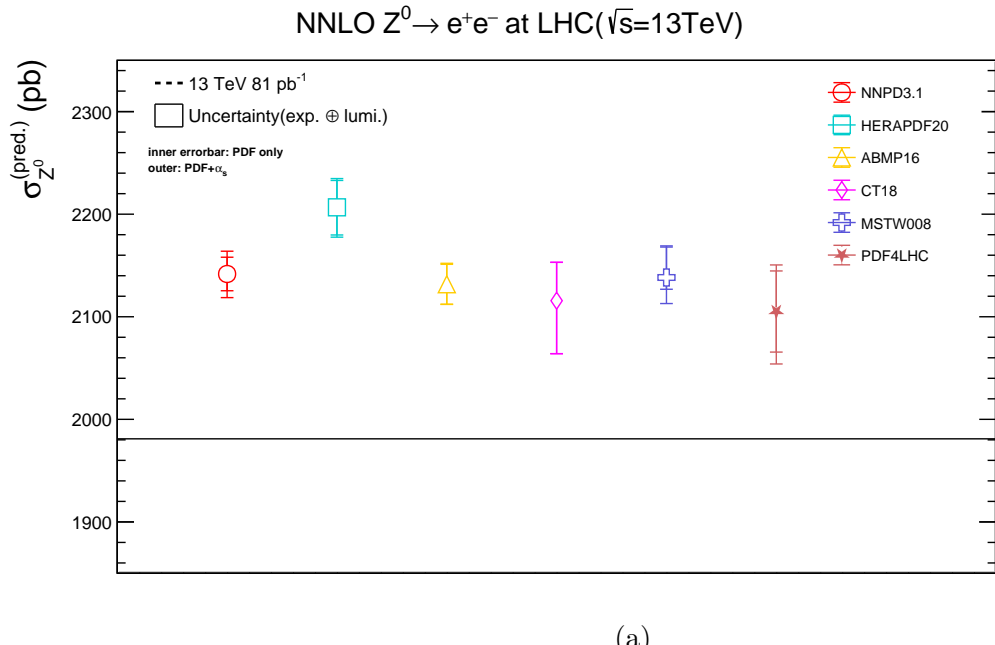


Figure 4.5: Figure 4.5 shows measured cross section of (W^+ , W^- , Z and W^\pm) with the variation of center of mass energy and at 14 TeV value of cross section is predicted at NNLO.



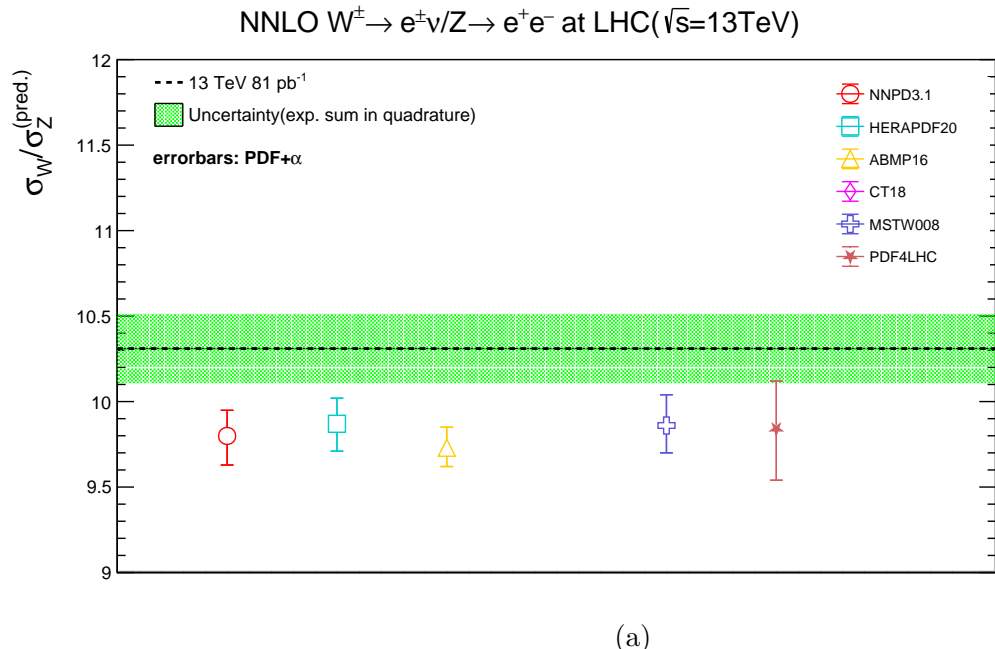
(a)

Figure 4.6: 4.6a showing the predicted cross section of W boson at 13 TeV NNLO using various Parton Distribution Function. The measured values are taken from [57]



(a)

Figure 4.7: 4.7a showing the predicted cross section of Z boson at 13 TeV NNLO using various Parton Distribution Function. The measured values are taken from [57]



(a)

Figure 4.8: 4.8a showing the predicted cross section Ratio of W and Z boson at 13 TeV NNLO using various Parton Distribution Functions. The measured values are taken from [57]

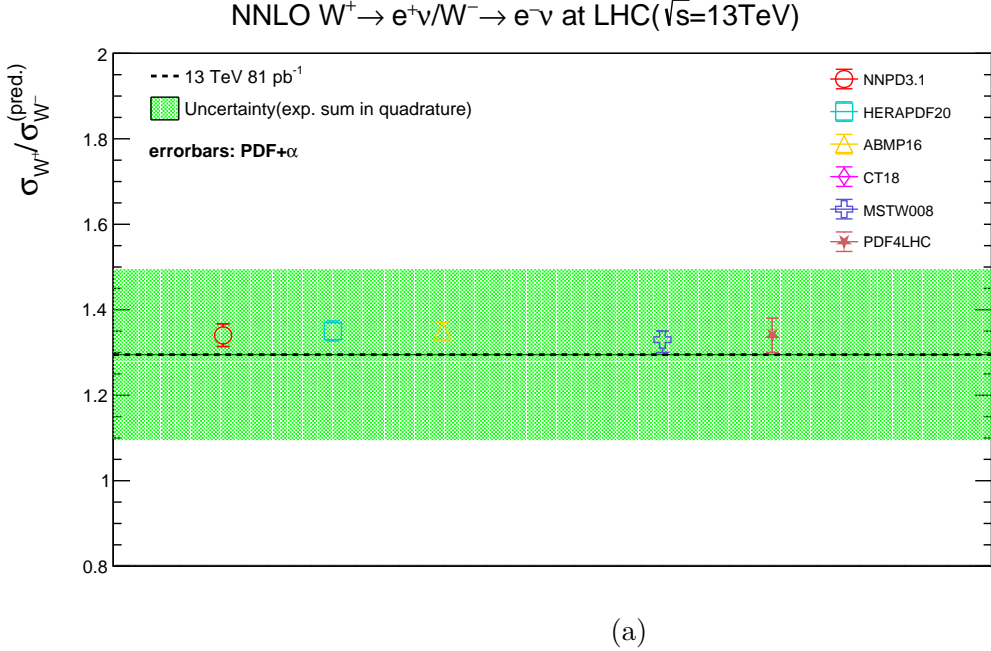


Figure 4.9: 4.9a showing the predicted cross section Ratio of W^+ and W^- boson at 13 TeV NNLO using various Parton Distribution Functions. The measured values are taken from [57]

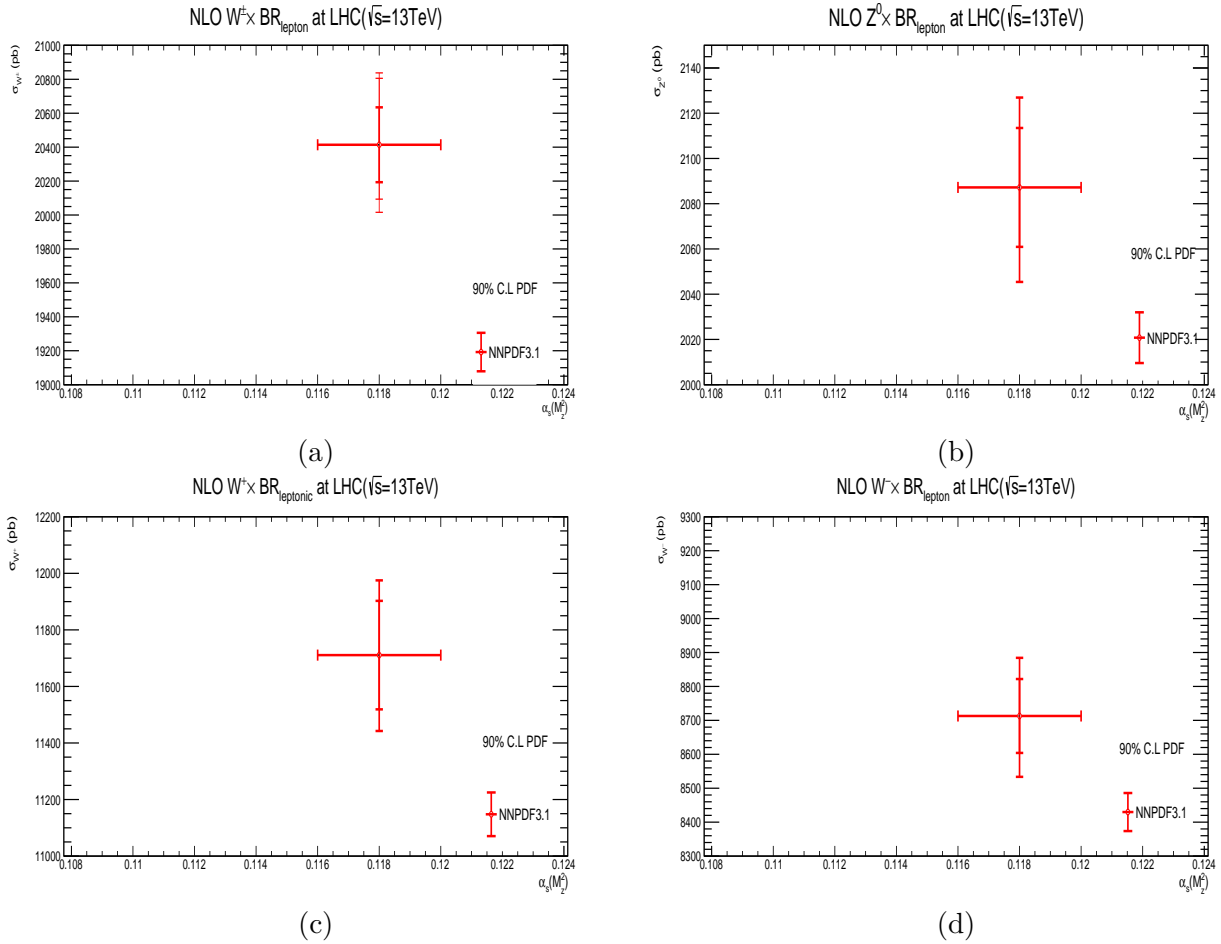


Figure 4.10: 4.10a and 4.10b are the NLO predictions of W and Z boson at 13TeV , 4.10c and 4.10d are for the W^+ and W^- bosons at 13TeV .

CHAPTER 4: RESULTS AND DISCUSSIONS

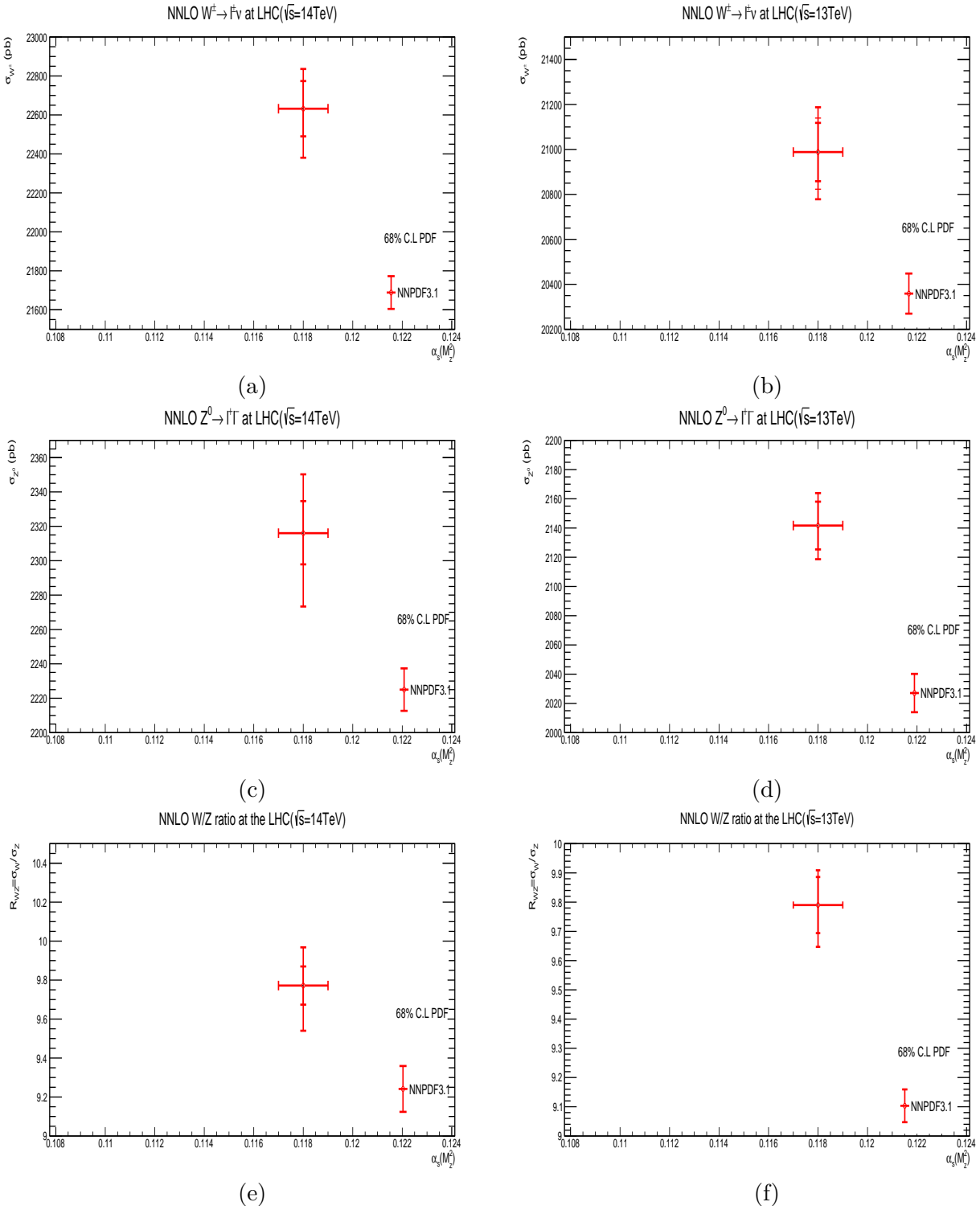


Figure 4.11: In Figure: 4.11a 4.11b are the NNLO predictions of W boson production cross section at 13 TeV and 14 TeV with 68% C.L. uncertainties. 4.11c 4.11d are the Z boson production cross section and 4.11e 4.11f are the predicted ratio of W and Z boson production cross section at 13TeV and 14TeV . The vertical error bars on prediction represent: inner (PDF), middle (α_s), outer (PDF+ α_s combined) error.

CHAPTER 4: RESULTS AND DISCUSSIONS

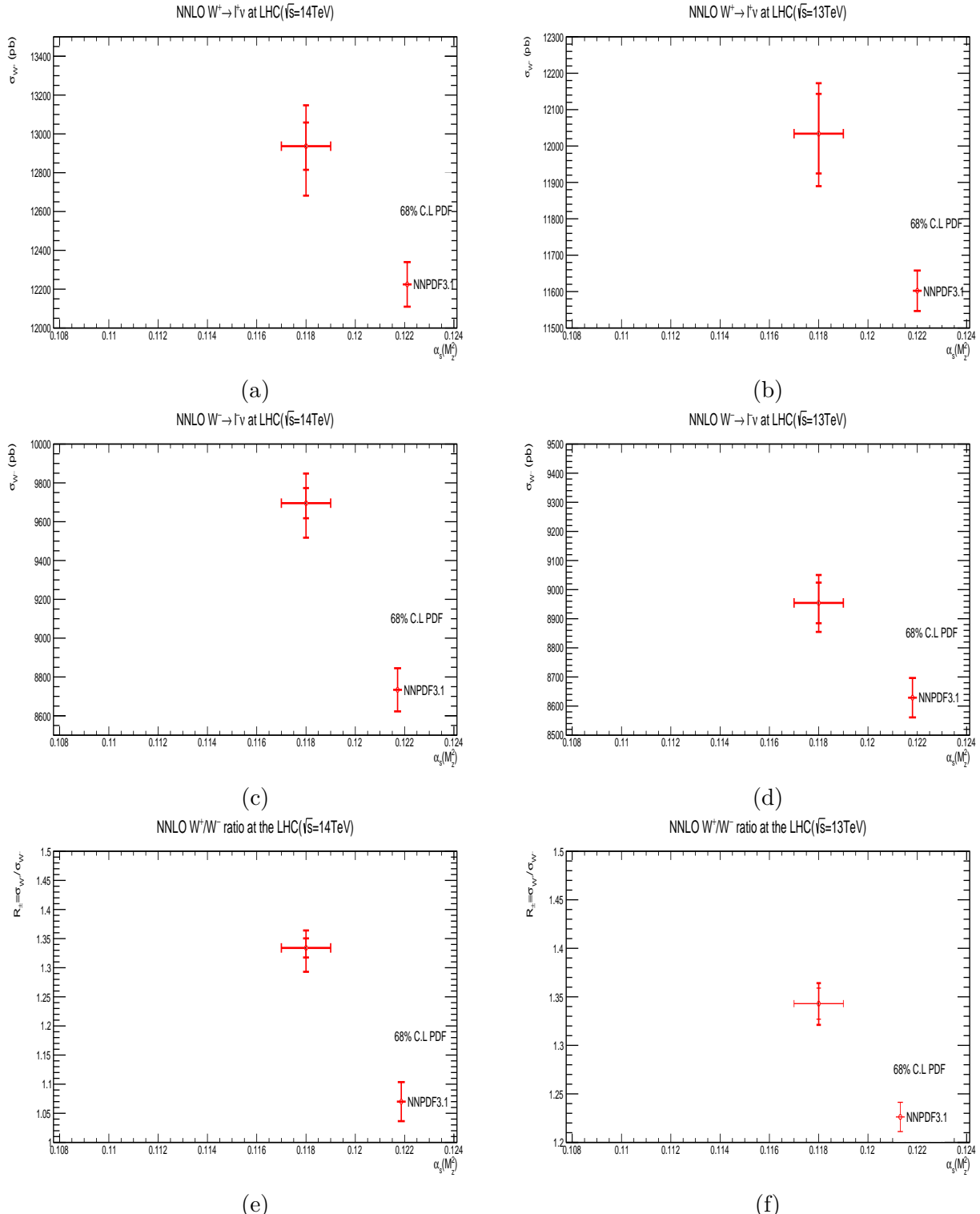


Figure 4.12: In Figure 4.12a 4.12b are the NNLO predictions of W^+ boson production cross section at 13 TeV and 14 TeV with 68% C.L. uncertainties. 4.12c 4.12d are the W^- boson production cross section and 4.12e 4.12f are the predicted ratio of W^+ and W^- boson production cross section at 13TeV and 14TeV . The vertical error bars on prediction represent: inner (PDF), middle (α_s), outer (PDF+ α_s combined) error.

CHAPTER 4: RESULTS AND DISCUSSIONS

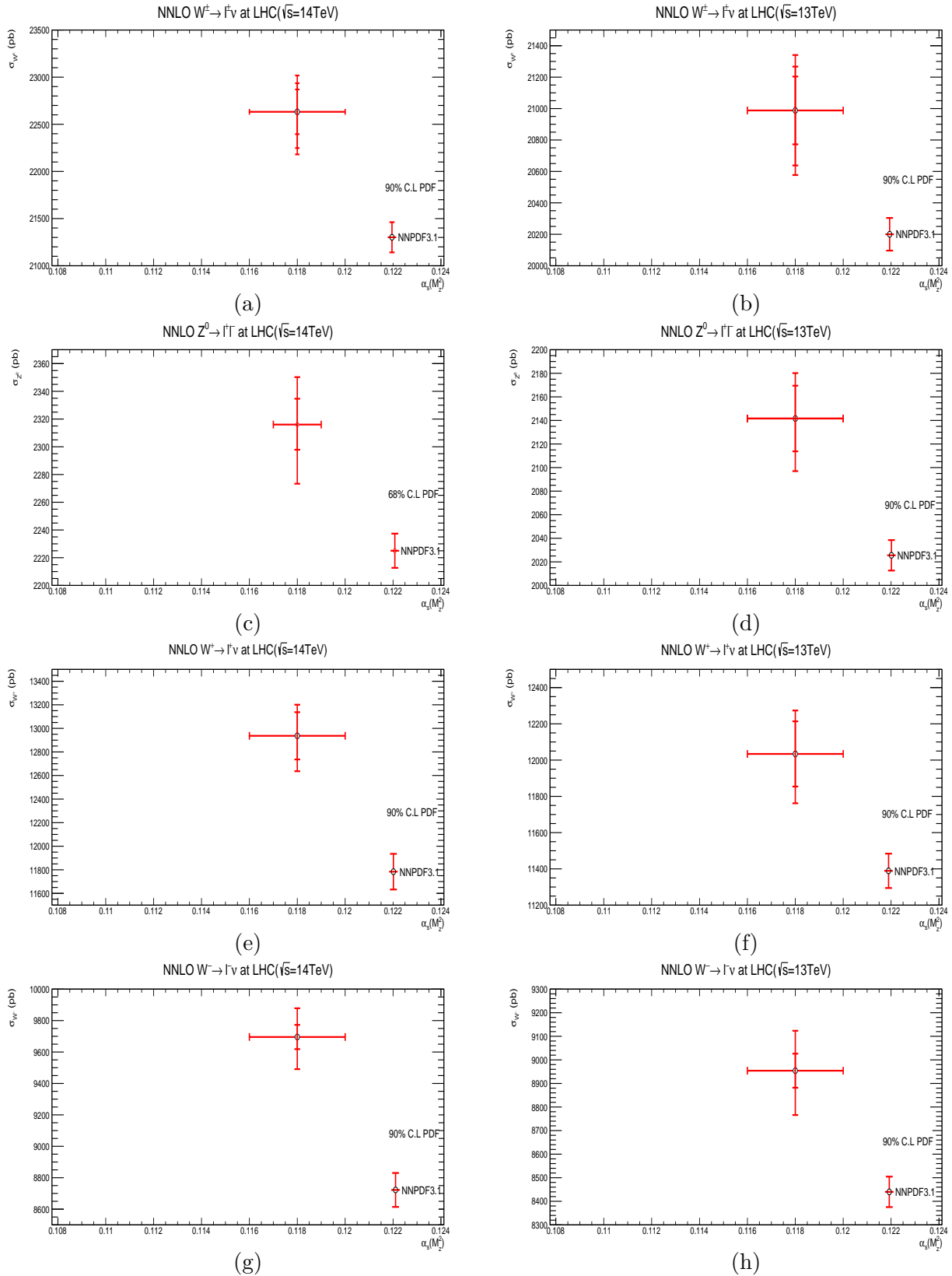


Figure 4.13: In Figure, 4.13a 4.13b are the NNLO predictions of W boson production cross section at 13 TeV and 14 TeV with 90% C.L. uncertainties. 4.13c 4.13d are the Z boson production cross section and 4.13e 4.13f and 4.13g 4.13h showing the predicted cross section of W^+ and W^- boson at 13 TeV and 14TeV respectively. The vertical error bars on prediction represent: inner (PDF), middle (α_s), outer (PDF+ α_s combined) error.

CHAPTER 4: RESULTS AND DISCUSSIONS

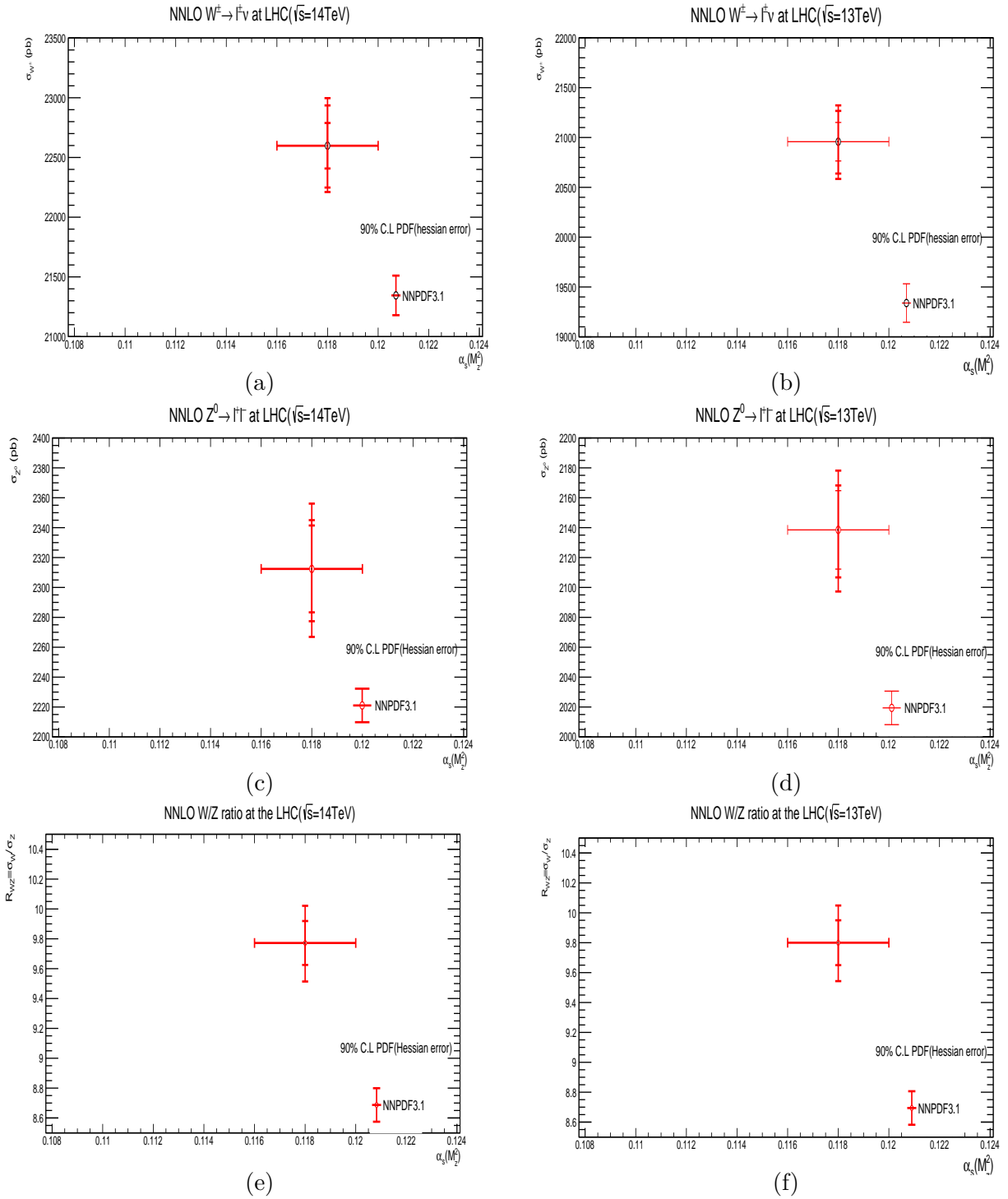


Figure 4.14: In Figure, 4.14a 4.14b are the NNLO predictions of W^+ boson production cross section at 13 TeV and 14 TeV with 90% C.L. uncertainties. 4.14c 4.14d are the Z boson production cross section and 4.14e 4.14f are the predicted ratio of W and Z boson production cross section at 13TeV and 14TeV. These uncertainties are measured with hessian error vector method in which vertical error bars represent inner (PDF), middle (α_s) and outer (PDF+ α_s combined) uncertainties.

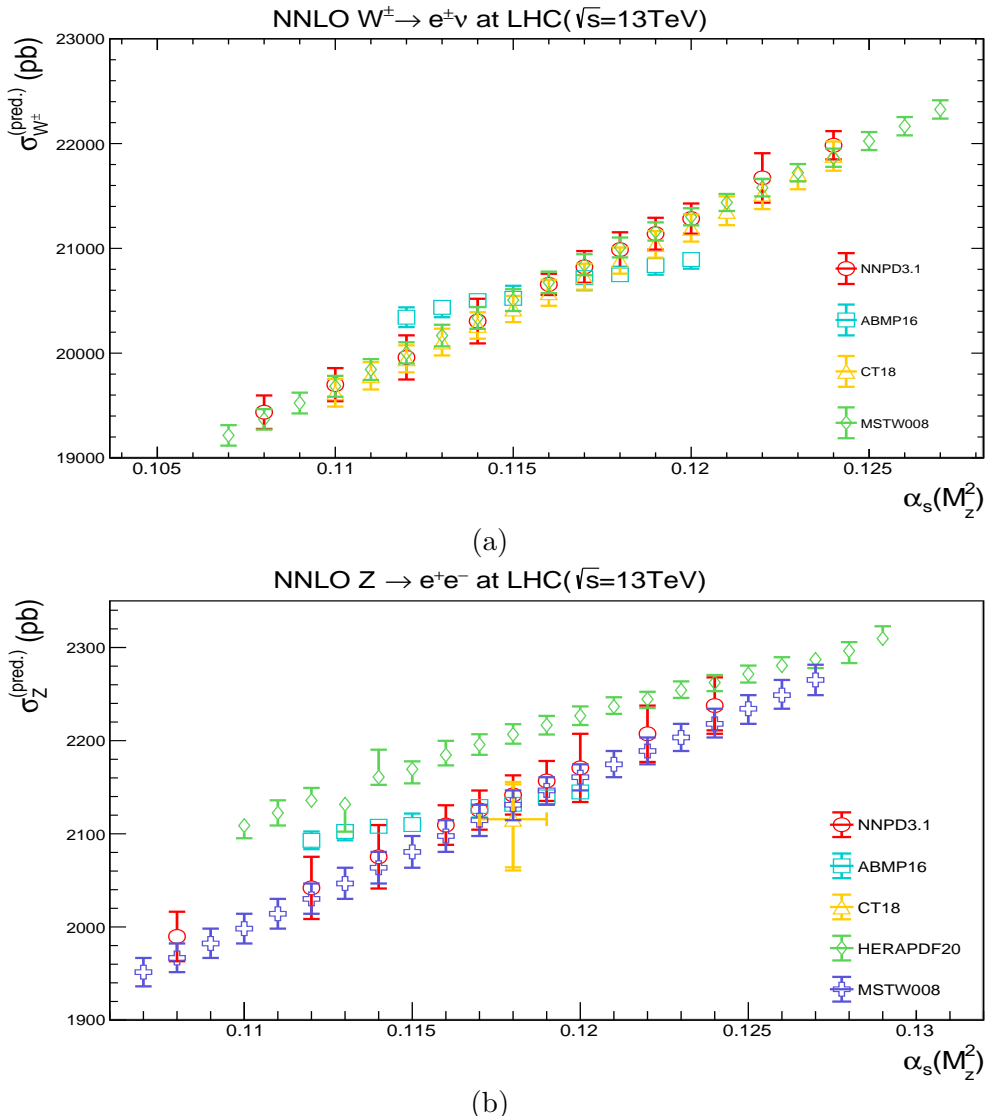


Figure 4.15: The predicted increase in production cross section of W and Z vector boson with the choice of $\alpha_s(M_Z^2)$ at 13 TeV .

4.4.0.1 Variation In Cross Section With QCD Scale

The predicted increase in cross section values of W and Z boson with the change in value of strong coupling constant α_s at 13 TeV and 14 TeV is shown in Fig. 4.15a 4.15b 4.16a 4.16b. The variation in the predicted cross section with the change of factorization (μ_F) and re-normalisation (μ_R) scale simultaneously at 13 TeV and 14 TeV is shown in Fig. 4.17, 4.18, 4.19 and 4.20.

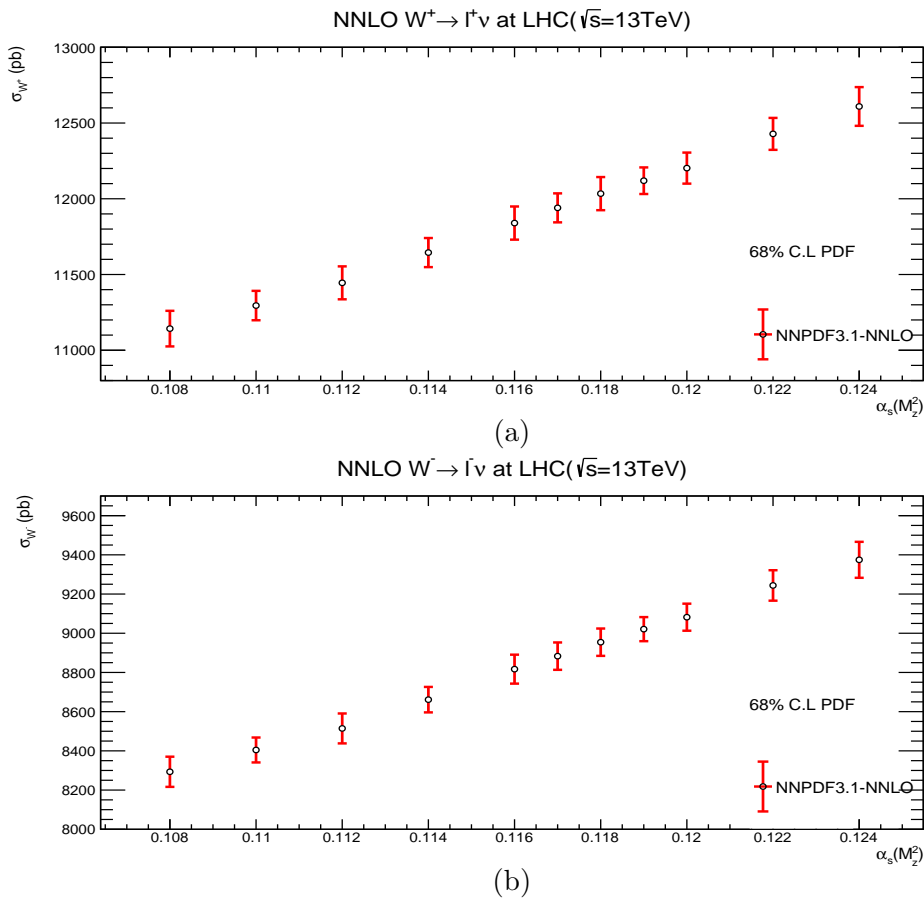
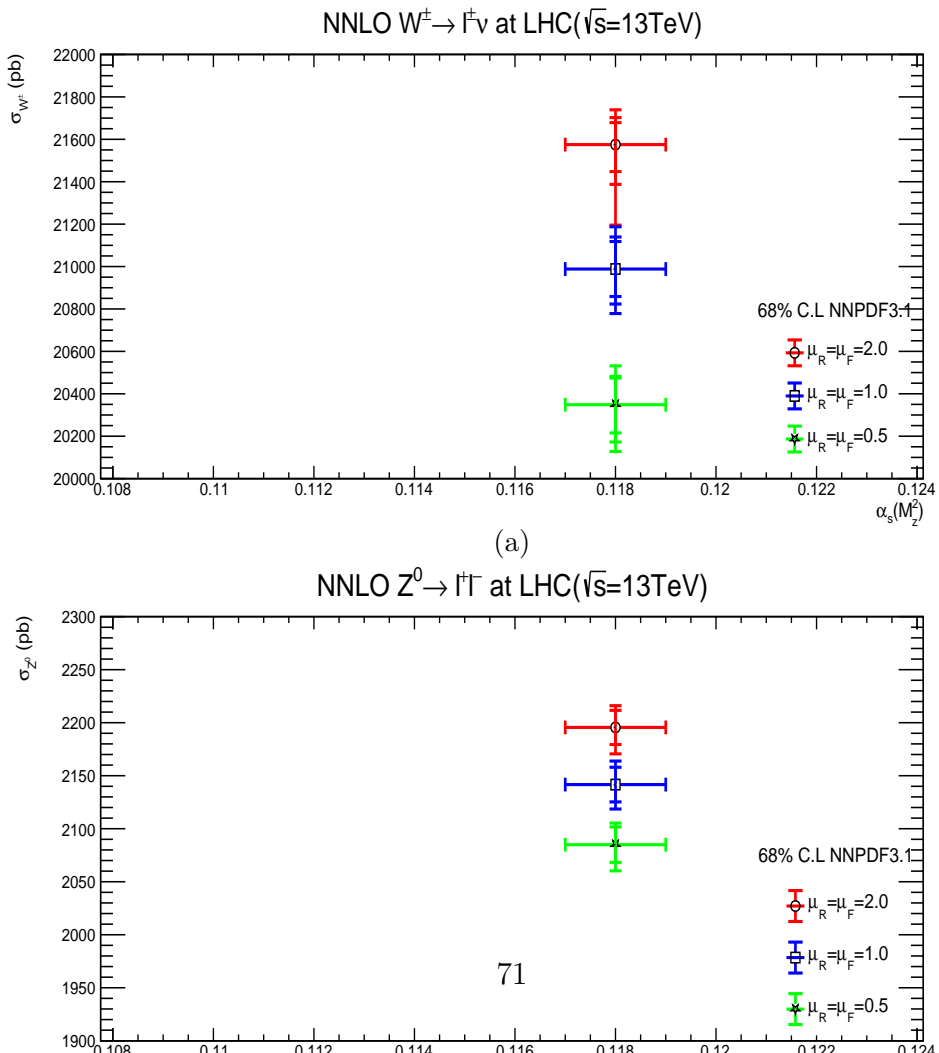


Figure 4.16: The predicted increase in production cross section of W^+ , W^- vector boson with the choice of $\alpha_s(M_Z^2)$ at 13 TeV .



CHAPTER 4: RESULTS AND DISCUSSIONS

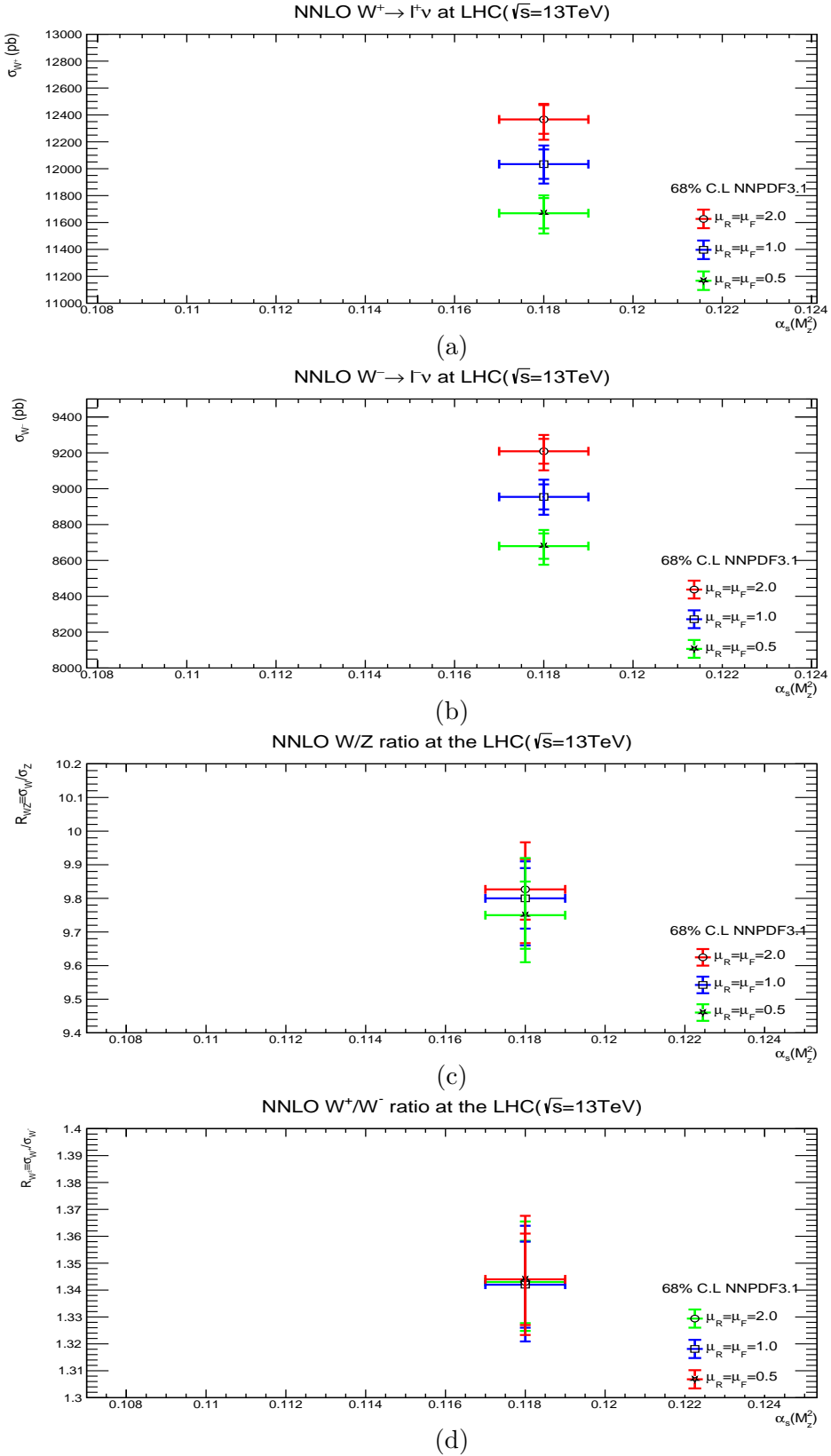


Figure 4.18: In figure 4.18a and 4.18b shows the predicted change in cross section of W^+ and W^- boson with the change in factorisation μ_R and re-normalisation μ_F scale and 4.18c and 4.18d are the cross section ratio of W to Z and W^+ to W^- boson. The vertical error bars on prediction represent: inner (PDF), middle (α_s), outer (PDF+ α_s combined) error.

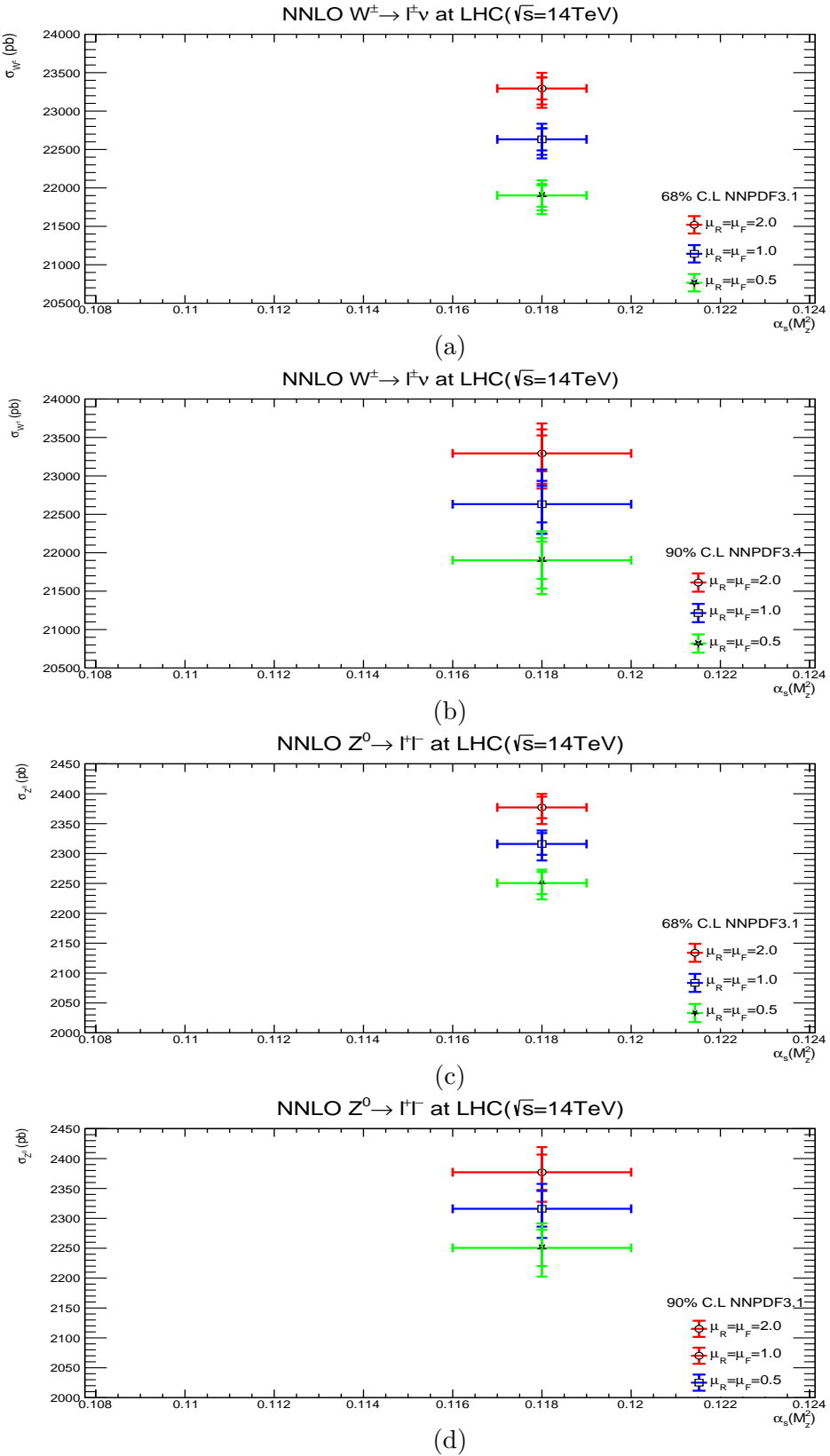


Figure 4.19: The predicted change in cross section of W and Z boson with the change in factorisation μ_R and re-normalisation μ_F scale at 14 TeV . 4.19a 4.19c, with $68\% \text{ } C.L.$ and 4.19b 4.19d with $90\% \text{ } C.L..$ The vertical error bars on prediction represent: inner (PDF), middle (α_s), outer (PDF+ α_s combined) error.

CHAPTER 4: RESULTS AND DISCUSSIONS

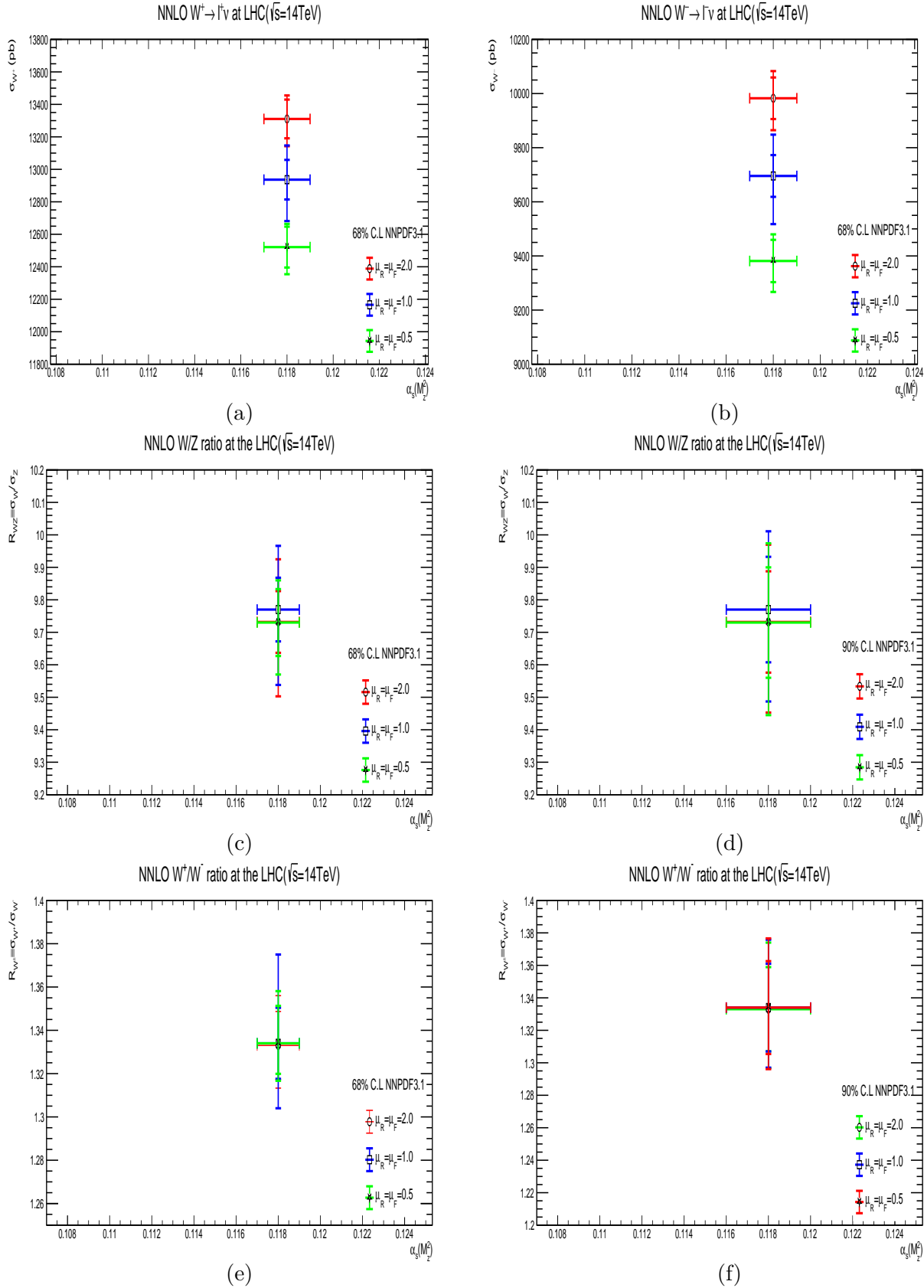


Figure 4.20: In figure 4.20a 4.20b showing the cross section of W^+ and W^- boson with different QCD scales at 68%*C.L.* uncertainties. 4.20c 4.20d represent the predicted change in cross section ratio of W and Z boson with QCD scales and 4.20e 4.20f for the W^+ and W^- boson similarly.

4.5 Kinematics of W and Z Boson

In this section generator level kinematic distributions of W^+ , W^- and Z boson is presented, for LO, NLO and NNLO predictions. The kinematics are plotted at 13 and 14 TeV with QCD scale variation. The kinematics of decaying leptons from the $W \rightarrow l\nu$ and $Z \rightarrow ll$ process are also presented.

4.5.1 Transverse Momentum and Pseudo Rapidity Distribution

Figs. 4.21, 4.22, 4.23 and 4.24 show the generator level distribution of kinematics of W and Z bosons at 13 TeV and 14 TeV

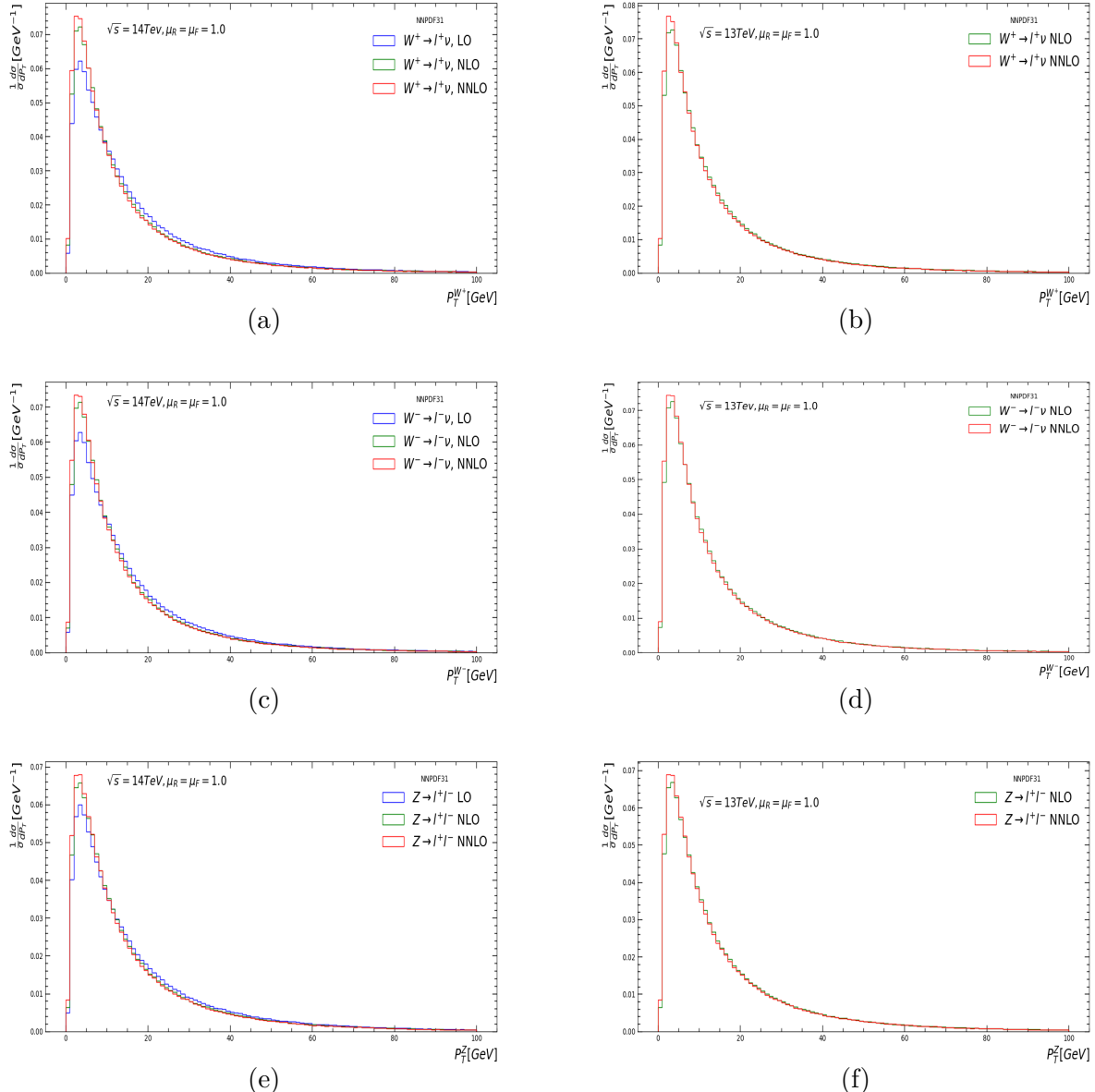


Figure 4.21: In figure 4.21a, 4.21c, 4.21e are the theoretically predicted transverse momentum distribution of W^+ , W^- and Z boson at 14 TeV with LO, NLO, and NNLO. 4.21b, 4.21d, 4.21f for the 13 TeV for NLO and NNLO.

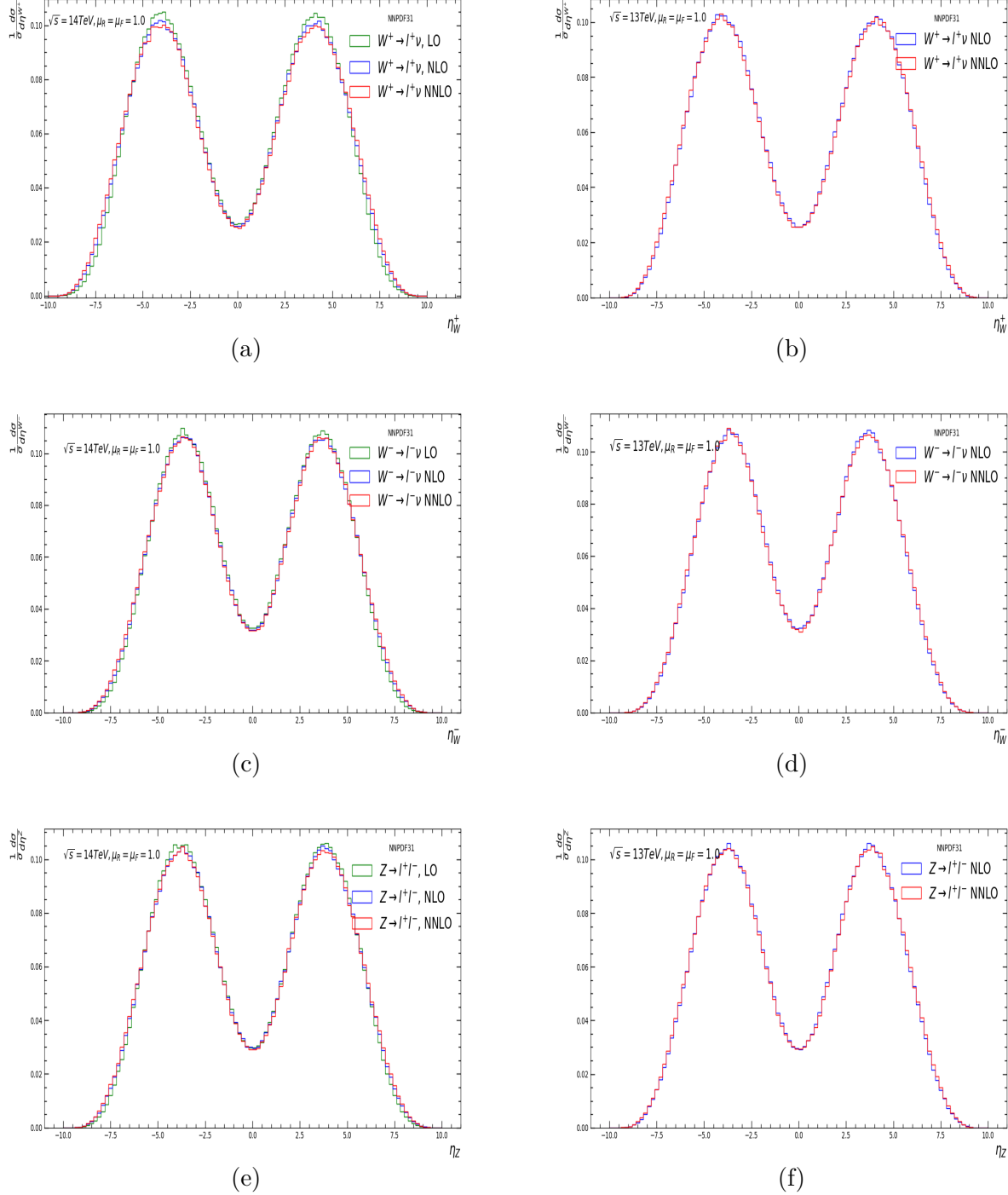


Figure 4.22: In figure 4.22a, 4.22c, 4.22e are the generator level theoretically predicted pseudo rapidity distribution of W^+ , W^- and Z boson at 14 TeV with LO, NLO, and NNLO. 4.22b, 4.22d, 4.22f for the 13 TeV for NLO and NNLO.

CHAPTER 4: RESULTS AND DISCUSSIONS

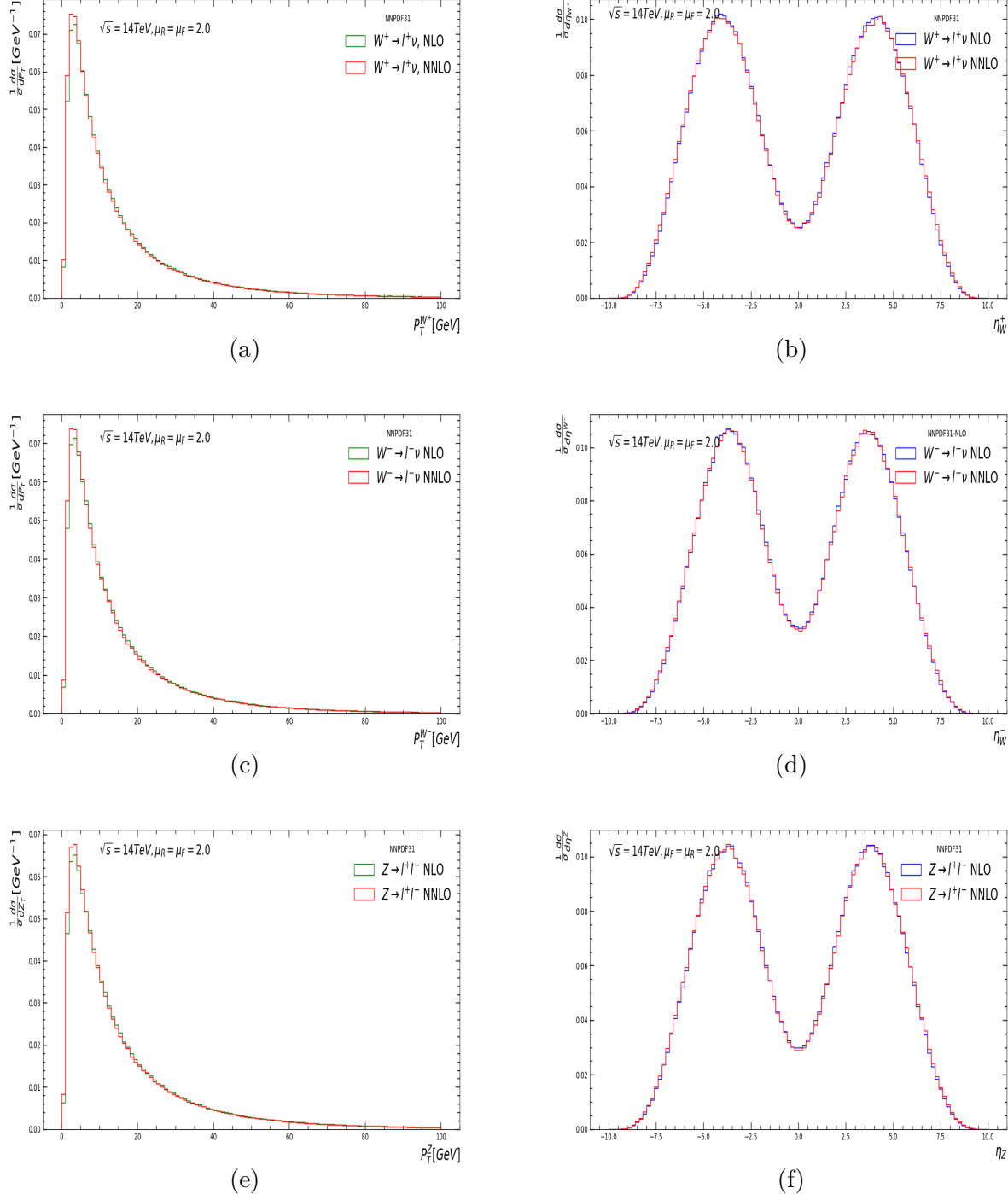


Figure 4.23: In figure 4.23a, 4.23c, 4.23e are the generator level transverse momentum distribution of W^+ , W^- and Z boson at 14 TeV with different QCD scales. 4.23b, 4.23d, 4.23f are the pseudo rapidity distribution for NLO and NNLO.

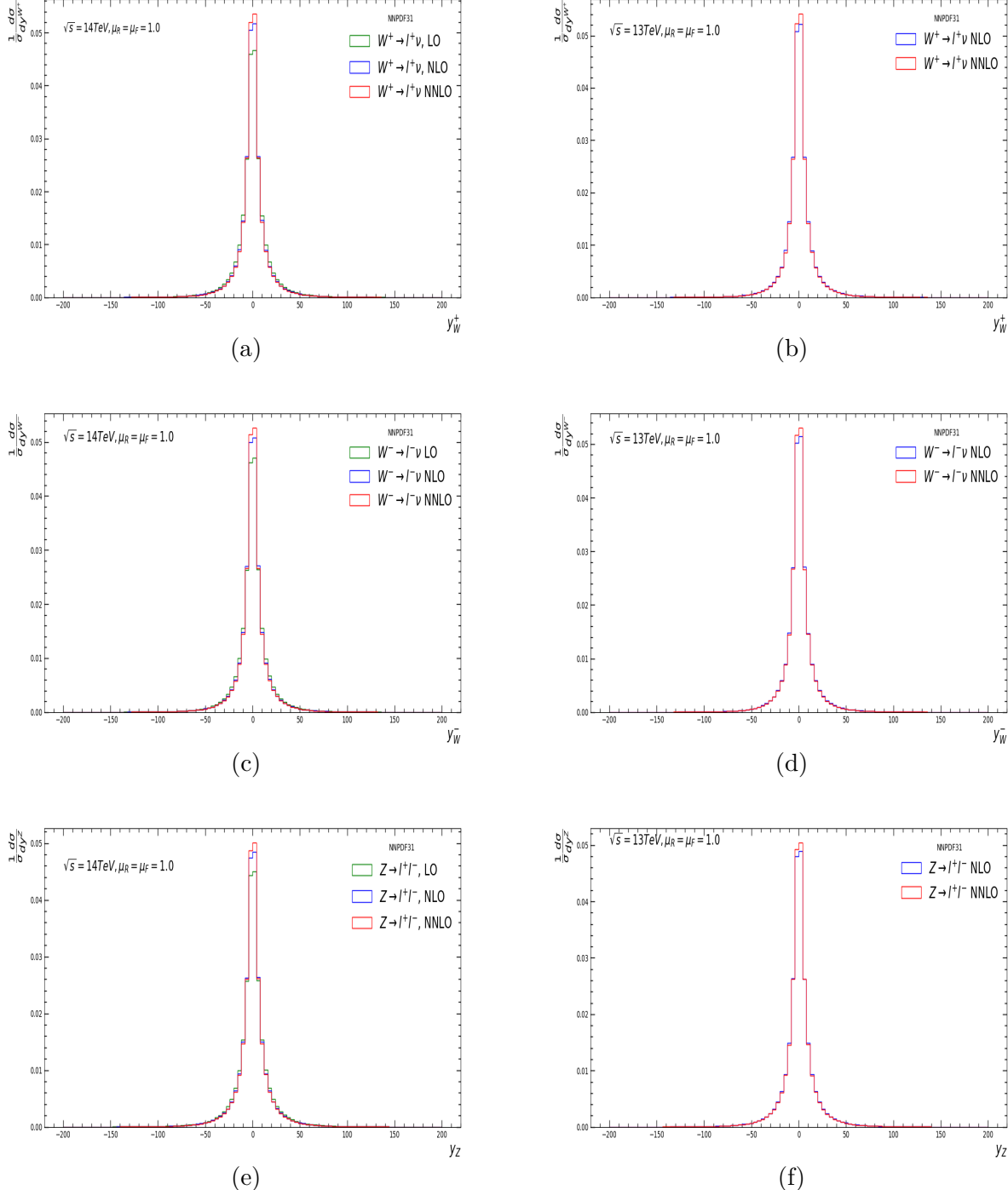
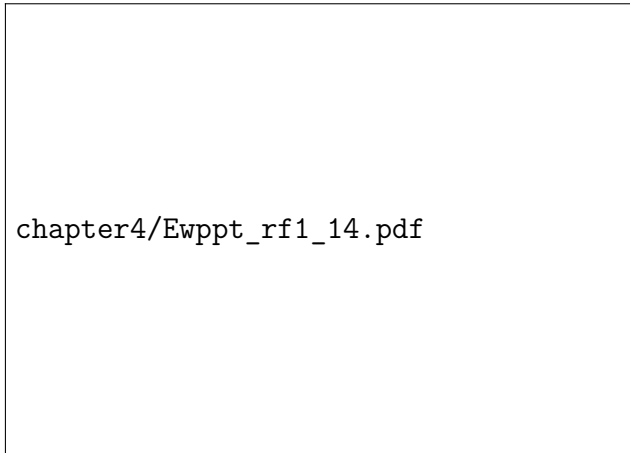


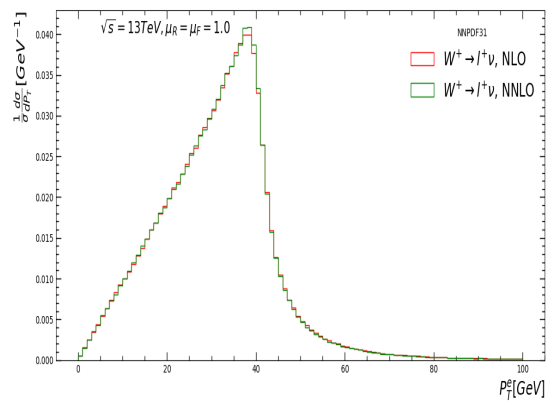
Figure 4.24: In figure 4.24a, 4.24b are the generator level rapidity distribution of W^+ boson at 14 TeV and 13 TeV . 4.24c, 4.24d for the W^- boson and 4.24e 4.24ffor Z boson rapidity distribution.

4.6 Leptons p_T and η Distribution

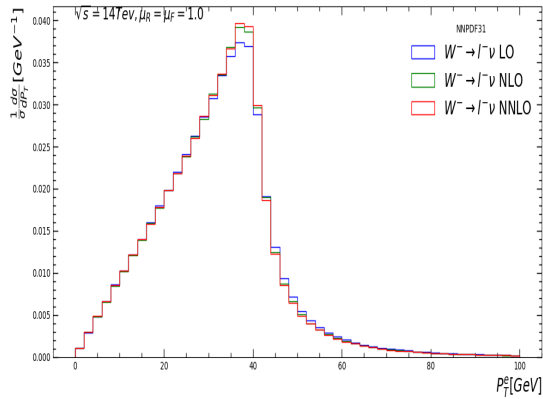
Figs. 4.25 and 4.26 show the electron p_T and η distribution at 13 TeV and 14 TeV .



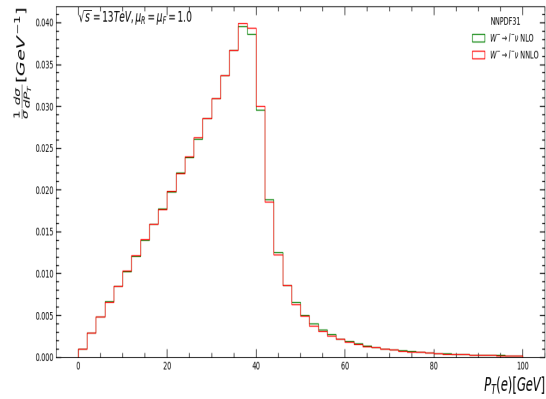
(a)



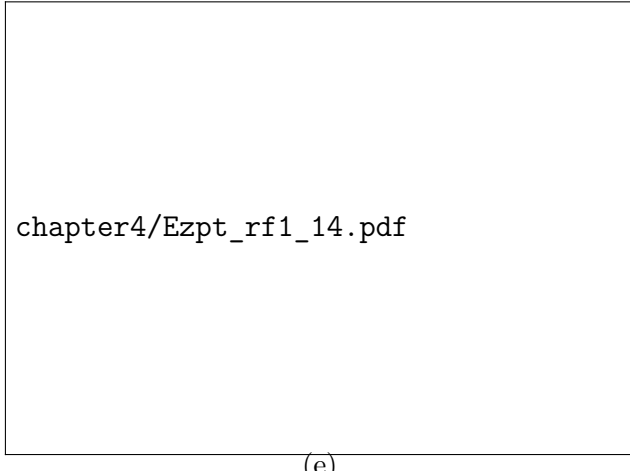
(b)



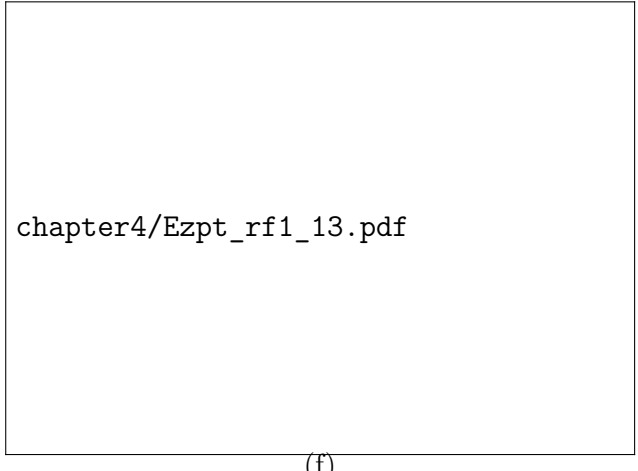
(c)



(d)

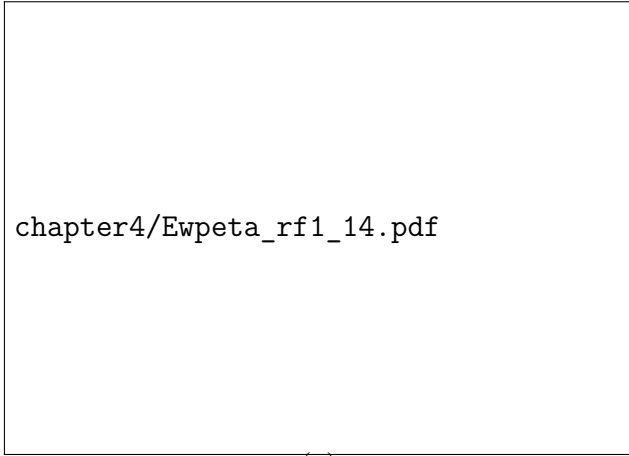


(e)

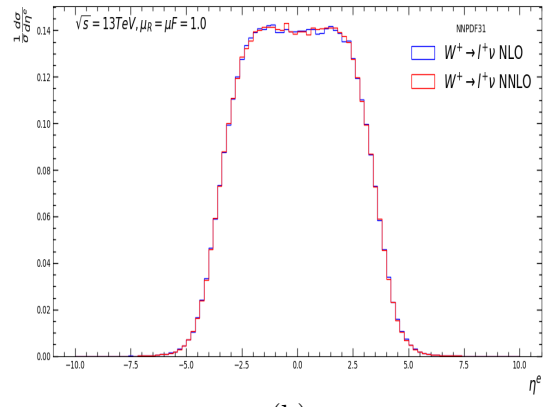


(f)

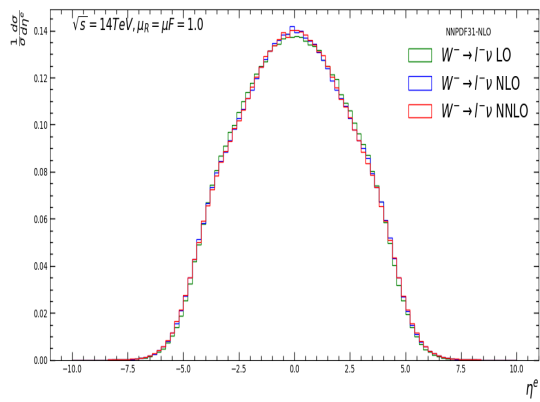
Figure 4.25: In figure 4.25a, 4.25c, 4.25e are the generator level transverse momentum distribution of electron at 14 TeV with LO, NLO, and NNLO. 4.25b, 4.25d, 4.25f for the 13 TeV for NLO and NNLO.



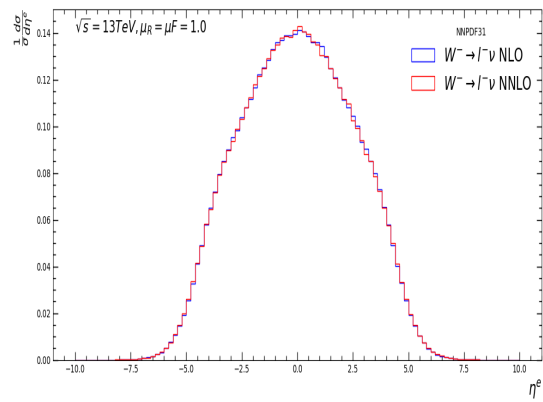
(a)



(b)



(c)



(d)

chapter4/Ezeta_rf1_14.pdf

(e)

chapter4/Ezeta_rf1_13.pdf

(f)

Figure 4.26: In figure 4.26a, 4.26c, 4.26e are the generator level pseudo rapidity distribution of electron at 14 TeV with LO, NLO, and NNLO. 4.26b, 4.26d, 4.26f for the 13 TeV for NLO and NNLO.

4.6.1 Di-lepton Mass and Rapidity Distribution

The plots in Figs. 4.27 and 4.28 show the distribution of rapidity and Di-lepton mass from $W \rightarrow e\nu$, $Z \rightarrow ll$ events at the generator level.

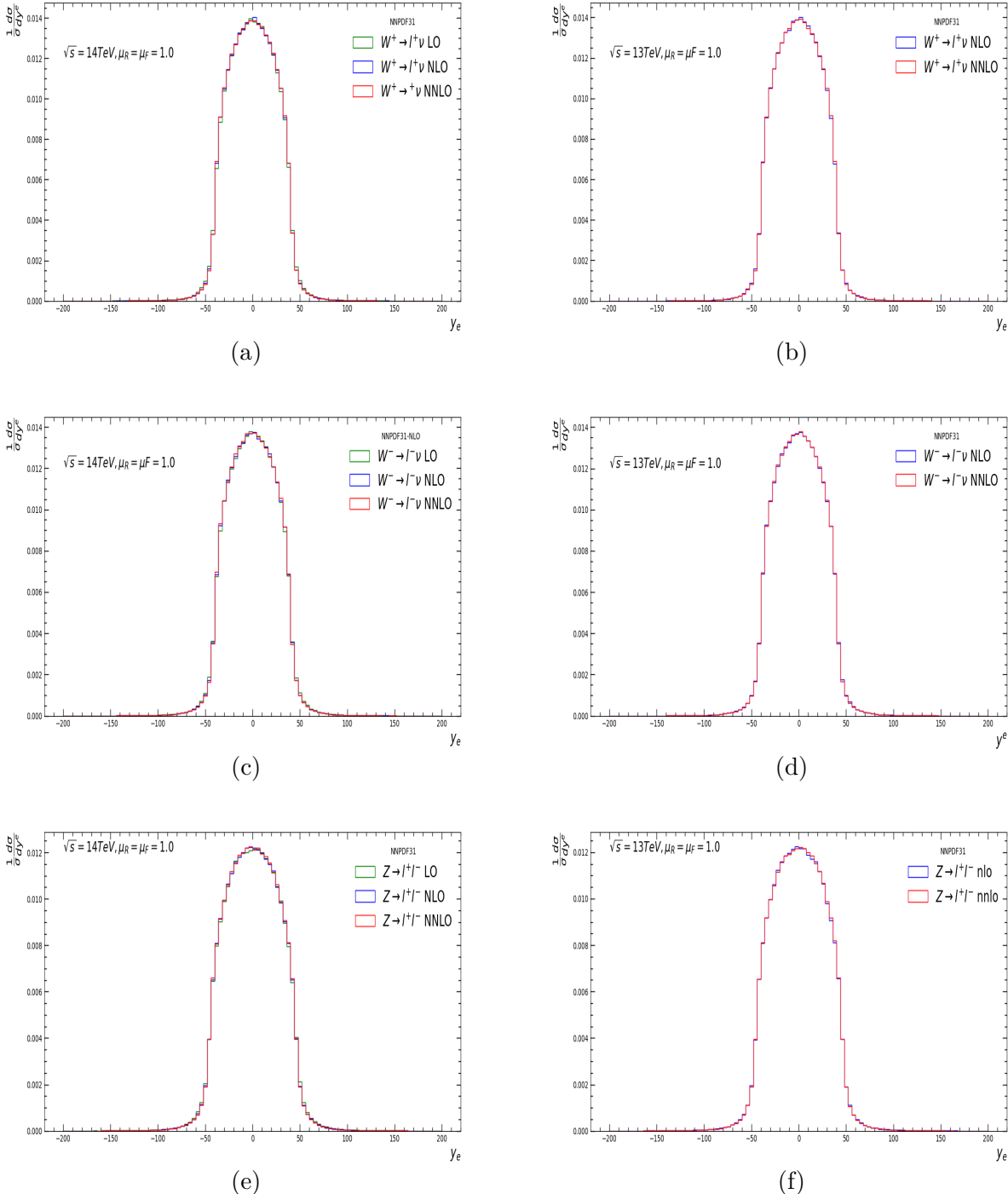


Figure 4.27: In figure 4.27a, 4.27b are the generator level rapidity distribution of electron for W^+ boson event at 14TeV and 13TeV , 4.27c, 4.27d for W^- and 4.27e, 4.27f for the Z boson event.

CHAPTER 4: RESULTS AND DISCUSSIONS

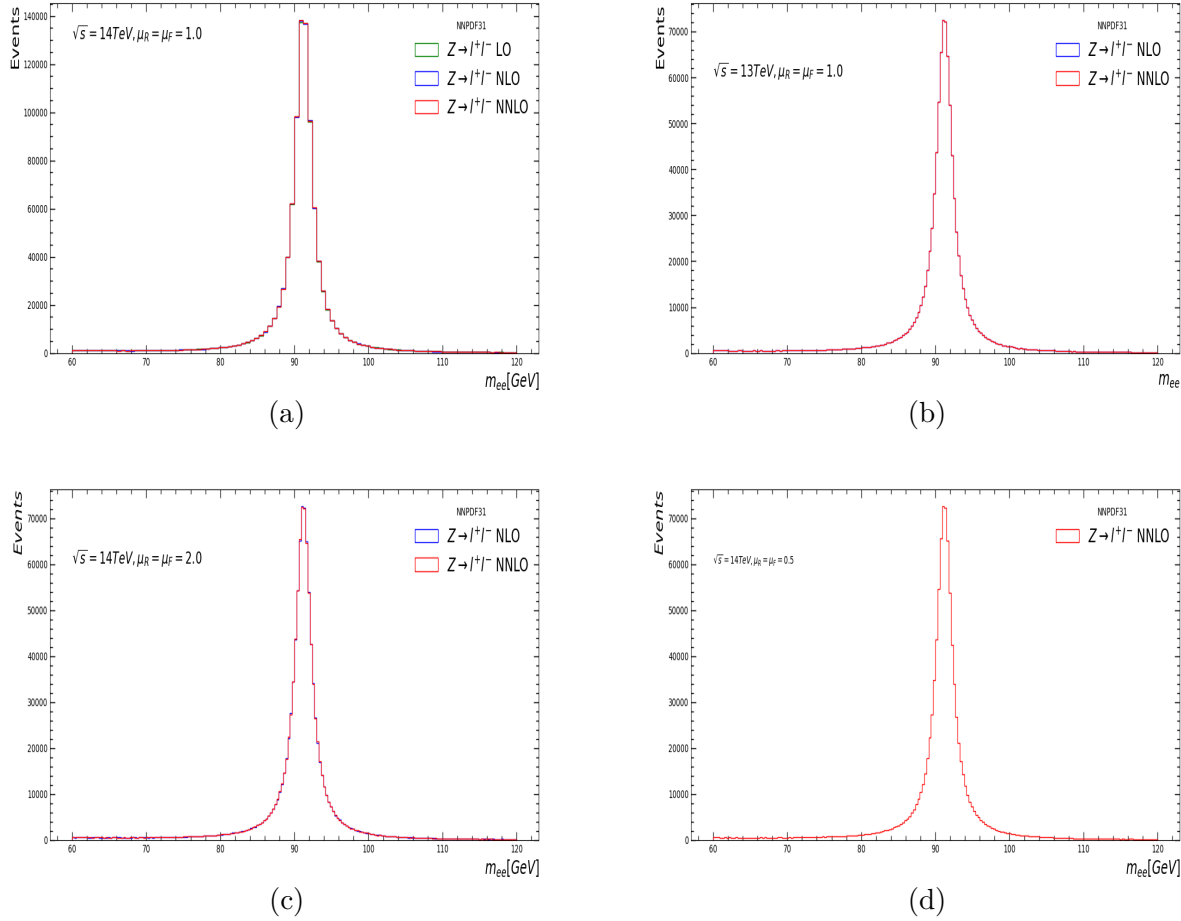


Figure 4.28: In figure 4.28a, 4.28c, 4.28d are the generator level Di-lepton transverse momentum distribution at 14 TeV with different QCD scales.

Conclusion

The study of single vector boson production cross section is very important because these bosons form background events for many important processes in Standard Model, specially events involving Higgs boson and Top quark. The precise measurement of vector boson gives deep insight to understand quantum chromodynamics (QCD) and electroweak (EW) processes. We performed a detail study of W and Z vector boson production cross section i.e. $\sigma \times BR(W \rightarrow l\nu, Z \rightarrow ll)$. The measured results of vector boson production cross section at $7\text{ TeV} \approx 40\text{ pb}^{-1}$, $8\text{ TeV} \approx 18.2\text{ pb}^{-1}$ and $13\text{ TeV} \approx 81\text{ pb}^{-1}$ are compared with the theoretically predicted cross sections. We find a great agreement between measured and theoretically predicted cross sections.

We also studied about various theoretical uncertainties in the predictions including PDF, α_s , QCD scale uncertainties etc. We also find how the W and Z boson cross section ratios are beneficial in cancellation of certain experimental and theoretical uncertainties.

The Predicted kinematics of these vector bosons and corresponding leptons are measured in detail and compared with the measured results.

We also made theoretical prediction for vector boson production cross section at 14 TeV at various QCD scales. These prediction will be checked with the measurements when the data will be available. We hope that these predictions at 14 TeV will be comparable with the measurements as were the previous results.

Bibliography

- [1] Wikipedia contributors. *Standard Model — Wikipedia, The Free Encyclopedia*. [Online; accessed 29-September-2021]. 2021. URL: https://en.wikipedia.org/w/index.php?title=Standard_Model&oldid=1045150258.
- [2] C. Patrignani et al. “Review of Particle Physics”. In: *Chin. Phys. C* 40.10 (2016), p. 100001. DOI: [10.1088/1674-1137/40/10/100001](https://doi.org/10.1088/1674-1137/40/10/100001).
- [3] Jackson David Clarke. “Physics Beyond the Standard Model”. PhD thesis. Melbourne U., 2016.
- [4] Johan Alwall. “Master of Science thesis: Supersymmetry and extensions of the Standard Model”. In: (Sept. 2001).
- [5] J. Beringer and Arguin. “Review of Particle Physics”. In: *Phys. Rev. D* 86 (1 2012), p. 010001. DOI: [10.1103/PhysRevD.86.010001](https://doi.org/10.1103/PhysRevD.86.010001). URL: <https://link.aps.org/doi/10.1103/PhysRevD.86.010001>.
- [6] (URL: <http://pdg.lbl.gov>). W. 2014. URL: <https://pdg.lbl.gov/2018/listings/rpp2018-list-z-boson.pdf>.
- [7] David Griffiths. *Introduction to Elementary Particles*. JOHN WILEY & SONS, INC, 1987.
- [8] David Griffiths. *Introduction to Electrodynamics, Chapter 12*. JOHN WILEY & SONS, INC, 1987.
- [9] Roger Peyret and Thomas D Taylor. “Quarks and Leptons”. In: 2nd ed. New York: JOHN WILEY & SONS, INC, 1984. Chap. 5.
- [10] P. Achard and O. Adriani. “Measurement of the running of the electromagnetic coupling at large momentum-transfer at LEP”. In: *Physics Letters B* 623.1 (2005), pp. 26–36. ISSN: 0370-2693. DOI: <https://doi.org/10.1016/j.physletb.2005.07.052>. URL: <https://www.sciencedirect.com/science/article/pii/S0370269305010439>.
- [11] David d’Enterria et al. *High-precision α_s measurements from LHC to FCC-ee*. 2015. arXiv: [1512.05194 \[hep-ph\]](https://arxiv.org/abs/1512.05194).
- [12] Francis Halzen and Alan D.Martin. *Quarks and Leptons: An Introductory course im modern particle physics*. JOHN WILEY & SONS, INC, 1984.
- [13] John Ellis, Mary K. Gaillard, and Dimitri V. Nanopoulos. “A Historical Profile of the Higgs Boson”. In: *The Standard Theory of Particle Physics* (2016), pp. 255274. ISSN: 1793-1339. DOI: [10.1142/9789814733519_0014](https://doi.org/10.1142/9789814733519_0014). URL: [http://dx.doi.org/10.1142/9789814733519_0014](https://dx.doi.org/10.1142/9789814733519_0014).
- [14] James Vincent Mead. “A measurement of top quark production at 13TeV with LHCb data”. Presented 27 May 2021. 2021. URL: [http://cds.cern.ch/record/2780780](https://cds.cern.ch/record/2780780).
- [15] “The Large Hadron Collider”. In: (2014). URL: <https://cds.cern.ch/record/1998498>.
- [16] Esma Mobs. “The CERN accelerator complex - 2019. Complexe des accélérateurs du CERN - 2019”. In: (2019). General Photo. URL: <https://cds.cern.ch/record/2684277>.

BIBLIOGRAPHY

- [17] The ATLAS Collaboration. “The ATLAS Experiment at the CERN Large Hadron Collider”. In: *Journal of Instrumentation* 3.08 (2008), S08003–S08003. DOI: [10.1088/1748-0221/3/08/s08003](https://doi.org/10.1088/1748-0221/3/08/s08003). URL: <https://doi.org/10.1088/1748-0221/3/08/s08003>.
- [18] The CMS Collaboration. “The CMS experiment at the CERN LHC”. In: *Journal of Instrumentation* 3.08 (2008), S08004–S08004. DOI: [10.1088/1748-0221/3/08/s08004](https://doi.org/10.1088/1748-0221/3/08/s08004). URL: <https://doi.org/10.1088/1748-0221/3/08/s08004>.
- [19] The LHCb Collaboration. “The LHCb Detector at the LHC”. In: *Journal of Instrumentation* 3.08 (2008), S08005–S08005. DOI: [10.1088/1748-0221/3/08/s08005](https://doi.org/10.1088/1748-0221/3/08/s08005). URL: <https://doi.org/10.1088/1748-0221/3/08/s08005>.
- [20] Matthias Schott and Monica Dunford. “Review of single vector boson production in pp collisions at $\sqrt{s} = 7$ s = 7 TeV”. In: *The European Physical Journal C* 74.7 (2014). ISSN: 1434-6052. DOI: [10.1140/epjc/s10052-014-2916-1](https://doi.org/10.1140/epjc/s10052-014-2916-1). URL: <http://dx.doi.org/10.1140/epjc/s10052-014-2916-1>.
- [21] Ettore Focardi. “Status of the CMS Detector”. In: *Physics Procedia* 37 (Dec. 2012), pp. 119–127. DOI: [10.1016/j.phpro.2012.02.363](https://doi.org/10.1016/j.phpro.2012.02.363).
- [22] The ALICE Collaboration. “The ALICE experiment at the CERN LHC”. In: *Journal of Instrumentation* 3.08 (2008), S08002–S08002. DOI: [10.1088/1748-0221/3/08/s08002](https://doi.org/10.1088/1748-0221/3/08/s08002). URL: <https://doi.org/10.1088/1748-0221/3/08/s08002>.
- [23] The LHCf Collaboration et al. “The LHCf detector at the CERN Large Hadron Collider”. In: *Journal of Instrumentation* 3.08 (2008), S08006–S08006. DOI: [10.1088/1748-0221/3/08/s08006](https://doi.org/10.1088/1748-0221/3/08/s08006). URL: <https://doi.org/10.1088/1748-0221/3/08/s08006>.
- [24] Dilia Maria Portillo Quintero. “Impact of Missing Transverse Energy Significance in ATLAS analyses in Run2”. In: (2019). URL: <https://cds.cern.ch/record/2668716>.
- [25] CERN. *High-Luminosity Large Hadron Collider (HL-LHC): Technical design report*. CERN Yellow Reports: Monographs. Geneva: CERN, 2020. DOI: [10.23731/CYRM-2020-0010](https://doi.org/10.23731/CYRM-2020-0010). URL: <https://cds.cern.ch/record/2749422>.
- [26] Muhammad Waqas. “Search for the associated production of a Z boson with a single top quark using CMS data at 8 TeV and 13 TeV and performance studies of the CMS silicon tracker.” Presented 04 Sep 2019. 2019. URL: <https://cds.cern.ch/record/2779481>.
- [27] S. Chatrchyan et al. “Observation of a new boson at a mass of 125 GeV with the CMS experiment at the LHC”. In: *Physics Letters B* 716.1 (2012), pp. 3061. ISSN: 0370-2693. DOI: [10.1016/j.physletb.2012.08.021](https://doi.org/10.1016/j.physletb.2012.08.021). URL: <http://dx.doi.org/10.1016/j.physletb.2012.08.021>.
- [28] Siona Ruth Davis. “CMS slice image view (transverse/longitudinal/3-D)”. In: (2016). URL: [http://cds.cern.ch/record/2204863](https://cds.cern.ch/record/2204863).
- [29] CMS Collaboration. “Performance of the CMS drift-tube chamber local trigger with cosmic rays”. In: *Journal of Instrumentation* 5.03 (2010), T03003–T03003. DOI: [10.1088/1748-0221/5/03/t03003](https://doi.org/10.1088/1748-0221/5/03/t03003). URL: <https://doi.org/10.1088/1748-0221/5/03/t03003>.
- [30] J. G. Layter. *The CMS muon project: Technical Design Report*. Technical design report. CMS. Geneva: CERN, 1997. URL: <https://cds.cern.ch/record/343814>.
- [31] *The CMS electromagnetic calorimeter project: Technical Design Report*. Technical design report. CMS. Geneva: CERN, 1997. URL: <https://cds.cern.ch/record/349375>.

BIBLIOGRAPHY

- [32] The CMS collaboration. “Missing transverse energy performance of the CMS detector”. In: *Journal of Instrumentation* 6.09 (2011), P09001P09001. ISSN: 1748-0221. DOI: [10.1088/1748-0221/6/09/p09001](https://doi.org/10.1088/1748-0221/6/09/p09001). URL: <http://dx.doi.org/10.1088/1748-0221/6/09/P09001>.
- [33] Vyacheslav Klyukhin. “Design and Description of the CMS Magnetic System Model”. In: *Symmetry* 13 (2021), 1052. 18 p. DOI: [10.3390/sym13061052](https://doi.org/10.3390/sym13061052). URL: <http://cds.cern.ch/record/2773274>.
- [34] A.M. Sirunyan et al. “Performance of the CMS muon detector and muon reconstruction with proton-proton collisions at 13 TeV”. In: *Journal of Instrumentation* 13.06 (2018). ISSN: 1748-0221. DOI: [10.1088/1748-0221/13/06/p06015](https://doi.org/10.1088/1748-0221/13/06/p06015). URL: <http://dx.doi.org/10.1088/1748-0221/13/06/P06015>.
- [35] V. Khachatryan et al. “The CMS trigger system”. In: *Journal of Instrumentation* 12.01 (2017), P01020P01020. ISSN: 1748-0221. DOI: [10.1088/1748-0221/12/01/p01020](https://doi.org/10.1088/1748-0221/12/01/p01020). URL: <http://dx.doi.org/10.1088/1748-0221/12/01/P01020>.
- [36] Sergio Cittolin, Attila Rcz, and Paris Sphicas. *CMS The TriDAS Project: Technical Design Report, Volume 2: Data Acquisition and High-Level Trigger. CMS trigger and data-acquisition project*. Technical design report. CMS. Geneva: CERN, 2002. URL: <https://cds.cern.ch/record/578006>.
- [37] P. J. Rijken and W. L. van Neerven. “Order”. In: *Phys. Rev. D* 51 (1 1995), pp. 44–63. DOI: [10.1103/PhysRevD.51.44](https://doi.org/10.1103/PhysRevD.51.44). URL: <https://link.aps.org/doi/10.1103/PhysRevD.51.44>.
- [38] W.L. van Neerven and E.B. Zijlstra. “The corrected Drell-Yan K-factor in the DIS and MS schemes”. In: *Nuclear Physics B* 382.1 (1992), pp. 11–62. ISSN: 0550-3213. DOI: [https://doi.org/10.1016/0550-3213\(92\)90078-P](https://doi.org/10.1016/0550-3213(92)90078-P). URL: <https://www.sciencedirect.com/science/article/pii/055032139290078P>.
- [39] G. Aad and B. Abbott. “Measurement of W \pm and Z-boson production cross sections in pp collisions at s=13 TeV with the ATLAS detector”. In: *Physics Letters B* 759 (2016), pp. 601–621. ISSN: 0370-2693. DOI: <https://doi.org/10.1016/j.physletb.2016.06.023>. URL: <https://www.sciencedirect.com/science/article/pii/S0370269316302763>.
- [40] G. Arnison et al. “Experimental Observation of Isolated Large Transverse Energy Electrons with Associated Missing Energy at $\sqrt{s} = 540$ GeV”. In: *Phys. Lett. B* 122 (1983), pp. 103–116. DOI: [10.1016/0370-2693\(83\)91177-2](https://doi.org/10.1016/0370-2693(83)91177-2).
- [41] P. Bagnaia et al. “Evidence for $Z^0 \rightarrow e^+e^-$ at the CERN $p\bar{p}$ Collider”. In: *Phys. Lett. B* 129 (1983), pp. 130–140. DOI: [10.1016/0370-2693\(83\)90744-X](https://doi.org/10.1016/0370-2693(83)90744-X).
- [42] *A Combination of Preliminary Results on Gauge Boson Couplings Measured by the LEP experiments*. Tech. rep. 2003 Summer Conferences. Geneva: CERN, 2003. URL: <https://cds.cern.ch/record/2285934>.
- [43] F. Abe and Amidei. “Measurement of W-boson production in 1.8-TeV p $^-$ p collisions”. In: *Phys. Rev. Lett.* 62 (9 1989), pp. 1005–1008. DOI: [10.1103/PhysRevLett.62.1005](https://doi.org/10.1103/PhysRevLett.62.1005). URL: <https://link.aps.org/doi/10.1103/PhysRevLett.62.1005>.
- [44] V. M. Abazov and Abbott. “Measurement of the Shape of the Boson-Transverse Momentum Distribution in $p\bar{p} \rightarrow Z/\gamma^* \rightarrow e^+e^- + X$ Events Produced at $\sqrt{s} = 1.96$ TeV”. In: *Phys. Rev. Lett.* 100 (10 2008), p. 102002. DOI: [10.1103/PhysRevLett.100.102002](https://doi.org/10.1103/PhysRevLett.100.102002). URL: <https://link.aps.org/doi/10.1103/PhysRevLett.100.102002>.

BIBLIOGRAPHY

- [45] Sunil Mukhi. “Renormalisation in Quantum Field Theory”. In: Aug. 2019. arXiv: [1908.04075 \[hep-ph\]](#).
- [46] Jen-Chieh Peng and Jian-Wei Qiu. “The Drell-Yan Process”. In: *The Universe* 4.3 (2016), pp. 34–44.
- [47] A. D. Martin et al. “Parton distributions for the LHC”. In: *The European Physical Journal C* 63.2 (2009), pp. 189285. ISSN: 1434-6052. DOI: [10.1140/epjc/s10052-009-1072-5](#). URL: <http://dx.doi.org/10.1140/epjc/s10052-009-1072-5>.
- [48] Pavel M. Nadolsky et al. “Implications of CTEQ global analysis for collider observables”. In: *Physical Review D* 78.1 (2008). ISSN: 1550-2368. DOI: [10.1103/physrevd.78.013004](#). URL: <http://dx.doi.org/10.1103/PhysRevD.78.013004>.
- [49] S. Alekhin et al. “3-, 4-, and 5-flavor next-to-next-to-leading order parton distribution functions from deep-inelastic-scattering data and at hadron colliders”. In: *Physical Review D* 81.1 (2010). ISSN: 1550-2368. DOI: [10.1103/physrevd.81.014032](#). URL: <http://dx.doi.org/10.1103/PhysRevD.81.014032>.
- [50] Richard D. Ball et al. “Precision NNLO determination of $\alpha_s(M_Z)$ using an unbiased global parton set”. In: *Phys. Lett. B* 707 (2012), pp. 66–71. DOI: [10.1016/j.physletb.2011.11.053](#). arXiv: [1110.2483 \[hep-ph\]](#).
- [51] B. Blok and P. Gunnellini. “Dynamical approach to MPI in W+dijet and Z+dijet production within the PYTHIA event generator”. In: *The European Physical Journal C* 76.4 (2016). ISSN: 1434-6052. DOI: [10.1140/epjc/s10052-016-4035-7](#). URL: <http://dx.doi.org/10.1140/epjc/s10052-016-4035-7>.
- [52] Torbjörn Sjöstrand, Stephen Mrenna, and Peter Skands. “A brief introduction to PYTHIA 8.1”. In: *Computer Physics Communications* 178.11 (2008), pp. 852867. ISSN: 0010-4655. DOI: [10.1016/j.cpc.2008.01.036](#). URL: <http://dx.doi.org/10.1016/j.cpc.2008.01.036>.
- [53] Gennaro Corcella et al. “HERWIG 6: an event generator for hadron emission reactions with interfering gluons (including supersymmetric processes)”. In: *Journal of High Energy Physics* 2001.01 (2001), pp. 010010. ISSN: 1029-8479. DOI: [10.1088/1126-6708/2001/01/010](#). URL: <http://dx.doi.org/10.1088/1126-6708/2001/01/010>.
- [54] T Gleisberg et al. “Event generation with SHERPA 1.1”. In: *Journal of High Energy Physics* 2009.02 (2009), pp. 007007. ISSN: 1029-8479. DOI: [10.1088/1126-6708/2009/02/007](#). URL: <http://dx.doi.org/10.1088/1126-6708/2009/02/007>.
- [55] C. Oleari. “The POWHEG BOX”. In: *Nuclear Physics B - Proceedings Supplements* 205-206 (2010), pp. 3641. ISSN: 0920-5632. DOI: [10.1016/j.nuclphysbps.2010.08.016](#). URL: <http://dx.doi.org/10.1016/j.nuclphysbps.2010.08.016>.
- [56] S. Chatrchyan et al. “Measurement of the inclusive W and Z production cross sections in pp collisions at $\sqrt{s} = 7$ TeV with the CMS experiment”. In: *Journal of High Energy Physics* 2011.10 (2011). ISSN: 1029-8479. DOI: [10.1007/jhep10\(2011\)132](#). URL: [http://dx.doi.org/10.1007/JHEP10\(2011\)132](http://dx.doi.org/10.1007/JHEP10(2011)132).
- [57] G. Aad et al. “Measurement of W and Z-boson production cross sections in pp collisions at s=13 TeV with the ATLAS detector”. In: *Physics Letters B* 759 (2016), pp. 601621. ISSN: 0370-2693. DOI: [10.1016/j.physletb.2016.06.023](#). URL: <http://dx.doi.org/10.1016/j.physletb.2016.06.023>.
- [58] G. Aad et al. “Determination of the Strange-Quark Density of the Proton from ATLAS Measurements of the W and Z Cross Sections”. In: *Physical Review Letters* 109.1 (2012). ISSN: 1079-7114. DOI: [10.1103/physrevlett.109.012001](#). URL: <http://dx.doi.org/10.1103/PhysRevLett.109.012001>.

BIBLIOGRAPHY

- [59] Richard D. Ball et al. “Parton distribution benchmarking with LHC data”. In: *Journal of High Energy Physics* 2013.4 (2013). ISSN: 1029-8479. DOI: [10.1007/jhep04\(2013\)125](https://doi.org/10.1007/jhep04(2013)125). URL: [http://dx.doi.org/10.1007/JHEP04\(2013\)125](http://dx.doi.org/10.1007/JHEP04(2013)125).
- [60] “Measurement of Inclusive W and Z Boson Production Cross Sections”. In: *Physical Review Letters* 112.19 (2014). ISSN: 1079-7114. DOI: [10.1103/physrevlett.112.191802](https://doi.org/10.1103/physrevlett.112.191802). URL: <http://dx.doi.org/10.1103/PhysRevLett.112.191802>.
- [61] “Measurement of inclusive W and Z boson production cross sections in pp collisions at $\sqrt{s}=13$ TeV”. In: (2015).
- [62] Sergey Alekhin et al. *The PDF4LHC Working Group Interim Report*. 2011. arXiv: [1101.0536 \[hep-ph\]](https://arxiv.org/abs/1101.0536).
- [63] G. Watt. “Parton distribution function dependence of benchmark Standard Model total cross sections at the 7 TeV LHC”. In: *Journal of High Energy Physics* 2011.9 (2011). ISSN: 1029-8479. DOI: [10.1007/jhep09\(2011\)069](https://doi.org/10.1007/jhep09(2011)069). URL: [http://dx.doi.org/10.1007/JHEP09\(2011\)069](http://dx.doi.org/10.1007/JHEP09(2011)069).